

## UARS Microwave Limb Sounder upper tropospheric humidity measurement: Method and validation

W. G. Read, J. W. Waters, D. L. Wu, E. M. Stone<sup>1</sup>, Z. Shippony,  
A. C. Smedley and C. C. Smallcomb<sup>2</sup>

Jet Propulsion Laboratory, California Institute of Technology, Pasadena, CA.

S. Oltmans

NOAA Climate Monitoring and Diagnostics Laboratory, Boulder, CO.

D. Kley, and H. G. J. Smit

Institute for Chemistry of the Polluted Atmosphere, Department for Chemistry and Dynamics of the Geosphere, Research Centre Juelich GmbH, Juelich, Germany.

J. L. Mergenthaler

Lockheed Martin Research Advanced Technology Center, Palo Alto, CA.

M. K. Karki

NASA Goddard Space Flight Center, Greenbelt, MD.

**Abstract.** The methodology and validation of upper tropospheric humidity (UTH) measurements by the Microwave Limb Sounder (MLS) on the Upper Atmosphere Research Satellite (UARS) are described. The MLS instrument was not specifically designed to measure UTH, but its measurement is achieved by modeling the radiance signal from a window channel as the instrument field of view is scanned through the troposphere. UTH is retrieved as a piecewise-linear function in relative humidity with respect to ice (% RH<sub>i</sub>) with breakpoints at 147, 215, 316, and 464 hPa. MLS version 4.9 is believed to be the most accurate version to date; its estimated global-averaged accuracy(precision) is 23(21), 22(10), 22(8), and 50(19) %RH<sub>i</sub> at 147, 215, 316, and 464, hPa respectively. The validation of UTH is established by its consistency with (1) climatological fields, (2) coincident comparisons with in situ Vaisala RS80 balloon sondes, frostpoint hygrometers and Measurement of Ozone and Water Vapor by Airbus In-Service Aircraft measurements, (3) cirrus observations, and (4) meteorological dynamics and assimilation fields. MLS climatological UTH is morphologically consistent with Stratospheric Aerosol and Gas Experiment II and Vaisala zonal climatologies. Comparisons with coincident in situ data show a wide range of agreement. Relative to the other in situ instruments, V4.9 MLS humidities agree on average within 11% at 147 hPa, 3–36% dry at 215 hPa, and 14–39% dry at 316 and 464 hPa. The standard deviation of the individual comparisons about the mean between MLS UTH and the other techniques is approximately 25 %RH<sub>i</sub> at all heights. Humidity measurements in cirrus are compared with UARS Cryogenic Limb Array Etalon Spectrometer (CLAES) extinction measurements and an MLS cirrus detection algorithm. CLAES extinction measurements from 316 to 147 hPa which indicate the presence of cirrus correspond well with MLS UTH measurements greater than ~100 %RH<sub>i</sub>. Global MLS UTH distributions appear consistent with those expected from upper tropospheric dynamics and with the Goddard Data Assimilation Office humidity fields.

## 1. Introduction

Tropospheric humidity affects weather and climate. Water vapor, the dominant greenhouse gas, is hypothesized to amplify the effects from other greenhouse gases [Intergovernmental Panel on Climate Change, 1995; Manabe and Wetherald, 1967]. General circulation models (GCM) [e.g., Cess *et al.*, 1990] test our understanding of climate, and data assimilation models are used to study and forecast weather [Schubert *et al.*, 1993]. These models produce a description of the atmosphere that includes water vapor. Comparing modeled with measured humidity is one way to test the accuracy of the GCM. The data assimilation model estimates water vapor continuously over time and space using measured water vapor fields as constraints. Physical processes in the atmosphere couple water vapor in all its dimensions, and its variability is high. There is an ongoing need for water vapor measurements globally and continuously. Particularly needed are humidity measurements in the upper troposphere. Upper tropospheric humidity (UTH) contributes half of the forcing in the Earth's radiation budget, but its origin and response to surface temperature is uncertain [Intergovernmental Panel on Climate Change, 1995; Lindzen, 1990]. UTH is not measured sufficiently frequently and reliably to refine models and supply the needs of data assimilation.

The Microwave Limb Sounder (MLS) on the Upper Atmosphere Research Satellite (UARS) was not designed specifically for UTH measurement, but the 203 GHz radiometer that measures weak stratospheric signals from the CIO molecule also receives water vapor continuum emissions when the radiometer field of view is scanned through the troposphere. A preliminary UTH retrieval was previously developed [Read *et al.*, 1995]; an improved retrieval and forward model is presented here and its performance is assessed.

The MLS UTH complements existing measurements. Stratospheric Aerosol and Gas Experiment (SAGE) II [Rind *et al.*, 1993] and radiosondes [Gaffen, 1993] have  $\leq 1$  km vertical resolution but have limited and incomplete global coverage. The nadir sounding operational satellites [Wu *et al.*, 1993] have complete global coverage but with poor vertical resolution and registration (the height of its UTH measurement depends on the water vapor concentration). The MLS UTH is between these extremes having  $\sim 1300$  profiles measured daily throughout the globe with  $\sim 3$  km vertical sampling. The best UTH measurements are for concentrations between 10–500 ppmv. Higher concentrations, up to a few thousand ppmv, are measurable with poorer accuracy. The vertical coverage ranges from  $\sim 500$  hPa to

$\sim 150$  hPa, including the uppermost troposphere which is not observed well by the nadir sounding humidity sensors or the majority of radiosondes.

This paper is organized as follows. Section 2 presents the theoretical basis of the measurement. In section 3, the expected accuracy and precision of the measurements and a comparison among the three MLS UTH versions are given. Some warnings and unphysical behaviors associated with the MLS UTH data are shown along with data usage recommendations in section 4. The MLS V4.9 UTH climatology maps are given in section 5 and compared with UTH climatologies from Vaisala radiosondes and SAGE II. In section 6, comparisons of MLS profiles with those measured coincidentally with frostpoint hygrometers, Vaisala RS80 radiosondes, aircraft mounted sensors, and cirrus detection are shown. MLS mapped fields are compared to Goddard Data Assimilation Office Earth Observing System (GEOS) reanalysis humidity and to derived fields such as potential vorticity and velocity potential/divergent winds from National Centers for Environmental Prediction (NCEP) in section 7. Conclusions and a discussion of future work are given in sections 8 and 9 respectively.

## 2. UARS MLS Upper Tropospheric Humidity Measurement

### 2.1. Measurement Description

The Microwave Limb Sounder (MLS) is a limb sounding instrument that measures thermal emission in bands near 63, 183, and 203 GHz [Barath *et al.*, 1993; Waters *et al.*, 1999]. UARS is in a circular  $57^\circ$  inclination orbit, at 585 km altitude, and MLS views the atmospheric limb in a direction perpendicular to the orbit path. There are 15 orbits per day and MLS measures a radiance profile every  $4.1^\circ$  of orbit arc. A radiometric profile is measured from the surface to 90 km. The global coverage is between  $81^\circ\text{S}$  and  $34^\circ\text{N}$  or  $34^\circ\text{S}$  and  $81^\circ\text{N}$  depending on the yaw state of the spacecraft which alternates on average every 36 days. The orbital precession causes the measurement longitude to move westward  $5^\circ$ , or 20 min earlier in local time, over a 24 hour period.

The UTH retrieval is based on a single spectral channel (MLS channel 30) radiance profile measurement which becomes nonlinearly proportional to the  $\text{H}_2\text{O}$  continuum emission with increasing path attenuation. This differs significantly from the other MLS constituent retrievals where a distinct spectral line feature is resolved and fitted (with the exception of  $\text{HNO}_3$  where a line wing is fitted). The MLS 183 GHz radiometer measures a strong water line but is mostly limited to stratospheric-like concentrations ( $< 10$  ppmv) and does not penetrate into the troposphere because the  $\sim 500$  MHz bandwidth is not sufficiently broad. The

<sup>1</sup>Now at ASM Lithography Holding N. V., CT.

<sup>2</sup>Now at National Weather Service, Louisville, KY.

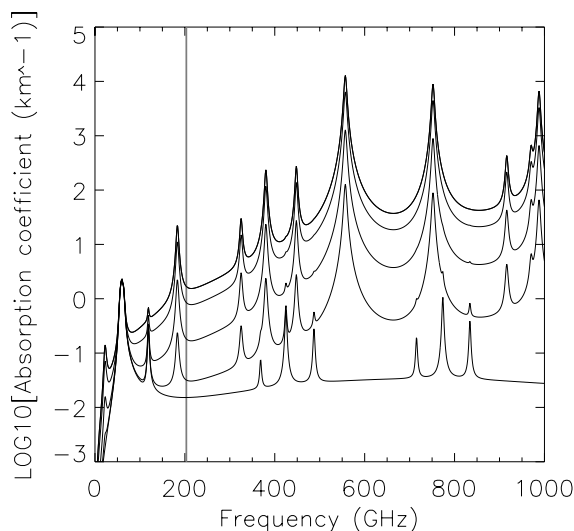


**Figure 1.** The MLS UTH measurement frequencies ( $\sim 202$  and  $204$  GHz) shown together as the vertical line in relation to the moist atmospheric absorption functions based on the millimeter-wave propagation model (figure adapted from Liebe [1989]). The five curves, in increasing order of absorption coefficient, represent 0%, 1%, 10%, 50%, and 100% relative humidity, respectively. The calculation is for 1013 hPa and 300 K.

scanned field of view (FOV) of the 203 GHz radiometer easily penetrates the troposphere and is free of strong stratospheric emitters. The dominant contributors to the signal in the troposphere are air and water vapor continua. Figure 1 shows the MLS measurement frequency in relation to oxygen and water emissions. The MLS UTH measurement uses channel 30, which simultaneously receives radiation from 204528 and 202006 MHz with weights 0.428 and 0.572, respectively, in a 94 MHz fullwidth ( $-3$  dB) filter [Jarnot *et al.*, 1996]. The measurement occurs in a “window” region in the moist atmospheric absorption coefficient spectrum, and we can neglect spectral differences in the water vapor and dry continuum emission at the two frequencies. It is also possible to measure water vapor into the uppermost troposphere using the image sideband of the 183 GHz radiometer which is centered at 186 GHz; however, that analysis is complicated by needing to remove the stratospheric 183 GHz water vapor contributions prior to analyzing the 186 GHz water vapor line wing and is not discussed further.

Plate 1 shows the channel 30 MLS radiance distribution as a function of radiance (brightness) and limb tangent pressure for all measurements in 1992. Radiance measurements have been counted and binned into a 61 by 65 equally spaced

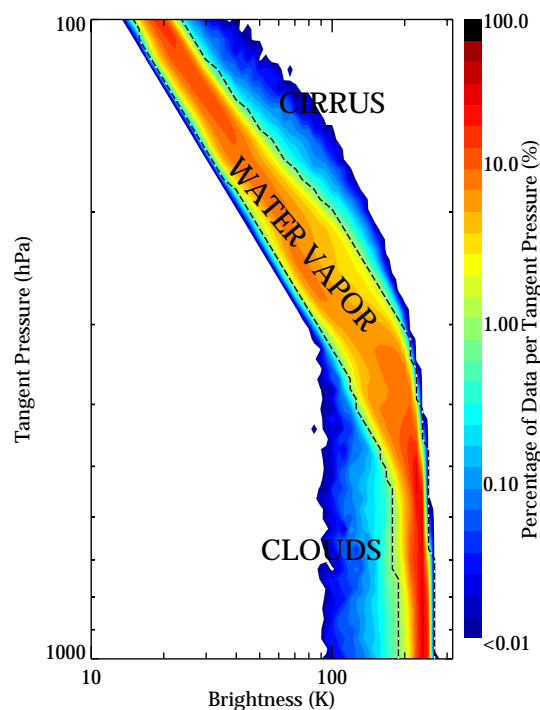


**Plate 1.** Channel 30 measured radiance versus limb tangent pressure for all data taken in 1992. The colors indicate the measurement frequency per tangent pressure value. See text for a full description.

grid array according to logarithm of brightness and tangent pressure. At each tangent pressure grid value the total number of measurements is counted. The number of measurements for each brightness and tangent pressure grid box is divided by the total number of measurements for that tangent pressure yielding a percent which is colored according to the accompanying scale. Plate 1 shows that most of the measurements are confined within a well-defined band. The brightness temperature of the measured radiances for limb tangent pressures less than 300 hPa (higher altitudes) are almost always less than the atmospheric temperature and are proportional to absorption. Taking a slice along a tangent pressure value in Plate 1 will reveal two distinct radiances where the measurement frequency rapidly rises and then rapidly falls with increasing radiance. The radiances bounded by these two gradients (at tangent heights above 300 hPa) are interpreted as observations of 0–100% relative humidity with respect to ice (%RHi) in clear sky or in thin cirrus. The two regions having steep gradients are indicated by dotted lines in Plate 1. Brightness temperatures for the majority of measurements at tangent heights below 500 hPa are near the atmospheric temperature, indicating an opaque atmosphere. The height at which the atmosphere becomes opaque is determined by the atmospheric humidity and is the lowest altitude where humidity measurements can be made. Channel 30 is always sensitive to atmospheric humidity above 300 hPa and often down to 500 hPa.

Radiances between 100 and 300 hPa along the left edge of the band marked “WATER VAPOR” in Plate 1 come from a dry atmosphere with less than  $\sim 2$  %RHi. These measurements are well fit by a uniformly mixed gas having absorption coefficient with pressure-squared dependence. Such dependence is expected for collision induced absorption (CIA) [Borysow and Frommhold, 1986; Dagg et al., 1985, and references therein], and the magnitude of the radiances is in acceptable agreement with calculated CIA emission from the well-mixed gases  $N_2$  and  $O_2$  as discussed later in this paper. Independent indications of very dry upper tropospheric conditions are given by Spencer and Braswell [1997]. Their analyses of data from the Defense Meteorological Satellite Program (DMSP) show that the  $30^\circ S$ – $30^\circ N$  upper tropospheric humidity distribution peaks between 5 and 10% relative humidity with respect to liquid water (%RHw) with values as low as 2 %RHw ( $\leq 4$  %RHi) observed. Dry stratospheric air ( $< 5$  %RHi) is also observed at higher latitudes down to 400 hPa [Rood et al., 1997].

Radiances at 100–400 hPa along the right edge of the band marked “WATER VAPOR” in Plate 1 are at the transition from clear (and thin cirrus, to which MLS is insensitive) to thick cirrus where the atmosphere is near 100 %RHi. The magnitude of these radiances is in reasonable agree-

ment, as discussed later in this paper, with calculated continuum emission from water vapor with 100 %RHi. Radiances greater than the upper edge of the “WATER VAPOR” band in Plate 1 at 150 hPa correlate well with cirrus detection using a two-band detection method discussed later. Radiation scattering and emissions from thick clouds explain the presence of measurements outside of the “WATER VAPOR” band. At higher altitudes (tangent pressures less than 300 hPa) the radiances are enhanced, and at lower altitudes (tangent pressures greater than 400 hPa) the radiances are depressed.

## 2.2. UTH Profile Parameterization

Retrieving UTH in %RHi units is done for the following reasons. The ambient temperature of the MLS UTH vertical coverage is almost always below freezing; therefore cirrus detection is facilitated with %RHi. Tropospheric water vapor mixing ratio and density have steep vertical gradients and a layer (or volume) average in these units is hard to interpret. Relative humidity, %RHi, is expected to better model the steep concentration gradient with fewer profile points.

The humidity profile is represented by

$$rh(\zeta) = \sum_{q=1}^4 RH_q \eta_q^{rh}(\zeta), \quad (1)$$

where  $rh$  is the “continuous” relative humidity function in %RHi,  $RH_q$  is a retrievable relative humidity coefficient in %RHi,  $\eta_q^{rh}(\zeta)$  is the representation basis and  $\zeta$  is the vertical coordinate,  $-\log[\text{pressure}/(\text{hPa})]$ . The representation basis functions with some modifications are similar to those used for other MLS products [Froidevaux et al., 1996] but have four breakpoints at 464, 316, 215, and 146 hPa. The  $\eta_q^{rh}(\zeta)$  functions are shown relative to a sample UTH profile in Figure 2.

## 2.3. MLS UTH Data Versions

There currently exist three MLS UTH data versions: “preliminary,” V4.9 (also known as V490), and V5. The preliminary UTH data version used a simple retrieval and forward model described by Read et al. [1995]. Data from this version have been used in a number of publications [Chandra et al., 1998; Chen et al., 1999, 1998; Clark et al., 1998; Elson et al., 1996; Haas and Pfister, 1998; Hu and Liu, 1998; Newell et al., 1997, 1996a, b; Rood et al., 1997; Sandor et al., 1998; Stone et al., 1996; Waters et al., 1999]. The preliminary version used the Liebe [1989] model for the  $H_2O$  absorption coefficient and a dry continuum absorption coefficient function derived from stratospheric radiances (tangent pressures below 50 hPa). The forward model neglected MLS field-of-view effects and the retrieval was

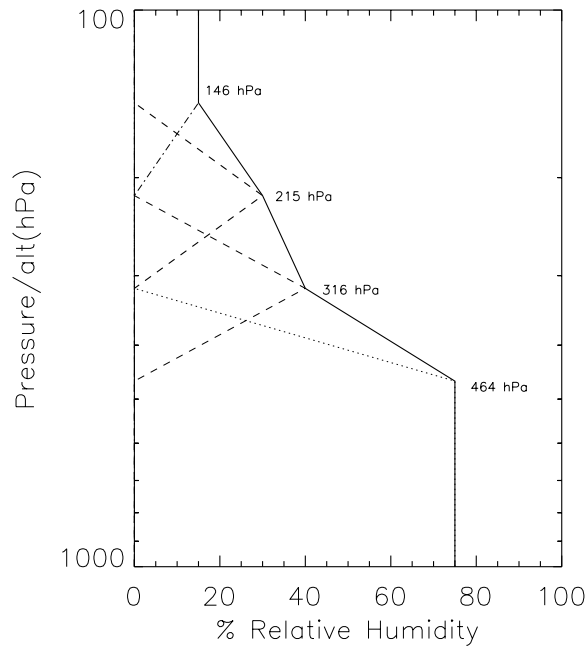


**Figure 2.** The MLS UTH representation basis functions (broken lines) for a sample UTH profile (solid line). The representation bases are multiplied by the coefficient break point values to produce the resulting UTH profile.

limited to optically thin radiances (signals less than 180 K). The preliminary version provided a good qualitative UTH measurement but it is generally too wet, especially at high latitudes. The excess humidity in the preliminary version is caused by an error in its dry continuum absorption coefficient function determined from stratospheric radiances, which did not extrapolate well into the troposphere.

An improved forward model and a nonlinear, a priori constrained, least squares retrieval is used to produce the V4.9 and V5 versions described here. V4.9 and V5 use tropospheric radiances to determine the dry and water vapor (wet) absorption coefficient functions, as described later. The principal difference between V4.9 and V5 is that V4.9 used radiances in what we believe is vapor-saturated air, and assumed insensitivity to ice emissions, to determine the wet component of the atmospheric absorption coefficient. V5 used coincident Vaisala radiosonde UTH measurements to establish the wet absorption coefficient function.

## 2.4. MLS UTH Forward Model

The forward model, which calculates the radiances used for UTH measurement, is described by *Read* [1999] and given by

$$\hat{I}_{\text{ch}=30}^L = r_u \frac{\int_{\nu_{l0}}^{\infty} \int_{\Omega_A} I(\nu, \Omega, \mathbf{x}) \Phi(\nu) G(\Omega, \Omega_t, \nu) d\Omega d\nu}{\int_{\nu_{l0}}^{\infty} \int_{\Omega_A} \Phi(\nu) G(\Omega, \Omega_t, \nu) d\Omega d\nu} + r_l \frac{\int_{-\infty}^{\nu_{l0}} \int_{\Omega_A} I(\nu, \Omega, \mathbf{x}) \Phi(\nu) G(\Omega, \Omega_t, \nu) d\Omega d\nu}{\int_{-\infty}^{\nu_{l0}} \int_{\Omega_A} \Phi(\nu) G(\Omega, \Omega_t, \nu) d\Omega d\nu}, \quad (2)$$

where  $\hat{I}_{\text{ch}=30}^L$  is the measured radiance for channel 30,  $\nu_{l0}$  is the local oscillator frequency (203267 MHz) within the instrument,  $r_u$  is the higher frequency (relative to  $\nu_{l0}$ ) sideband relative response,  $r_l$  is the lower frequency sideband relative response ( $r_l + r_u \equiv 1$ ),  $I(\nu, \Omega, \mathbf{x})$  is the atmospheric limb radiance,  $\Phi(\nu)$  is the instrument spectral response for channel 30,  $G(\Omega, \Omega_t, \nu)$  is the antenna field-of-view (FOV) response function,  $\nu$  is frequency,  $\Omega$  is solid angle,  $\Omega_t$  is the FOV direction,  $\Omega_A$  is the integration limits in solid angle ( $4\pi$  sr), and  $\mathbf{x}$  is the forward model state vector. The state vector contains the constituent concentrations including humidity  $RH_q$ , temperature  $T$ , FOV direction limb tangent pressure  $\zeta_t$ , and some geometric and hydrostatic quantities for converting tangent pressure into a pointing angle and height. As there is negligible spectral variation across channel 30 in the troposphere, the spectral integrals are neglected and (2) is evaluated monochromatically at the nominal lower and upper sideband frequencies of channel 30. The limb radiance is assumed to have negligible variability across the  $\sim 6$  km horizontal (or azimuth) width of the FOV, and the FOV function

can be collapsed into a one-dimensional function in elevation (or vertical) angle,  $\chi$  ( $G(\Omega, \Omega_t, \nu) \rightarrow G(\chi, \chi_t, \nu)$ ). The FOV integral now in  $\chi$  is evaluated using the convolution theorem for Fourier transforms. The elevation angles  $\chi$  and  $\chi_t$  are computed from the state vector  $\mathbf{x}$ . The “measurement altitude” of the limb radiance line-of-sight path and FOV direction are characterized in the state vector by tangent pressure  $\zeta_t$ .

**2.4.1. Radiative transfer calculation.** The MLS limb radiance  $I(\nu, \mathbf{x})$  is modeled with a nonpolarized, nonscattering, radiative transfer calculation in local thermodynamic equilibrium. The calculation is an integration along the line-of-sight (LOS). The LOS is a path  $s$  beginning at the instrument ( $s = 0$ ) passing through the atmosphere ( $s > 0$ ) and out into space ( $s \rightarrow \infty$ ). The radiative transfer equation is

$$I(\nu, \mathbf{x}) = I_o(\nu) \tau(s = \infty, \nu, \mathbf{x}) + \int_{s=0}^{s=\infty} B(\nu, T(s)) \alpha(\nu, \mathbf{x}, s) \tau(\nu, \mathbf{x}, s) ds, \quad (3)$$

where  $B(\nu, T(s))$  is the Planck blackbody function at  $s$ ,  $T(s)$  is the temperature which is a part of state vector  $\mathbf{x}$ ,  $I_o$  is the cosmic space radiance,  $\tau(\nu, \mathbf{x}, s)$  is the transmission function, and  $\alpha(\nu, \mathbf{x}, s)$  is the absorption coefficient. The transmission function is given by

$$\tau(\nu, \mathbf{x}, s) = \exp \left[ - \int_{s'=0}^{s'=s} \alpha(\nu, \mathbf{x}, s') ds' \right], \quad (4)$$

where  $s'$ , the integration variable, is path length. Equation (3) is solved discretely by layering the atmosphere and replacing the integral with a summation over layers. A convenient way to perform this operation is to use the discrete differential temperature radiative transfer equation [Read *et al.*, 1995]

$$I(\nu, \mathbf{x}) \approx I_t = \sum_{j=t+1}^N \Delta B_j \prod_{k=j}^N \Delta \tau_{kt} - \left( \prod_{k=t}^N \Delta \tau_{kt} \right) \times \left( \sum_{j=t+1}^N \Delta B_j \prod_{k=t}^{j-1} \Delta \tau_{kt} \right) + I_o \left( \prod_{k=t}^N \Delta \tau_{kt} \right)^2. \quad (5)$$

Equation (5) is applied to an  $N - 1$  layered atmosphere where each layer is separated by surfaces with indices running from 1 (the Earth surface) to  $N$  (top of the  $N - 1$  layer and nonabsorbing space). The LOS tangent height is the surface with index  $t$ . Subscripts  $j$  and  $k$  indicate the surfaces used in the products and sums. The differential Planck blackbody radiation quantities  $\Delta B_j$  are  $(B_{j-1} - B_{j+1})/2$ , except when  $j = N$ , where  $\Delta B_N$  is  $(B_{N+1} + B_N)/2$ . The Planck blackbody

radiation energy  $B_j$  is divided by the Boltzmann constant to give the radiance calculation in Kelvins. These units are convenient because the approximate atmospheric temperature at the saturation height of the radiance profile is immediately available. The four product terms are four atmospheric LOS transmissions from layer  $j$  to the instrument, tangent layer  $t$  to the instrument, layer  $j$  to the tangent layer  $t$ , and the total path, respectively.  $\Delta \tau_{kt}$  are the layer transmissions given by

$$\Delta \tau_{kt} = \exp \left[ - \frac{\Delta s_{k \rightarrow k+1}^{\text{refr}}}{\Delta s_{k \rightarrow k+1}} \int_{\zeta_k}^{\zeta_{k+1}} \alpha(\mathbf{x}, \zeta) \frac{ds}{dh} \frac{dh}{d\zeta} d\zeta \right],$$

$$\Delta \tau_{Nt} \equiv 1.0, \quad (6)$$

where  $(\Delta s_{k \rightarrow k+1}^{\text{refr}}) / (\Delta s_{k \rightarrow k+1})$  is the correction for refraction,  $\alpha(\mathbf{x}, \zeta)$  is the absorption coefficient,  $ds/dh$  is the unrefracted path length derivative with respect to height, and  $dh/d\zeta$  is the hydrostatic balance derivative with respect to negative logarithm of pressure. The refraction correction is the ratio of the refracted layer path length to the unrefracted path length. These equations assume the atmosphere is horizontally homogeneous within the  $100 \times 200 \text{ km}^2$  ( $\perp \times \parallel$  to the LOS) measurement footprint. The calculation is performed on a layered atmosphere having 33 nearly equally spaced  $\sim 1 \text{ km}$  thick levels between the surface and 10 hPa. Equation (6) is solved with 8-point Gauss-Legendre quadrature. The tangent height for the radiative transfer calculation is one of 33 levels used for the integrations. The vertical profile of radiances has 33 tangent heights, the same grid used for the integrations. The instrument spectral and spatial effects are computed according to the discussion following (2).

The absorption coefficient includes contributions from the dry and wet continua, and spectral lines of  $\text{H}_2^{18}\text{O}$ ,  $\text{O}_3$ ,  $\text{N}_2\text{O}$ , and  $\text{HNO}_3$ . Contributions from any other gases are thought negligible. The profiles for these species are represented by logarithm basis functions (but with different coefficient “breakpoints”).  $\text{O}_3$ ,  $\text{N}_2\text{O}$ , and  $\text{HNO}_3$  profiles are either climatological values or when available, MLS retrieved values. The wing of the 203.4 GHz  $\text{H}_2^{18}\text{O}$  line contributes weakly to the brightness and is added to the wet continuum. The total absorption coefficient is the sum of line and continuum contributions. The spectral data for lines within 202–204 GHz of the contributing molecules are adequately known.

The retrieval requires radiance derivatives with respect to humidity, which are given by

$$\frac{dI_t}{dF_m^{\text{h}_2\text{O}}} \equiv K_m^{\text{h}_2\text{O}} = \sum_{j=t+1}^N \Delta B_j \prod_{k=j}^N \Delta \tau_{kt} \sum_{k=j}^N \frac{d\Delta \delta_{kt}}{dF_m^{\text{h}_2\text{O}}} - \left( \prod_{k=t}^N \Delta \tau_{kt} \sum_{k=t}^N \frac{d\Delta \delta_{kt}}{dF_m^{\text{h}_2\text{O}}} \right)$$

$$\begin{aligned} & \times \left( \sum_{j=t+1}^N \Delta B_j \prod_{k=t}^{j-1} \Delta \tau_{kt} \sum_{k=t}^{j-1} \frac{d\Delta\delta_{kt}}{dF_m^{\text{h}_2\text{O}}} \right) \\ & + 2I_o \left( \prod_{k=t}^N \Delta \tau_{kt} \right)^2 \sum_{k=t}^N \frac{d\Delta\delta_{kt}}{dF_m^{\text{h}_2\text{O}}}, \quad (7) \end{aligned}$$

where  $\Delta\delta_{kt}$  is the layer opacity which is the argument in the exponential in (6) and  $F_m^{\text{h}_2\text{O}}$  is a humidity coefficient in volume mixing ratio. The layer opacity derivative for the atmosphere above surface  $N$ ,  $d\Delta\delta_{Nt}/dF_m^{\text{h}_2\text{O}} \equiv 0$ .

The forward model requires humidity in volume mixing ratio (VMR) units. Humidity in %RHi is converted to VMR according to

$$F_m^{\text{h}_2\text{O}} = f^{\text{h}_2\text{O}}(rh = 1\% \text{RHi}, \zeta_m) \sum_{q=1}^4 RH_q \eta_q^{\text{rh}}(\zeta_m), \quad (8)$$

where  $f^{\text{h}_2\text{O}}(rh = 1\% \text{RHi}, \zeta_m)$  is the mixing ratio per %RHi at  $\zeta_m$  and its associated temperature. Vertical coordinate  $\zeta_m$  is a  $-\log p$  grid having 17 equally spaced values used in the forward model between the surface pressure and 100 hPa. The uppermost coefficient  $F_{17}^{\text{h}_2\text{O}}$ , which represents water vapor above 100 hPa, is set to 5 ppmv. MLS channel 30 is quite insensitive to stratospheric water vapor, and the assumed value above 100 hPa is unimportant as long as it is less than  $\sim 10$  ppmv.

The following formula, based on the Goff-Gratch function [List, 1951], is used to compute  $f^{\text{h}_2\text{O}}(rh, \zeta_m)$ ,

$$f^{\text{h}_2\text{O}}(rh, \zeta_m) = rh \left( \frac{T}{273.16} \right)^{3.56654} 10^{C(T) + \zeta_m}, \quad (9)$$

where

$$C(T) = a_0 - a_1(273.16/T - 1.0) + a_2(1.0 - T/273.16),$$

$T$  is temperature at  $\zeta_m$  from the National Centers for Environmental Prediction (NCEP), and constants  $a_0 = -1.2141649$ ,  $a_1 = 9.09718$ , and  $a_2 = 0.876793$ .

The retrieval algorithm needs weighting functions for each FOV pointing direction with respect to  $RH_q$  which are related to the derivatives computed by (7) by

$$\begin{aligned} \frac{dI_t}{dRH_q} &= K_{tq}^{\text{rh}} \\ \frac{dI_t}{dRH_q} &= \sum_{m=1}^{17} K_{tm}^{\text{h}_2\text{O}} \frac{dF_m^{\text{h}_2\text{O}}}{dRH_q}. \quad (10) \end{aligned}$$

Differentiating (8) with respect to  $RH_q$  and substituting into (10) gives

$$K_{tq}^{\text{rh}} = \sum_m^{17} \eta_q^{\text{rh}}(\zeta_m) f^{\text{h}_2\text{O}}(rh = 1\% \text{RHi}, \zeta_m) K_{tm}^{\text{h}_2\text{O}}, \quad (11)$$

where  $K_{tm}^{\text{h}_2\text{O}}$  is the weighting function matrix in brightness (K) per VMR (equation (7)) whose rows  $t$  are the measurement tangent pressures and whose columns  $m$  are basis coefficient indices.  $K_{tq}^{\text{rh}}$  is the weighting function matrix (K/%RHi) for the  $RH_q$  coefficients.

**2.4.2. V4.9 dry air continuum.** Parameters in the dry absorption coefficient were estimated from MLS data. The dry air (mostly  $\text{N}_2$  and  $\text{O}_2$ ) continuum absorption coefficient is expected to have the form [Liebe, 1989]

$$\alpha = Ap^2(300/T)^B. \quad (12)$$

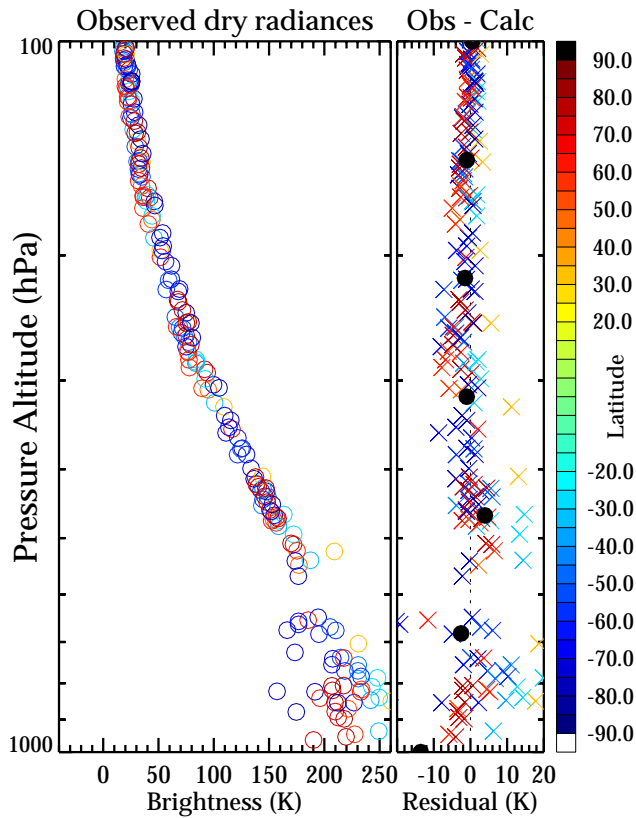
The dry absorption function for V4.9 was established by fitting  $A$  and  $B$  to MLS radiances between 100 and 400 hPa for a limited number of days: January 10, January 15, July 12, July 18, September 17, November 1, in 1992, March 14, 1993, and July 2, 1994. The measurement records for those days were scanned for the smallest 1% of radiance profiles between 400 and 100 hPa. The pointing and atmospheric composition data used for the fit come from archived MLS data except for  $\text{N}_2\text{O}$  which used a simple zonal climatological average. Atmospheric temperature data were taken from NCEP reanalyses data stored in the MLS files with  $\sim 5$  km vertical resolution. Radiometric estimates for  $\text{N}_2\text{O}$  along with  $\text{O}_3$  and  $\text{HNO}_3$  are subtracted from the measured radiances before fitting the dry air function. The resulting fits are  $A = 6.43 \times 10^{-9} \text{ km}^{-1} \text{ hPa}^{-2}$  and  $B = 3.05$ .

Plate 2 shows the the calculated “dry” radiances, and the individual and average difference with the measurements. The scatter of the observed minus calculated radiance differences is large, and its cause is not clearly understood. Possible causes are errors in limb tangent pressure and tropospheric temperatures, neglect of horizontal gradients, residual water vapor contributions, errors estimating contributions from other species like  $\text{N}_2\text{O}$ , and instrument-related artifacts.

**2.4.3. V4.9 water vapor continuum.** The water vapor absorption coefficient in the window region can be written [Bauer et al., 1995; Godon et al., 1992; Bauer and Godon, 1991]

$$\alpha = f^{\text{h}_2\text{O}} Ap^2(300/T)^B, \quad (13)$$

where  $f^{\text{h}_2\text{O}}$  is the water vapor mixing ratio, and  $A$  and  $B$  are frequency-dependent constants. Equation (13) accounts for water-air continuum absorption, including contributions from line wings, and ignores the water-water term which depends on  $(f^{\text{h}_2\text{O}})^2$  and contributes negligibly in the upper troposphere. Values for  $A$  and  $B$  are available from laboratory measurements of water vapor broadened by  $\text{N}_2$  at 213 GHz [Godon et al., 1992]. The wet continuum using these constants was added to the dry function discussed previously along with a contribution from the 203408 MHz  $\text{H}_2^{18}\text{O}$  line.



**Plate 2.** The V4.9 dry absorption function fit: (left) measured radiances (circles, colored by latitude) and (right) differences between the calculated and observed (colored crosses) and the average of the differences binned in 1/6 decade in  $\log P$  thick layers (black bullets).

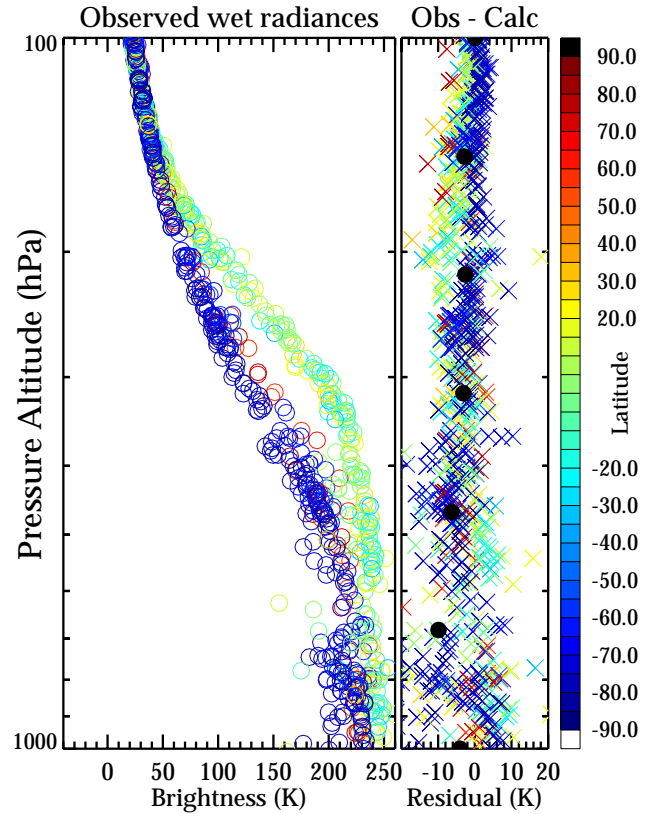


**Plate 3.** The V4.9 wet absorption function fit. The format is the same as in Plate 2.

This combined function was used to calculate MLS radiances as a function of tangent pressure for 100 %RH<sub>i</sub> ( $\text{H}_2^{18}\text{O}$  abundance is  $2.04 \times 10^{-3}$ , the accepted isotopic ratio, times the water vapor abundance for 100 %RH<sub>i</sub>). These calculated radiances were compared to the measured radiances along the right boundary (clear/thin cirrus to thick cirrus atmosphere) of the region marked “WATER VAPOR” in Figure 1; the *Godon et al.* [1992]  $A$  value had to be increased by 15% to fit the MLS data giving  $A = 5.29 \times 10^{-5} \text{ km}^{-1} \text{ hPa}^{-1}$ . There was no evidence that the fit could be significantly improved by having a different temperature dependence from the laboratory measurement. Therefore  $B = 4.2$ , from the *Godon et al.* [1992] laboratory measurement, is used.

A preliminary water vapor retrieval was performed on the same set of days used to fit the dry and wet parameters discussed above. Radiance profiles for retrieved UTH greater than 80 %RH<sub>i</sub> at 147 and 215 hPa, and 60 %RH<sub>i</sub> at 316 and 464 hPa are shown along with the residuals from the fits in Plate 3. A smaller value for the lower two levels was



used because their retrieved values can be biased dry when the upper two levels are moist. The radiances cluster in two groups. The group having the higher radiances are tropical and the group having lower radiances are high latitude. The residuals indicate reasonable agreement between the calculated and observed “wet” radiances.

**2.4.4. V5 combined dry and wet continua fit.** MLS Version 5 data processing incorporates algorithm improvements (N. Livesey et al., manuscript in preparation, 2001), and there are minor changes from V4 in limb tangent pressure, temperature, and stratospheric species. The V5 continuum parameters were determined differently from V4.9. An algorithm was developed which simultaneously fitted the dry and wet absorption coefficient functions, including their temperature dependences. Dry atmospheric radiances were selected, as in the V4.9 fit, and assumed to have 0% RH. The humidity information for fitting the wet atmospheric radiances comes from coincident ( $1^\circ$  by  $1^\circ$  in longitude and latitude and 3 hours in time) Vaisala radiosondes. The radiosonde-measured temperature was used for converting the UTH profile into mixing ratio, and the V5 temperature profile was used for the forward model and retrieval. The V5 temperature vertical resolution is 6  $\zeta$  levels per decade of pressure ( $\sim 2.7$  km) and in the troposphere is the NCEP temperatures interpolated onto the MLS measurement track. The V5 continuum parameters are determined using data from 68 days between October 7, 1991 and August 12, 1996.

The V5 fit gives  $A = 7.30 \times 10^{-9} \text{ km}^{-1} \text{ hPa}^{-2}$ ,  $B = 2.79$  for the dry absorption function and  $A = 5.67 \times 10^{-5} \text{ km}^{-1} \text{ hPa}^{-2}$  and  $B = 3.59$  for the water vapor continuum. Plate 4 shows the results of the V5 fit. The vertically binned averaged residuals are smaller than for V4.9 indicating a better fit. The scatter is still very large, however, even for the dry component and its cause is unknown.

Plate 5 compares the continuum functions from V4.9 and V5 fits with functions from the Liebe MPM models [Liebe et al., 1993; Liebe, 1989], atmospheric transmission measurements from Mauna Kea, Hawaii [Pardo et al., 2001], and laboratory measurements closest to the MLS measurement conditions [Borysow and Frommhold, 1986; Godon et al., 1992, and references therein]. The dry air continuum functions include an  $\text{N}_2\text{—N}_2$  collision induced absorption (CIA) contribution multiplied by 1.29 plus the  $\text{O}_2$  debye contribution. Scaling the  $\text{N}_2\text{—N}_2$  CIA by 1.29 is recommended by Pardo et al. [2001] for including  $\text{O}_2\text{—N}_2$ ,  $\text{N}_2\text{—O}_2$  and  $\text{O}_2\text{—O}_2$  CIAs. The water vapor continuum functions from Liebe [1989], Liebe et al. [1993], and Pardo et al. [2001] include water line by line and continuum contributions calculated at 203 GHz. The laboratory measurement is an  $\text{N}_2$  broadened  $\text{H}_2\text{O}$  absorption measurement at 213 GHz

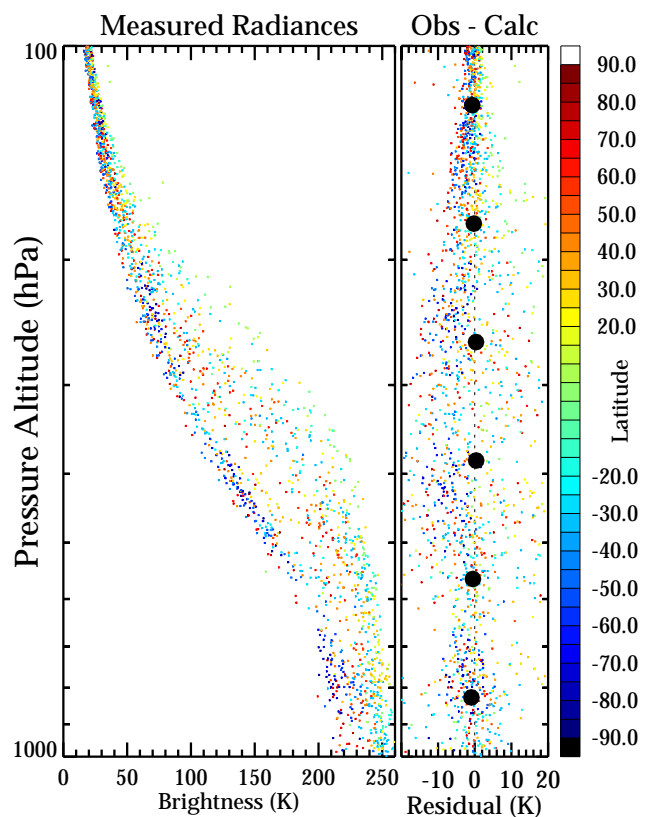


**Plate 4.** The V5 dry and wet absorption function fit. The format is the same as in Plate 2.

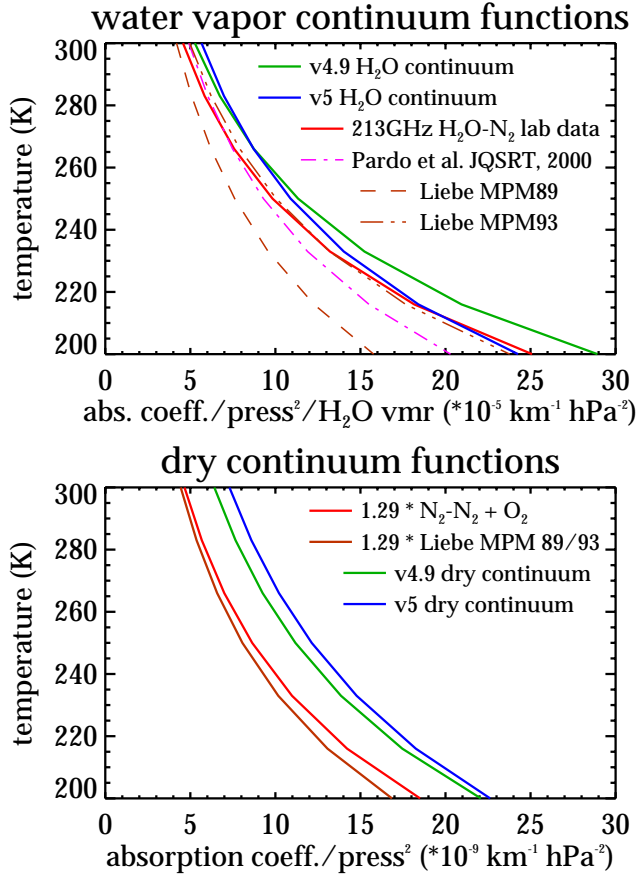


**Plate 5.** Continuum functions fit to MLS data compared to laboratory and model measurements. (top) H<sub>2</sub>O continuum absorption and (bottom) dry continuum absorption divided by pressure squared as a function of temperature. The laboratory data are from *Godon et al.* [1992] for H<sub>2</sub>O, and the dry continuum is based on measurements by *Dagg et al.* [1985, 1978, 1975, 1974], *Stone et al.* [1984], and *Urbanik et al.* [1977]. Results from the MPM89 and 93 models [*Liebe*, 1989; *Liebe et al.*, 1993] and measurements from Mauna Kea, Hawaii [*Pardo et al.*, 2001] are shown.

[*Godon et al.*, 1992]. In all cases, water self-broadening and the absorption from the 203 GHz H<sub>2</sub><sup>18</sup>O line are neglected. The MLS-derived dry continuum functions indicate 20–25% more absorption than the Liebe model and Pardo measurements. Likewise the V4.9 MLS water vapor absorption function at 203 GHz is 16–80% stronger than the other functions. These comparisons show that the MLS-derived absorption functions are reasonable but probably contain artifacts. The in-orbit derivation of these functions will approximately compensate for these artifacts thereby improving the quality of the retrieved UTH. Some of the differences are due to omission of O<sub>2</sub> line wing contributions for the model dry continuum functions. The MLS-derived dry function may include small contributions from water vapor and other atmospheric species. The MLS-derived dry and wet continuum functions are affected by NCEP temperature errors and/or MLS limb tangent errors. The derived functions are also affected by instrumental artifacts such as the yaw cycle dependence which is discussed later.

## 2.5. MLS UTH Retrieval Algorithms

**2.5.1. Version 4.9 retrieval algorithm.** The V4.9 UTH retrieval uses an iterated a priori constrained least squares technique. The UTH profile which best fits the radiances and a priori information is given by

$$\mathbf{RH} = \mathbf{RH}_{\text{initial}} + (\mathbf{y} - \mathbf{y}_{\text{initial}}) \mathbf{S}_y^{-1} \mathbf{K}' \mathbf{S}_{\text{rh}}. \quad (14)$$

$\mathbf{RH}$  and  $\mathbf{RH}_{\text{initial}}$  are the “estimated” and “initial” UTH profiles, respectively. The measurement vectors  $\mathbf{y}$  and  $\mathbf{y}_{\text{initial}}$  are the experimental and calculated (from the initial UTH profile) measurements, respectively.  $\mathbf{S}_{\text{rh}}$  and  $\mathbf{S}_y$  are the covariances of the UTH profile and measurements, respectively.  $\mathbf{K}'$  is the transpose of the measurement sensitivity matrix. Appendix A shows that (14) is identical to optimal estimation [*Rodgers*, 1976, equation (99)].

The measurement vector is composed of MLS limb scan radiances and a priori information,

$$\mathbf{y} = (\text{radiances, a priori UTH profile}). \quad (15)$$

The radiances include all limb emission measurements with tangent pressures greater than 80 hPa. Typically, there are five to six good radiances per limb scan meeting this criteria, and a retrieval is performed only if there are at least four. The a priori UTH profile is 50 %RH<sub>i</sub>. The  $\mathbf{y}_{\text{initial}}$  is of the same form as  $\mathbf{y}$ , where the radiances are computed from the forward model for  $\mathbf{RH}_{\text{initial}}$  with  $\mathbf{RH}_{\text{initial}}$  concatenated to it.

$\mathbf{S}_{\text{rh}}$  and  $\mathbf{S}_y$  are the error covariances of the UTH profile and measurements, respectively. The UTH profile covariance is estimated from

$$\mathbf{S}_{\text{rh}} = (\mathbf{K} \mathbf{S}_y^{-1} \mathbf{K}')^{-1}. \quad (16)$$

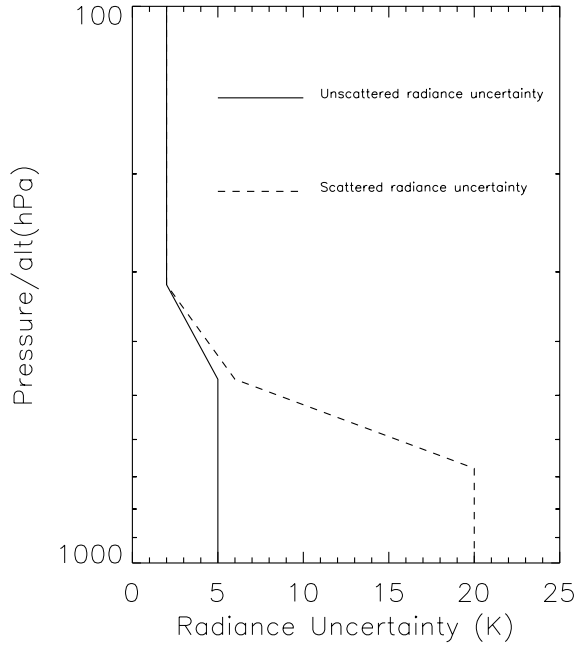


**Figure 3.** Radiance uncertainty profiles for channel 30 used in V4.9 and V5 UTH retrievals. The profile with the smaller values is the nominal uncertainty. The profile with higher values is used when the atmosphere has thick cirrus which scatters the radiation received by MLS.

The measurement error covariance is a block diagonal matrix consisting of radiance and a priori uncertainties,

$$\mathbf{S}_y = \begin{pmatrix} \mathbf{S}_{\text{rad}} & \mathbf{0} \\ \mathbf{0} & \mathbf{S}_{\text{apriori}} \end{pmatrix}, \quad (17)$$

where  $\mathbf{S}_{\text{rad}}$  is the radiance error covariance matrix and  $\mathbf{S}_{\text{apriori}}$  is the UTH a priori error covariance matrix.

Figure 3 shows the radiance uncertainty profiles which are the diagonal elements in  $\mathbf{S}_{\text{rad}}$  for both V4.9 and V5 retrievals. The off-diagonal elements in  $\mathbf{S}_{\text{rad}}$  are assumed zero, a pessimistic assumption because an important error source, the tangent pressure, is correlated throughout the tropospheric scan.

The diagonal elements assumed for the radiance error covariance in clear sky and thin cirrus are 2 K between 80 and 316 hPa increasing to 5 K for tangent pressures greater than 464 hPa. These values are based on the mean residual of the radiance fit to the dry and wet continua rounded to 1 K. The radiance errors modeled in this way are expected to include contributions from limb pressure, temperature, contaminant species, and inadequacy of the continuum parameterization.

Atmospheric scattering of the radiation is another consideration. Noticeable scattering of 202/204 GHz radiation occurs when cloud particle sizes exceed about 100  $\mu\text{m}$ . The MLS radiative transfer forward model does not include scattering and cannot model the brightness temperature depression seen in the lowest altitudes of the scan. Scattering can be detected by an unusually large negative value of observed minus calculated radiance at the lowest altitude scan position. When scattering is detected, the radiance uncertainties are appropriately inflated.

The a priori covariance matrix elements are given by

$$S_{\text{apriori}}(i, j) = 150^2 \exp \left[ \left( \frac{\zeta_i - \zeta_j}{0.25} \right)^2 \right]. \quad (18)$$

The a priori UTH uncertainty is set at 150 %RH<sub>i</sub> with a 4 km correlation length. The diagonal element is made large to minimize a priori influence, except in rare situations where the radiances provide very little information. The 4 km correlation length is chosen to stabilize the retrieval in case the vertical scan becomes irregular.

The measurement sensitivity matrix  $\mathbf{K}$  is constructed as follows,

$$\mathbf{K} = (\mathbf{K}_{\text{th}}, \mathbf{1}), \quad (19)$$

where  $\mathbf{K}_{\text{th}}$  is the instrument weighting function matrix whose elements are given by (11) and  $\mathbf{1}$  is a 4 by 4 unit matrix for the a priori contribution. The forward model is based on the linear approximation,  $\mathbf{y} = \mathbf{y}_{\text{initial}} + (\mathbf{RH} - \mathbf{RH}_{\text{initial}}) \mathbf{K}$ .

The retrieval proceeds as follows: an initial profile for  $\mathbf{RH}_{\text{initial}}$  is input into the forward model which gives  $\mathbf{y}_{\text{initial}}$  and  $\mathbf{K}$ . Equations (14) and (16) give an estimate of  $\mathbf{RH}$  which is iterated until

$$\chi^2 = (\mathbf{y} - \mathbf{y}_{\text{initial}}) \mathbf{S}_y^{-1} (\mathbf{y} - \mathbf{y}_{\text{initial}})^t, \quad (20)$$

is minimized and/or the difference between  $\mathbf{RH}$  and  $\mathbf{RH}_{\text{initial}}$  is negligible.

The first estimate of  $\mathbf{RH}_{\text{initial}}$  is a retrieval of an average %RH<sub>i</sub> over the 1013(surface)–100 hPa vertical range. The single-layer retrieval uses 50 %RH<sub>i</sub> for its initial guess, 50±150 %RH<sub>i</sub> as the a priori, and the “scattered radiance” uncertainty profile from Figure 3. Although the representation basis encompasses the entire troposphere, typically, the retrieved value is indicative of an average relative humidity in a broad vertical layer centered somewhere between the 316 and 215 hPa levels. Initializing the layered retrieval with  $\mathbf{RH}_{\text{initial}}$  from a retrieval of the average humidity in the upper troposphere which is archived in the data files improves the quality of the 464 hPa UTH whose solution is sometimes not unique. The quality of the radiance fit for the single-layer retrieval is used to determine the likely existence of scattering

and, consequently, which of the radiance uncertainty profiles in Figure 3 to use in the final retrieval for each limb scan. If the lowest altitude measured radiance is more than 10K below the radiance calculated from the single-layer retrieval, then scattering is assumed to be present and the “scattered radiance” uncertainty profile is used.

**2.5.2. Version 5 retrieval algorithm.** The V5 UTH retrieval algorithm is essentially identical to that of V4.9. The main difference in the V5 UTH retrievals being due to the parameters used for the dry and wet absorption continua was discussed earlier. The a priori correlation smoothing in V5 is exponential rather than Gaussian as in V4.9. Also, the V4.9 requirement for at least four good radiance measurements at tangent pressures greater than 80 hPa is not imposed in V5: this produces more UTH data, but with some (or all) of the levels relaxed to the a priori value. The V5 estimated uncertainties are set negative whenever their values are greater than 50% of the a priori uncertainty; this indicates significant a priori influence.

## 2.6. Cirrus Effects

One advantage of a microwave experiment is its ability to observe through aerosol, haze, and thin cirrus. Heavy volcanic aerosols have been shown to be completely negligible in MLS signals [Waters *et al.*, 1999]. The interpretation of MLS signals, however, can be affected by clouds and cirrus. Ice particles and water droplets are both emitting and scattering agents. Whenever scattering occurs, the size and shape distribution are important factors in addition to concentrations. Figure 4 shows the relative absorption efficiencies of different H<sub>2</sub>O phases (vapor, liquid, and ice) at 203 GHz. The water vapor absorption function used for Figure 4 is the experimentally derived V4.9 wet continuum function. The ice and liquid absorption functions are empirical functions from Liebe *et al.* [1989]. Ratios greater than 1 indicate that water vapor is a stronger emitter per unit mass density than ice or liquid water. Ice absorbs less than 50% efficiently as vapor but still can be significant. Liquid water is 30–50 times more efficient than vapor. Despite its greater efficiency, liquid water is probably unobservable by MLS, as seen from the radiometric signals characteristic of 100 %RH<sub>i</sub> shown in Plate 3. Under saturated vapor conditions, a necessary condition surrounding clouds, the radiance signals below 400 hPa have values near 240 K indicating the atmosphere has become opaque and MLS does not see the warmer lower troposphere where liquid generally resides. Consequently, we assume that lower altitude clouds containing liquid water do not contribute to the MLS signals.

The maximum water vapor thermodynamically possible is exponentially dependent on temperature according to the Clausius-Clapyron equation. This dependence can be ex-

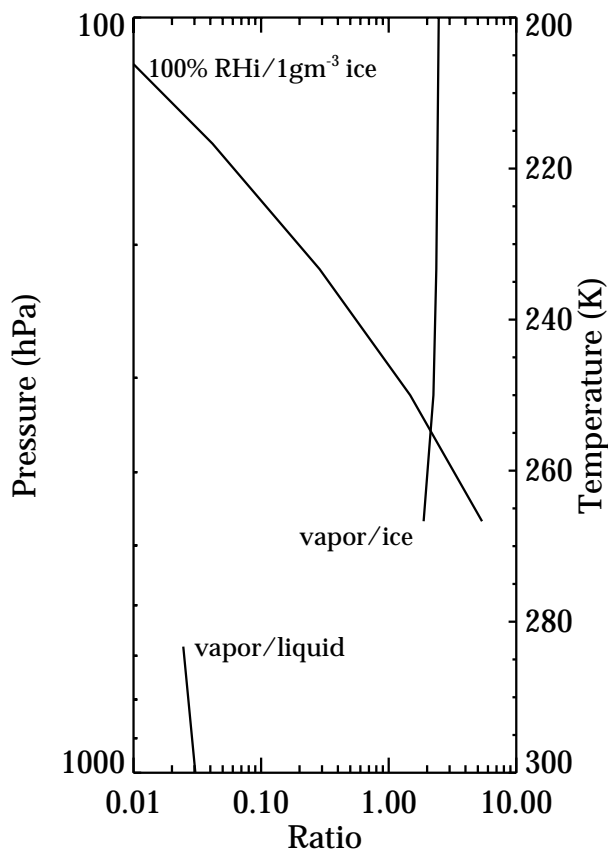


**Figure 4.** Relative efficiencies of different H<sub>2</sub>O phases in absorbing 203 GHz radiation. The curve labeled “vapor/ice” gives the ratio of vapor to ice absorption for the same mass of H<sub>2</sub>O: an equal mass of H<sub>2</sub>O absorbs 203 GHz radiation  $\sim 2\times$  more strongly in the vapor phase than in ice phase. Similarly the “vapor/liquid” curve is the ratio of vapor to liquid absorption for the same mass of H<sub>2</sub>O: an equal mass of H<sub>2</sub>O absorbs 203 GHz radiation only  $0.02\text{--}0.03\times$  as strongly in the vapor as in liquid phase. The curve labeled “100 %RH<sub>i</sub>/1 g m<sup>-3</sup> ice” gives the pressures and temperatures indicated by the y-axes the ratio of absorption by 100 %RH<sub>i</sub> vapor to cirrus having 1 g m<sup>-3</sup> ice water content. These curves neglect scattering.

ploited to interpret MLS signals in the presence of ice when supersaturation or scattering do not occur. We assume ice forms when humidity reaches 100 %RH<sub>i</sub>, and the portion of retrieved UTH in excess of 100 %RH<sub>i</sub> is ice. The minimum detectable ice density (average ice water content (IWC) over the MLS FOV) is  $\sim 0.005 \text{ g m}^{-3}$  at 147 hPa ( $\sim 0.04$ ,  $0.1$ , and  $0.5 \text{ g m}^{-3}$  for the 215, 316, and 464 hPa levels, respectively). Figure 4 shows the absorption ratio of 100 %RH<sub>i</sub> vapor to  $1 \text{ g m}^{-3}$  ice density as a function of height (temperature) in a tropical atmosphere. A cirrus cloud at 147 hPa having  $1 \text{ g m}^{-3}$  ice density will emit 20 times more 203 GHz radiation than vapor at 100 %RH<sub>i</sub>. Although quite high,  $1 \text{ g m}^{-3}$  is not unusual for cirrus associated with a major convective system or hurricane [Pueschel *et al.*, 1995], and these have been seen in the MLS data. If there is no scattering, the  $1 \text{ g m}^{-3}$  IWC cirrus would give a retrieved UTH of  $\sim 2000$  %RH<sub>i</sub> at 147 hPa. Cirrus not associated with convective systems typically have concentrations of  $0.003 \text{ g m}^{-3}$  or less [Knollenberg *et al.*, 1993] and contribute radiance equivalent of 6 %RH<sub>i</sub>. Given the ( $\sim 20\%$ ) uncertainties in the empirical continuum functions, thin cirrus are not expected to contribute significantly to MLS UTH errors.

Cirrus can be distinguished from vapor by comparing measurements from 203 GHz with that from the 186 GHz image sideband of the MLS 183 GHz channel used to measure stratospheric water [Wu, 1998]. Vapor absorption is 6 times larger at 186 GHz than 203 GHz, but ice extinction and scattering have similar values at the two frequencies. A scatterplot of the 186 and 203 GHz radiances shows points falling on two lines: one line with a slope of 1 and the other a slope of  $\sim 7$ . Since these radiances are optically thin, the slopes are a measure of the ratio of the absorption coefficient and/or scattering efficiencies at the two frequencies. The points on the slope of seven are clear-sky signals and those on the unit slope are cirrus. The amount of divergence between these lines is proportional to ice water content and cloud scattering efficiency (whose effects are not separable). A cirrus retrieval based on this method has been performed during the period the 183 GHz operated (October 1991 through April 1993) and produces “MLS cloud index” [Wu, 1998]. The cloud index is equivalent to ice water content (IWC) ( $\text{g m}^{-3}$ ) when no scattering is present. The cloud index overestimates IWC whenever significant scattering occurs, probably the situation for most of the points greater than the cloud index uncertainty ( $0.007 \text{ g m}^{-3}$  at 147 hPa). Plate 6 shows a density plot of V4.9 UTH versus MLS cloud index. The majority of points above 230 %RH<sub>i</sub> are detected as cirrus by the cloud index.

As shown in Plate 6, the peak of the cloud index distribution declines with increasing UTH between 0 and 100 %RH<sub>i</sub>, reaching a minimum near 100 %RH<sub>i</sub> and then slowly

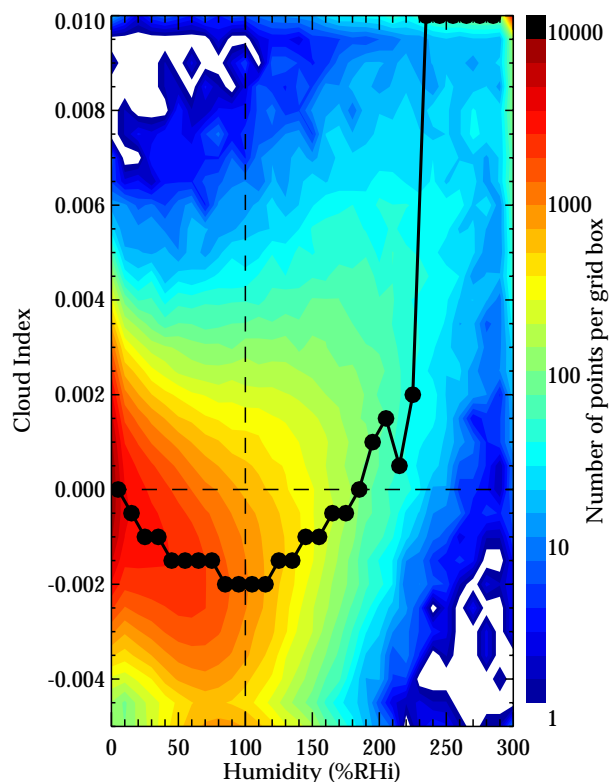


**Plate 6.** A scatter density plot of MLS cloud index versus V4.9 retrieved UTH at 147 hPa between  $40^\circ\text{S}$  and  $40^\circ\text{N}$  for October 1991 through April 1993 when the 183 GHz radiometer was operational. The MLS cloud index is derived from a two-radiometer cloud detection technique described in the text. Data points are collected in an equally spaced 10 %RH<sub>i</sub> by 0.0005 cloud index bins and the color for that bin is the number of points in it. The symbols show the most likely cloud index as a function of MLS %RH<sub>i</sub>.

increasing until 230 %RHi. The cause of the minimum near 100 %RHi is not understood. The cloud index uncertainty associated with this method is 0.007 and therefore is most useful for detecting thicker clouds. The lowest level is 147 hPa where the two-band method provides good vapor/ice separability; it cannot be applied to the lower levels.

Thick cirrus is easily observable by MLS because it scatters the radiation. Scattering is detected by noting the value of the lowest altitude MLS radiance in relation to the radiances above it. If the lowest radiance is colder, or if the radiance profile increases with height, then scattering is likely, and the only explanation if there is a radiance depression of 10 K or more. When this happens, radiation from lower levels will be scattered into the MLS radiometer when its FOV is scanned through a cloud. At higher altitudes, scattering produces warmer radiances than can be explained by a nonscattering forward model, and the retrieved UTH will be several hundred %RHi, correctly indicating the presence of cirrus. Scattering by clouds at lower altitudes causes radiance depression as mentioned previously, and usually corrupts the 464 hPa (and possibly 316 hPa) UTH values.

### 3. MLS UTH Quality and Data Version Differences

#### 3.1. Accuracy, Precision, and Vertical Resolution

MLS UTH accuracy estimates are based on the average of the continuum fit residuals discussed in subsection 2.4. These residuals are a measure of forward model accuracy, which is thought to dominate the resulting absolute accuracy of the retrieved UTH values. The continuum-fit average residuals are typically 2–5 K, much larger than the individual measurement noise of 0.1 K. Values of these residuals were used as the “radiance uncertainty” during the retrievals and propagated through the retrieval algorithm to obtain the UTH accuracy stored in the data file for each profile.

Individual profile accuracy is strongly dependent on humidity. As an example, Plate 7 shows maps of estimated accuracies for the June-July-August (JJA) season. Comparing the accuracies in Plate 7 with the MLS climatologies for the same season (Plates 10–13, discussed later) sometimes show a positive correlation with humidity which is particularly striking at 464 hPa. The accuracy maps are consistent with the behavior of the weighting functions shown in Plate 8. The significant negative correlation of the weighting function with humidity demonstrates the high nonlinearity of the measurement, especially at 464 hPa. The 464 hPa weighting function varies from tens of K/%RHi near 0 %RHi to essentially 0 K/%RHi above 30 %RHi. The 215 and 147 hPa weighting functions tend to be more uniform for all humidity values.

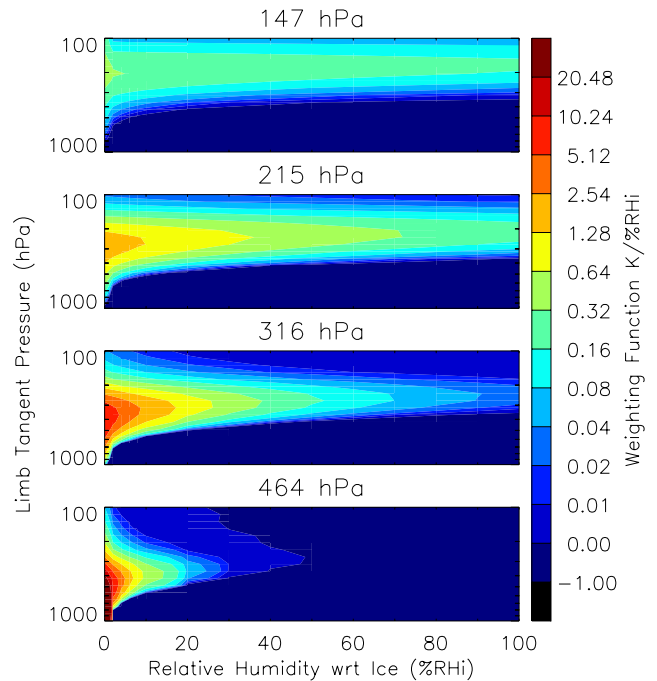


**Plate 8.** UTH weighting functions as a function of relative humidity (horizontal axis) and limb tangent pressure (vertical axis). These are calculated for a typical tropical temperature profile.



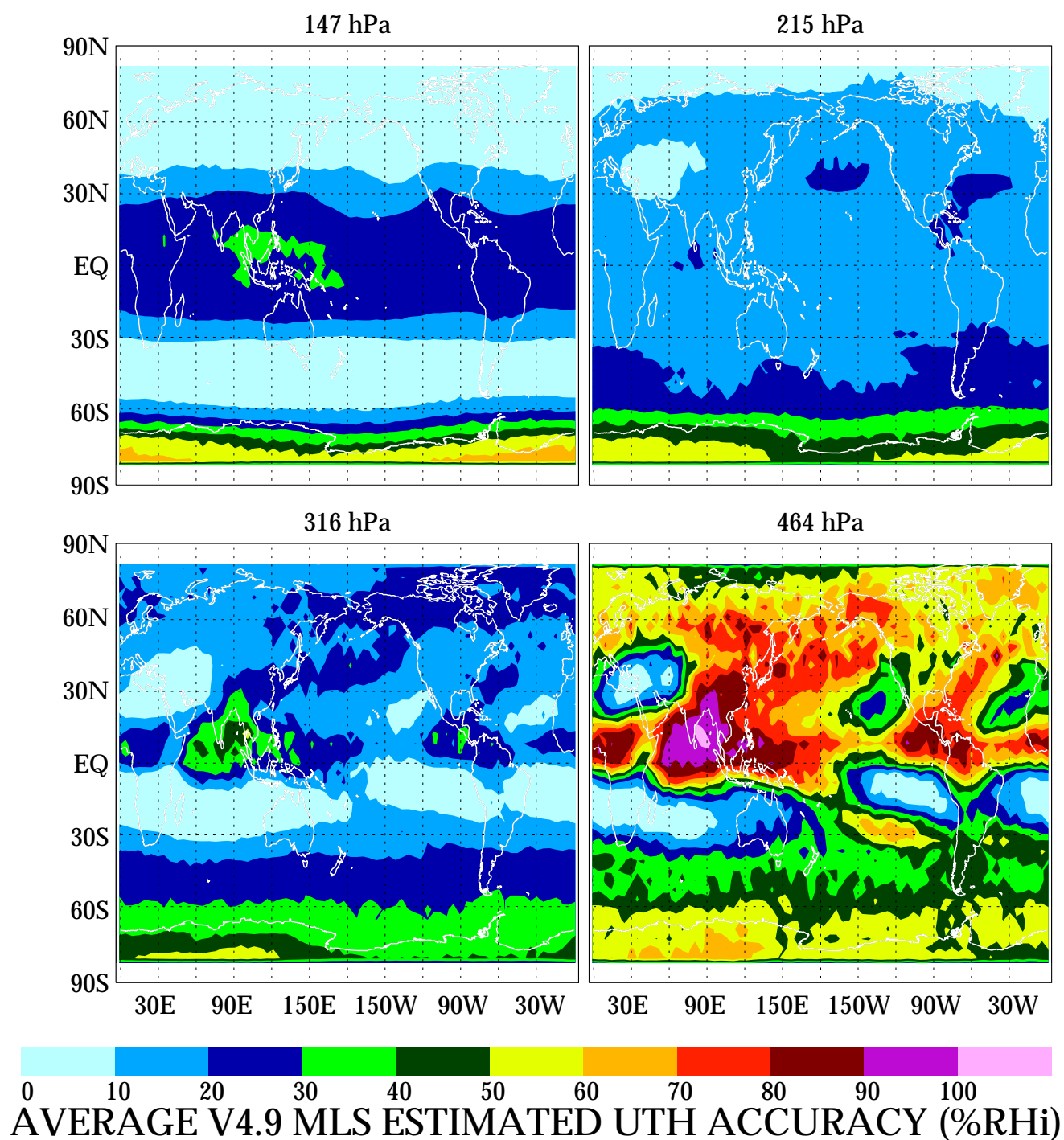


**Plate 7.** Maps of V4.9 MLS estimated UTH accuracies for June-July-August.

**Table 1.** Estimated Accuracy and Precision for MLS V4.9 UTH

Level, hPa	Global		30°S–30°N		30°–60° (S and N)		60°–81° (S and N)	
	Precision, <sup>a</sup> %RH <sub>i</sub>	Accuracy, <sup>b</sup> %RH <sub>i</sub>	Precision, <sup>a</sup> %RH <sub>i</sub>	Accuracy, <sup>b</sup> %RH <sub>i</sub>	Precision, <sup>a</sup> %RH <sub>i</sub>	Accuracy, <sup>b</sup> %RH <sub>i</sub>	Precision, <sup>a</sup> %RH <sub>i</sub>	Accuracy, <sup>b</sup> %RH <sub>i</sub>
147	21	23	32	34	10	10	29	26
215	10	22	15	20	4	21	18	28
316	8	22	6	20	9	22	12	32
464	19	50	20	58	25	49	24	51

<sup>a</sup>Precision: root sum square of contributions from radiance noise, pressure, temperature, and contaminant species precisions.

<sup>b</sup>Accuracy: uncertainty based on the average radiance fit residual to the continuum functions.

The estimated UTH measurement precision is the root sum square of contributions from (1) radiance noise (0.1K), (2) limb tangent pressure (0.15 km), (3) temperature (2K), and (4) contaminant species (0.4 ppmv O<sub>3</sub>, 1.5 ppbv HNO<sub>3</sub>, and 15 ppbv N<sub>2</sub>O). These contributions were propagated through the retrieval to provide an estimate of profile precision. Table 1 gives average individual profile precision and accuracy for MLS V4.9 UTH binned globally and in three broad latitude ranges; V5 values are  $\sim 3$  %RH<sub>i</sub> higher.

Vertical resolution of MLS UTH is highly variable due to the nonlinear nature of the retrieval. Vertical resolution is determined by the vertical representation basis used in the retrieval, vertical smearing by the instrument and measurement geometry (weighting function), instrument noise characteristics, and measurement sampling frequency. The weighting functions for the retrieval basis functions are shown in Plate 8. A typical full width at half maximum (FWHM) of the weighting function is approximately 4 km.

Averaging kernels [Rodgers, 1990] incorporate all aspects of the measurement system affecting resolution. The averaging kernel relates the true atmospheric profile to the retrieved profile according to

$$\mathbf{RH} = \mathbf{RH}_{\text{true}}\mathbf{A} + \mathbf{RH}_{\text{a priori}}(\mathbf{I} - \mathbf{A}), \quad (21)$$

where  $\mathbf{RH}$  is the retrieved humidity (equation (14)),  $\mathbf{RH}_{\text{true}}$  is the atmospheric humidity,  $\mathbf{RH}_{\text{a priori}}$  is the a priori relative humidity, and  $\mathbf{A}$  is the averaging kernel matrix which is computed from the instrument weighting functions, measurement noise, and a priori uncertainties.  $\mathbf{A}$  for MLS UTH is a 4 by 4 square matrix whose elements along a row can be thought of as a vertical smoothing function of the measurement system. The FWHM of MLS UTH smoothing function is the best measure of vertical resolution of the UTH measurement with the following reminders: (1) the averaging kernel depends on the a priori uncertainties and (2) the averaging kernel calculation assumes the atmosphere is accurately represented by the retrieval representation basis. A

perfect measurement system has a unit matrix for  $\mathbf{A}$ . Off-diagonal elements indicate degradation of resolution. The averaging kernel gives the smoothing function among the breakpoints of the vertical profile basis and therefore indicates the half width at half maximum for the top (147 hPa) and bottom (464 hPa) coefficients.

Plate 9 shows averaging kernel contours overlayed on the MLS V4.9 June-July-August zonal mean UTH climatology. The plot gives some indication of how these contours vary with humidity. The solid lines enclose the regions where the averaging kernel exceeds 0.9, indicating negligible a priori influence. The dashed lines indicate where the averaging kernel is 0.5. The FWHM (resolution) for a coefficient is the vertical distance between its 0.5 contours. Only one 0.5 averaging kernel contour is appropriate for the 147 and 464 hPa coefficients. Since the averaging kernel calculation assumes the UTH in the atmosphere is modeled according to Figure 2, the averaging kernels provide no information on the lower altitude limit of the 464 hPa coefficient or the upper altitude limit of the 147 hPa coefficient. The resolution of the 464 and 147 hPa coefficients are estimated from the vertical distance between the 0.5 averaging kernel contour and the lower 464 hPa and upper 147 hPa weighting function half maximum contour, also shown in Plate 9. Resolution is best when the 0.5 averaging kernel contours have little or no overlap among the coefficients which occurs when the atmosphere is driest as shown near 20S. The 147 and 215 hPa coefficients produce well-resolved kernels for the wide range of atmospheric conditions shown here except for Antarctic winter where very low temperatures can cause some a priori influence. MLS UTH sensitivity is more constant in mixing ratio than in %RH<sub>i</sub>. Very low temperatures at fixed %RH<sub>i</sub> uncertainties reduce the a priori uncertainty and more tightly constrain the retrieval. This manifests itself by reducing the peak value and broadening the averaging kernel as shown in Plate 9. Therefore the sensitivity and resolution of the measurement system in relative humidity are not as good when temperature is less than 200 K. The upper 464 hPa averag-



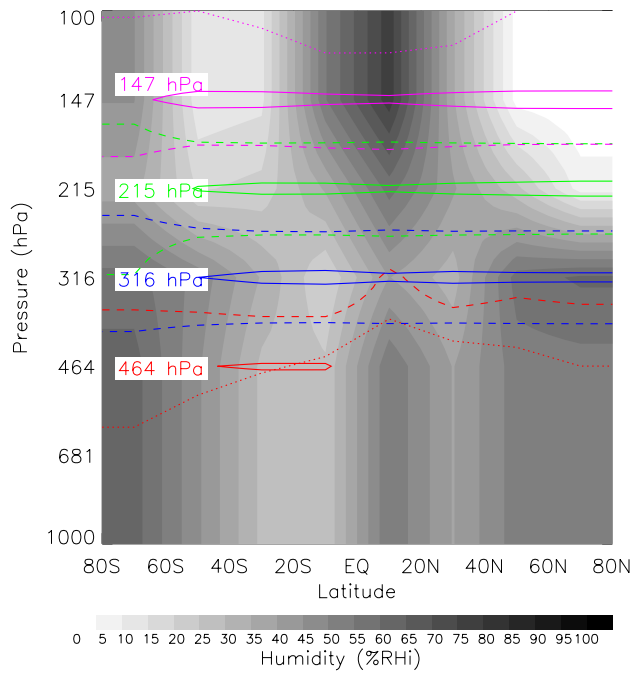


**Plate 9.** Peak and width contours of MLS averaging kernels and weighting functions overlaid on the MLS June-July-August UTH zonal mean climatology. The four MLS retrieval levels are individually colored. The solid lines enclose the region where the averaging kernel exceeds 0.9 (little a priori influence), and the thick dashed lines are locations of their half maximum. For reasons discussed in the text only the locations of the half maximum value for the lower side of the 147 hPa averaging kernel, and the upper side of the 464 hPa, are shown; the dotted lines for these levels give weighting function half value points on the upper and lower sides, respectively. The vertical distance between dashed and/or dotted curves of the given color give the approximate vertical resolution for that level.

ing kernel 0.5 contour overlaps the lower 316 hPa 0.5 averaging kernel contour with increasing humidity. This means that the 464 hPa humidity coefficient is having its effective height shifted toward 316 hPa. The 147 hPa level has its best resolution over the tropics where the vertical gradient in absorber density is greatest. This behavior is expected when the radiometric signal is optically thin. The transition to optically thick radiance occurs between 900 and 350 hPa depending on humidity. When the atmosphere between 500 and 300 hPa is very moist, the 464 hPa coefficient is almost entirely obscured and somewhat degenerate with the 316 hPa level. This is evidenced by the 464 hPa lower altitude weighting function half maximum contour being above 464 hPa in the tropics, and its averaging kernel 0.5 contour having considerable overlap with the 316 hPa averaging kernel.

### 3.2. Comparisons Among the Different MLS Data Versions

Average differences between the UTH preliminary version and V4.9 based on a small number of days have been previously published by *Sandor et al.* [1998] in mixing ratio units. Here we compare, in %RH<sub>i</sub> units, the preliminary and V4.9 UTH for all data in 1992 and 1993. The V4.9 data were screened according to the procedures described in section 4, and the preliminary version data were screened by positive uncertainty (negative MLS uncertainties indicate unusable data for both the preliminary version and V4.9). Results of the comparisons are given in Table 2, presented as bias and scaling differences. The bias is the intercept and the scaling is the slope obtained from a linear regression analysis. The scatter between the versions is shown in Figure 5. Differences between the preliminary version and V4.9 are mainly due to the inferior algorithms and the dry continuum used in the preliminary version.

Table 3 and Figure 6 give results of analogous comparisons between V4.9 and V5, again for all data taken in 1992 and 1993. The V4.9 and V5 use essentially the same forward model, retrieval algorithm, and method of determining parameters for the dry air continuum. The significant difference in these versions is the method by which the water vapor continuum parameters were obtained, as described previously (V5 used Vaisala radiosondes for determining H<sub>2</sub>O profiles, whereas V4.9 did not use Vaisala radiosondes for this purpose). The bias differences are relatively small, with scaling accounting for most of the differences.

**Table 2.** Bias and Scaling Factors Between the Preliminary Version and V4.9 UTH<sup>a</sup>

Level, hPa	Global		30°S–30°N		30°–60° (S and N)		60°–81° (S and N)	
	Bias, %RH <sub>i</sub>	Scaling	Bias, %RH <sub>i</sub>	Scaling	Bias, %RH <sub>i</sub>	Scaling	Bias, %RH <sub>i</sub>	Scaling
147	40.9	0.59	45.4	0.49	25.0	0.67	47.4	2.33
215	49.3	0.97	39.1	0.63	42.6	1.15	74.3	3.82
316	17.3	0.52	12.5	0.24	18.5	0.32	38.9	0.67
464	18.4	0.29	4.5	0.00	15.5	0.14	33.2	0.31

<sup>a</sup>Preliminary version %RH<sub>i</sub> = bias+scaling×(V4.9 %RH<sub>i</sub>).

**Table 3.** Bias and Scaling Factors Between V5 and V4.9 UTH<sup>a</sup>

Level, hPa	Global		30°S–30°N		30°–60° (S and N)		60°–81° (S and N)	
	Bias, %RH <sub>i</sub>	Scaling	Bias, %RH <sub>i</sub>	Scaling	Bias, %RH <sub>i</sub>	Scaling	Bias, %RH <sub>i</sub>	Scaling
147	−8.2	0.99	−13.0	1.01	−4.0	0.81	−2.0	0.74
215	−1.6	0.92	−2.0	0.97	−1.4	0.91	−1.5	0.66
316	1.6	0.83	0.8	0.90	2.2	0.81	0.5	0.81
464	4.5	0.73	5.4	0.82	5.2	0.73	−0.8	0.72

<sup>a</sup>V5 %RH<sub>i</sub> = bias+scale×(V4.9 %RH<sub>i</sub>).

## 4. Caveats, Artifacts, and Recommendations for Using MLS UTH Data in Scientific Studies

### 4.1. Caveats for Using the MLS UTH Data

There are three caveats investigators should be aware of when using MLS UTH data: (1) horizontal area footprint and unaccounted errors caused by a forward model simplification, (2) dry bias in 316 hPa and 464 hPa UTH values, and (3) temperature sensitivity of absolute humidity derived from relative humidity.

The MLS horizontal footprint is approximately  $100 \times 200$  km<sup>2</sup> ( $\perp \times \parallel$  to the LOS), and the forward model and retrieval algorithms assume horizontal homogeneity. Horizontal UTH variability will add some retrieval error which is not included in either the precision or accuracy estimates given here.

Retrieval simulation studies have demonstrated that humidities greater than 70 %RH<sub>i</sub> at 316 hPa and 60 %RH<sub>i</sub> at 464 hPa are underestimated. The exact cause of this behavior is not understood. In some situations a priori influence may bias the retrieval towards lower humidities. We expect the same behavior in actual atmospheric retrievals.

The MLS UTH measurement in %RH<sub>i</sub> is less affected by temperature errors than its corresponding absolute humidity. The absorption strengths for the dry background and water vapor continua were determined from a limited num-

ber of MLS radiance measurements where the %RH<sub>i</sub> and the temperature of the atmosphere were assumed known. Temperature errors are thus approximately compensated by the continua, making the measured %RH<sub>i</sub> generally insensitive to an NCEP temperature bias if one exists; however, this is not true for absolute UTH. Scientific investigations or assimilations should either use MLS UTH in %RH<sub>i</sub> or convert the MLS UTH in %RH<sub>i</sub> to absolute humidity using temperature data associated with their analysis and not the MLS temperature used in the retrieval.

### 4.2. Artifacts in MLS UTH Data

There are currently four known artifacts associated with the MLS UTH: (1) unphysically high humidity retrievals, sometimes occurring at 147 and 215 hPa, (2) erroneously low retrievals at 316 and 464 hPa, (3) unusual behavior of stratospheric-like concentrations at 147 hPa, mid-high latitudes, and (4) a yaw cycle artifact at 147 hPa.

The MLS UTH product is insensitive to thin cirrus which does not degrade its quality. Thick cirrus usually scatters the radiation. Retrieved 147 and 215 hPa UTH in thick cirrus exceeds 230 %RH<sub>i</sub>, sometimes giving values in the thousands of %RH<sub>i</sub>. Thick cirrus is detected when 147 hPa UTH is greater than 230 %RH<sub>i</sub> ( $> 0.007$  g m<sup>−3</sup> density average over the MLS FOV) and/or the calculated radiance at the lowest altitude pointing is more than 10.0 K warmer than

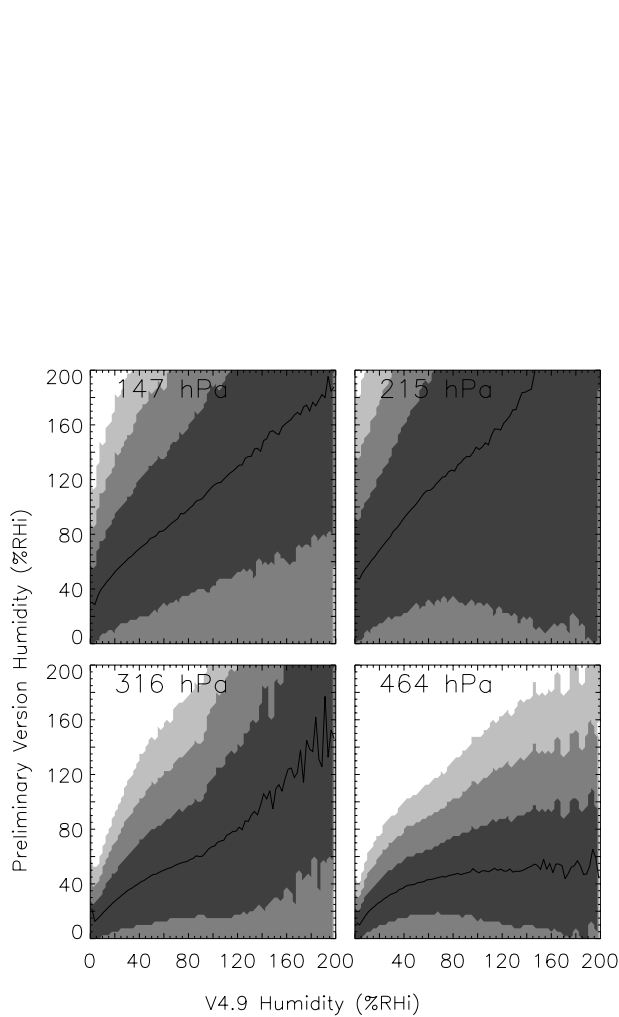


**Figure 5.** A comparison between UTH version 4.9 and the preliminary version for all measurements taken in 1992 and 1993. The black line is the mean preliminary version %RH as a function of V4.9 %RH; each shade from dark to light indicates 1, 2, and 3 standard deviations of the scatter about the mean.

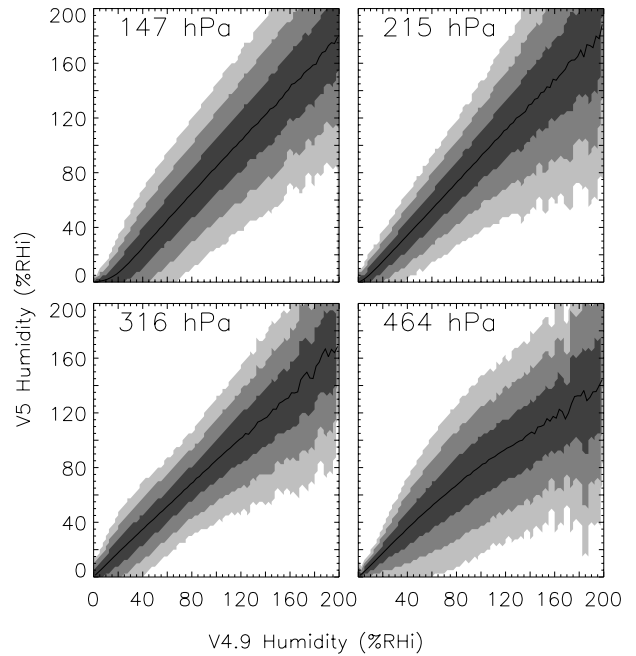


**Figure 6.** Same as Figure 5, but for UTH versions 4.9 and 5.

that measured.

Numerical simulations have demonstrated that erroneously low retrieved UTH can occur at 464 hPa. This problem was significantly reduced but not eliminated, by using the two-stage retrieval procedure discussed earlier. In retrievals of real data we also noted that both the 316 and 464 hPa levels can have unrealistically low values, primarily due to the retrieval solution not always being unique. This problem tends to occur when the 147 and 215 hPa levels are very moist, causing poor sensitivity to the 316 and 464 hPa levels. An effective method for eliminating this artifact is to compare the 316 hPa and 464 hPa UTH to the single-layer retrieved value used for the first guess and reject the 316 or 464 hPa data if those levels are more than 5 %RH drier than the single-layer value. A scattering cloud also produces erroneously low retrievals at 316 and 464 hPa by depressing the radiance on the low-altitude portion of the scan. Screening the 316 and 464 hPa retrieved relative humidity against the initial guess as described is an effective method for eliminating cloud corrupted data at the lower two levels. Using a low-altitude radiance depression of 10 K or more as indicating cloud scattering, hence unreliable retrievals at 316 and 464 hPa, and comparing it to the total number of rejected 316 and 464 hPa retrievals shows that only 10% of these are caused by cloud scattering.

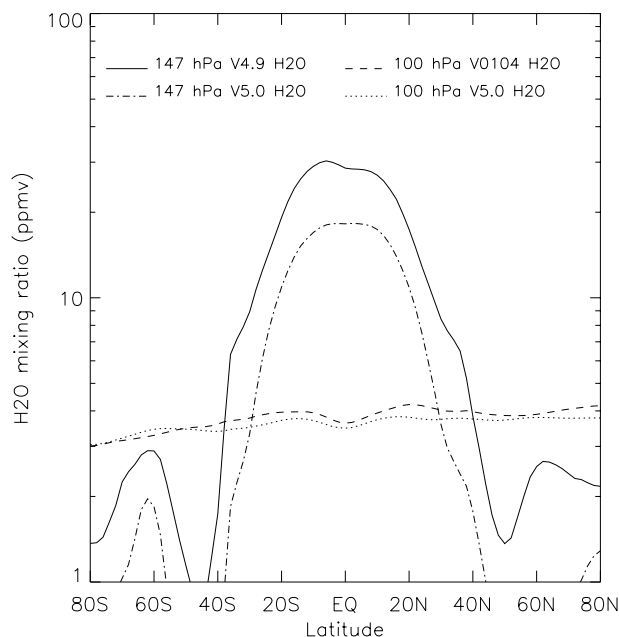


**Figure 7.** Comparison of MLS upper tropospheric and lower stratospheric zonal average  $\text{H}_2\text{O}$  mixing ratios for 50 days throughout 1992. The highest tropospheric level (147 hPa) and lowest stratospheric level (100 hPa) are each shown for the two indicated versions of both tropospheric and stratospheric data. The MLS 147 hPa  $\text{H}_2\text{O}$  shows unphysical behavior at abundance levels of a few ppmv, consistent with its expected accuracy being not better than  $\sim 8$  ppmv. The MLS UTH versions to date therefore are not considered sufficiently reliable for connecting these data to lower stratospheric  $\text{H}_2\text{O}$  data.

MLS UTH versions to date exhibit unusual behavior of a few parts per million by volume (ppmv) which is significant for stratospheric abundances. The estimated accuracy of the uppermost 147 hPa UTH level is not better than 8 ppmv, worse than typical values of lower stratospheric  $\text{H}_2\text{O}$ , and it shows some unphysical behavior. Figure 7 compares MLS 147 hPa  $\text{H}_2\text{O}$  zonal average mixing ratios with 100 hPa mixing ratios [Pumphrey, 1999] obtained from the separate 183 GHz MLS radiometer that provides stratospheric  $\text{H}_2\text{O}$ . The MLS 147 hPa  $\text{H}_2\text{O}$  shows apparently artificial dips to  $\sim 1$  ppmv near  $50^\circ\text{S}$  and  $50^\circ\text{N}$  which are not present in the 100 hPa zonal average.

The 147 hPa UTH retrievals contain an artifact associated with the UARS yaw cycle. Variations in solar illumination of the MLS antenna and instrument through the yaw cycle can,

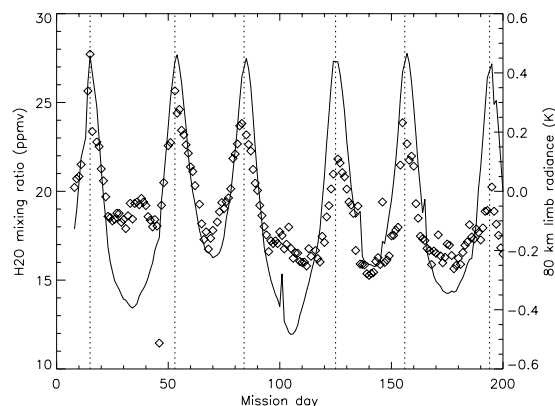


**Figure 8.** Daily 147 hPa  $30^\circ\text{S}$ – $30^\circ\text{N}$  retrieved  $\text{H}_2\text{O}$  average (diamonds) and measured brightness near 80 km (solid line). Dotted vertical lines indicate UARS yaw maneuver days. Mission day 0 is September 12, 1991.

by variations in heating and possibly other effects, produce small artifacts in the radiances. Figure 8 compares daily  $30^\circ\text{S}$ – $30^\circ\text{N}$  averages of the MLS observed 202 and 204 GHz radiances at 80 km tangent height and the retrieved 147 hPa  $\text{H}_2\text{O}$  mixing ratio. Radiances at 80 km and 202/204 GHz should be the cosmic background (0.28 K in our units), but a peak-to-peak yaw cycle variation of  $\sim 0.8$  K brightness is observed which correlates with a  $\sim 10$  ppmv peak-to-peak variation in average 147 hPa  $\text{H}_2\text{O}$  mixing ratio. The  $\text{H}_2\text{O}$  variability is consistent with the radiance variability. This artifact is not observed at 215 hPa and lower levels.

#### 4.3. Data Usage Recommendations

The MLS UTH data are archived at the Goddard Distributed Active Archive Center in two formats: L3AT and L2. The L3AT file is the standard geophysical products data file used by all UARS profiling instruments. The V4.9 UTH L3AT files have UTH values from 1000 to 147 hPa in six levels. UTH values at 1000 and 683 hPa are set equal to the retrieved 464 hPa coefficient. The MLS UTH L2 file is an ASCII file which contains UTH profiles in %RH, mixing ratio (ppmv), temperature (K, from NCEP analyses), estimated

UTH error covariance, measured and calculated MLS channel 30 radiances and other retrieval diagnostics. We recommended using the L2 file because it has the single-layer humidity retrieval (first guess for the layered retrieval) needed to screen the 316 and 464 hPa data. Version 4.9 is currently believed to be the best MLS UTH data version. Recommendations for use of these data are the following:

1. Assume any MLS UTH > 120%RH<sub>i</sub> to be indicative of the presence of cirrus and set the value to 100 %RH<sub>i</sub>.
2. Reject any 316 or 464 hPa UTH that is more than 5 %RH<sub>i</sub> less than the single-layer retrieved value (in L2 file).
3. Never use V4.9 UTH accompanied with a negative uncertainty.
4. If possible, use an auxiliary cloud data set to reject 316 and 464 hPa level retrievals whenever thick upper tropospheric clouds are present.

## 5. MLS V4.9 Climatology and Comparisons With Other UTH Climatologies

### 5.1. MLS V4.9 UTH Climatology

The V4.9 UTH seasonal climatologies are given in Plates 10–13 at the four MLS UTH surfaces. These climatologies include all data from September 1991 through June 1997. The data have been averaged in 5° longitude by 4° latitude bins and screened according to section 4. All four levels show the moistening in the Intertropical Convergence Zone (ITCZ) and its expected seasonal behavior. The upper troposphere over tropical land masses is wetter than over the oceans, and the Indian monsoon shows in the June–July–August (JJA) season. The relative humidity at 147 hPa is very low outside the tropics except at high latitudes during the Southern Hemisphere winter. The high relative humidities over the Antarctic during JJA may be associated with polar stratospheric clouds. The tropics show a decrease in %RH<sub>i</sub> from 464 to 316 hPa, which is similar to other satellite climatologies [Soden and Lanzante, 1996] but an increasing relative humidity from 316 hPa up to 147 hPa reaching nearly 100 %RH<sub>i</sub> at 147 hPa.

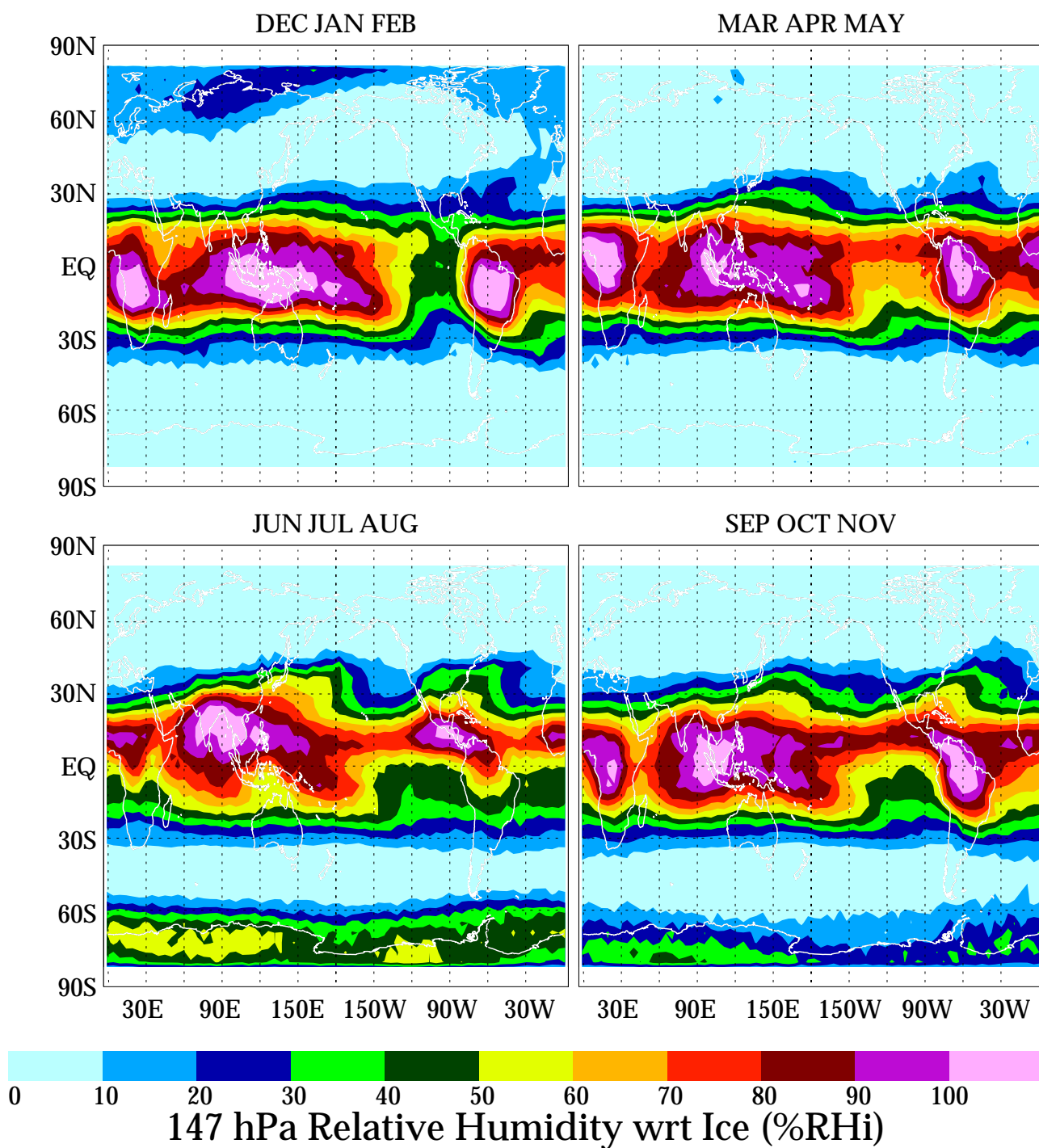
### 5.2. Comparison With Vaisala Radiosonde Climatology

The global radiosonde network provides a rich supply of data. Radiosondes are typically launched by balloon and contain sensors measuring pressure, temperature, humidity, and wind velocity. The data, typically taken on ascent, are radioed to the monitoring site, processed, and archived into files binned by universal time (UT) in 6-hour increments (0000, 0600, 1200, and 1800) for each day. These data for the entire UARS mission are available from the UARS Central Data and Handling Facility (CDHF). Reporting sta-

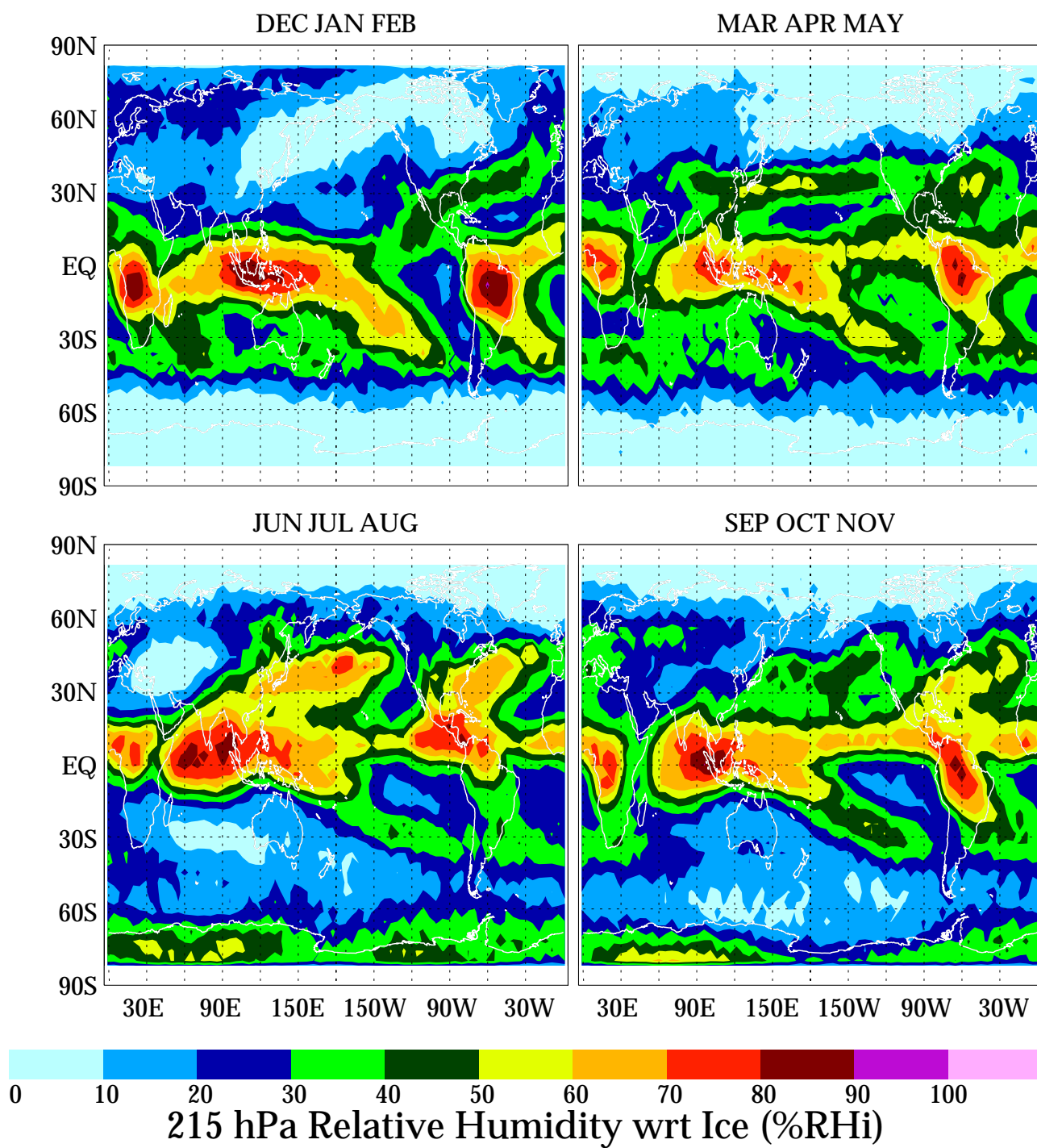
tions are required to provide data (when available) on predefined mandatory levels (1000, 850, 700, 500, 400, 300, 250, 200, 150 hPa, and several levels above). Humidity is archived as dewpoint depression which we convert to H<sub>2</sub>O vapor pressure using the Wexler expression of *Elliot and Gaffen* [1991]. H<sub>2</sub>O partial pressure is converted to %RH<sub>i</sub> or mixing ratio based on (9) using the radiosonde temperature measurement. In practice, a radiosonde network within a country uses its own function to convert relative humidity with respect to water (%RH<sub>w</sub>) into dewpoint depression. Many of these functions are given by *Gaffen* [1993]. The archived records have dewpoint depressions greater than 5°C rounded to the nearest degree. The variability among the functions can be ignored because it is usually less than the reporting precision [*Elliot and Gaffen*, 1993]. The radiosonde measurement after converting to %RH<sub>i</sub> is linearly interpolated onto the four MLS surfaces, for comparisons. Since the NCEP mandatory levels are of comparable resolution to the MLS retrieval surfaces, linear interpolation in %RH<sub>i</sub> is considered adequate for the comparison. The Vaisala radiosonde measurement is a point value in height with an effective vertical resolution of 0.5 km at -50°C (due to sensor response time [*Paukkunen*, 1995]) that is archived on an approximately 2 km vertical grid in the upper troposphere.

A good discussion regarding the quality of radiosonde humidity measurements is given by *Larsen et al.* [1993] who used them for validating the SAGE II upper tropospheric H<sub>2</sub>O measurements. The major issue with radiosondes generally is how quickly they respond to humidity changes, which becomes an increasingly severe problem at temperatures below -40°C. The SAGE II validation showed that the Vaisala thin film capacitive radiosonde, the best currently available with the fastest response time [*Schmidlin*, 1988], consistently yielded much better agreement (5–20%) than the other radiosonde detectors, even after screening out reporting biases and suspected bad data points. Based on the SAGE II experience, we only used the Vaisala radiosonde for comparisons.

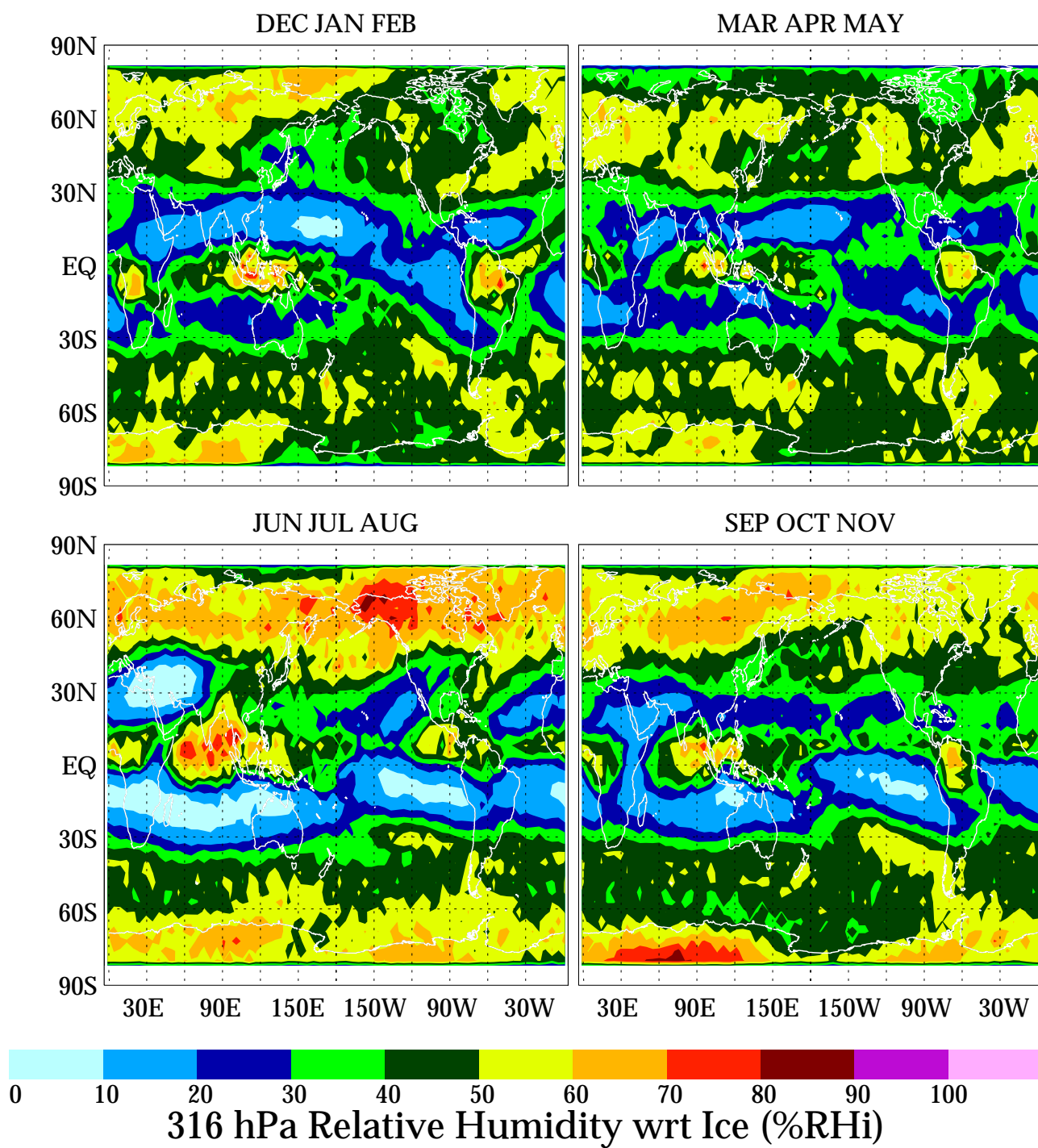
There currently exist three Vaisala instrument types: RS80-A, RS80-H, and RS90. These types are not distinguished in the data archive, which is unfortunate because the raw data from the A type has a severe dry bias at low temperatures that is not present in the H type. The dry bias in A type Vaisala sondes reported by *Miloshevich et al.* [2001] is based on comparisons with a simultaneously flown frostpoint hygrometer and cloud particle replicator. The ratio of the frostpoint relative humidity to that of the A-type Vaisala is 1.1, 1.3, 1.6, 2.0, and 2.4 at -20°C, -35°C, -50°C, -60°C, and -70°C, respectively. These ratios only apply to the raw data and not necessarily to the archived data which may have un-



**Plate 10.** MLS V4.9 UTH climatology (September 1991 through June 1997) at 147 hPa divided into four seasons. The data were screened according to the method described in section 4.

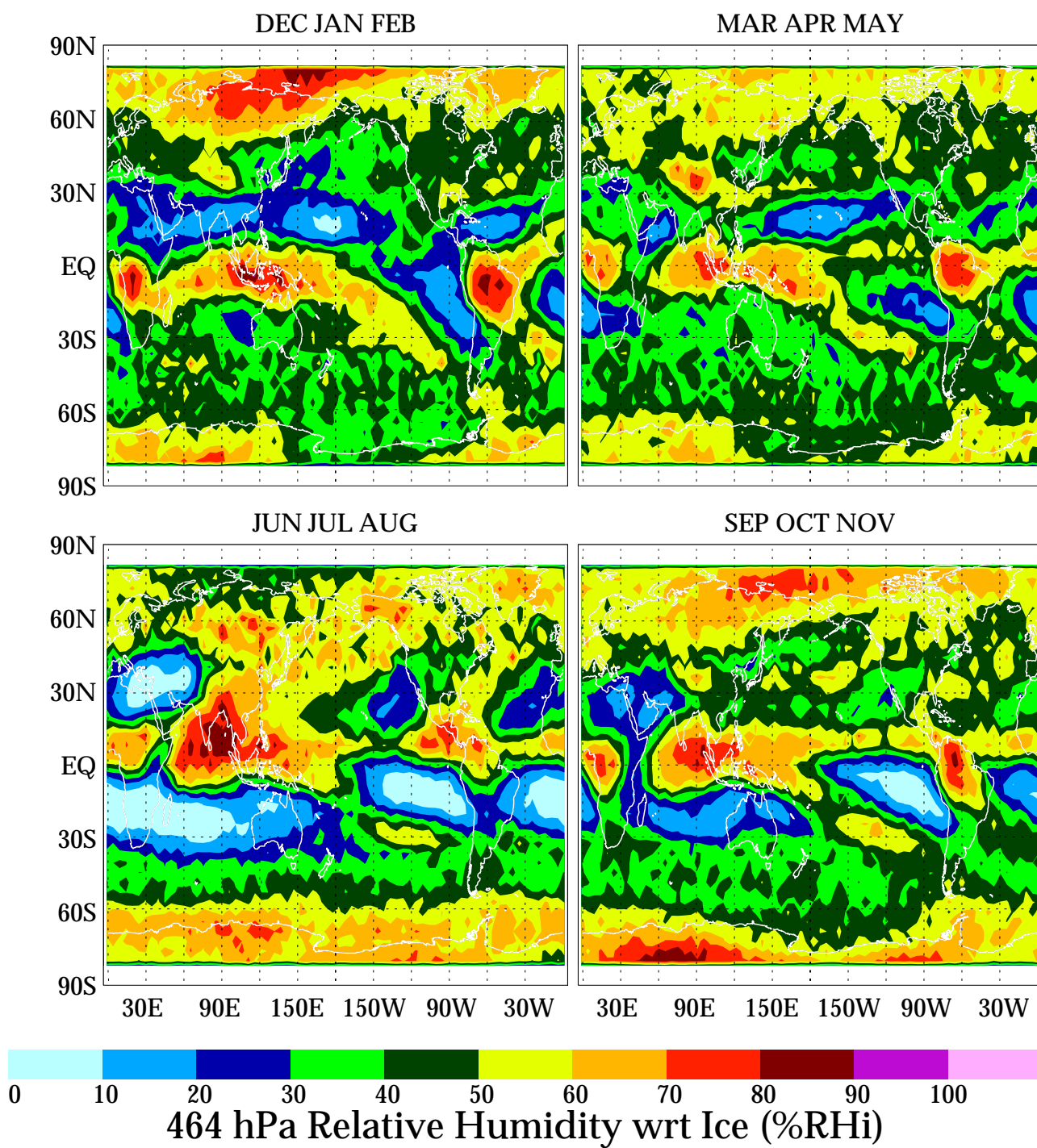
**Plate 11.** Same as Plate 10, but for 215 hPa.





**Plate 12.** Same as Plate 10, but for 316 hPa.



**Plate 13.** Same as Plate 10, but for 464 hPa.

dergone some additional processing [e.g., Anderson, 1994]. The H type has a much smaller bias relative to the frostpoint hygrometer and the Vaisala RS90 even smaller. The H type became available in 1993 but is slowly working its way into the radiosonde network because of added expense associated with its data acquisition and processing system. The RS90 sonde became available after 1997. Most of the MLS validation data are prior to 1994. For these reasons and lack of other information we assumed that the archived Vaisala data are from the A-type instrument.

Plate 14 compares MLS and Vaisala zonal mean UTH climatologies for the period of September 1991 through June 1997. A similar figure is given by Peixoto and Oort [1996] for radiosondes (incorporating all sensor types), but with the uppermost altitude at 300 hPa. The Peixoto and Vaisala climatologies are generally similar but quantitatively different, probably a consequence of our using relative humidity with respect to ice (rather than water) and a subset (Vaisala only) of the radiosonde data. The MLS zonal mean relative humidities are similar but drier than those from the Vaisala radiosonde which may be caused by MLS underestimating humidity at 316 and 464 hPa when humidity exceeds 70 %RHi and possibly a sampling difference where most of the radiosonde measurements are taken over land, whereas MLS has measurements over both land and ocean. Peixoto and Oort [1996] show the land-ocean contrast should not exceed 10 %RHw above 500 hPa. The seasonal shifts are present, and the Southern Hemisphere winter subtropics are drier than the Northern Hemisphere winter subtropics in the MLS data. This difference between DJF and JJA is not present in the Peixoto and Oort [1996] climatology.

An interesting feature present in both the MLS and Vaisala measurements is the inverted profile in the tropics which shows relative humidity increasing with height above 316 hPa. This feature is not observed in operational nadir sounding satellites [Spencer and Braswell, 1997; Soden and Bretherton, 1996] which are not sensitive to water vapor above 250 hPa. The high tropical 147 hPa %RHi and inverted profile measured by MLS and Vaisala radiosondes are consistent with high occurrence of tropical subvisible cirrus (SVC) at 15 km in a 3 km thick layer observed by SAGE II [Wang et al., 1996] and Cryogenic Limb Array Etalon Spectrometer (CLAES) [Mergenthaler et al., 1999; Jensen et al., 1999; Sandor et al., 2000]. The correlation between SAGE II zonal-height SVC climatological figures and MLS relative humidity is striking except for the March–April–May (MAM) season, where MLS shows more equatorial symmetry than SAGE II cloud percentages [see Wang et al., 1996, Figure 3]. The zonal average Vaisala humidities at 147 hPa in the tropics are approximately 80–90 %RHi, which is inconsistent with the dry bias at  $-60^{\circ}\text{C}$  observed by [Miloshe-

vich et al., 2001] in the raw Vaisala radiosonde data and implies that the archived data were processed differently with a nonlinear temperature correction.

A Vaisala radiosonde global seasonal UTH climatology was produced in a similar fashion to that of MLS (see Plates 10–13) for comparison. The Vaisala data, converted to %RHi were linearly interpolated onto the 4 MLS UTH levels and averaged in  $5^{\circ} \times 4^{\circ}$  longitude by latitude bins. Plates 15–18 show the differences between the Vaisala and MLS climatologies. The differences at 147 hPa show a zonal behavior with MLS having wetter tropics and drier mid–high latitudes. But there are some notable exceptions, such as North America, which is 50% wetter, and South Africa, which is sometimes 30% drier. The latter is believed to be caused by a reporting practice where all the radiosonde values at 147 hPa are set to 0 %RHi. A latitude-dependent pattern in the differences exists at 215 hPa. The radiosondes are generally drier than MLS in the tropics but generally wetter in the Northern Hemisphere higher latitudes. The southern middle latitudes show the best agreement. The difference at 316 hPa is larger. More areas of the globe, including the tropics, show a dry bias in the MLS data but, interestingly, MLS is much wetter over the northeast Atlantic region in all seasons. The southern midlatitudes are generally in best ( $\sim 10$ – $20$  %RHi) agreement with MLS. The 464 hPa climatologies agree within  $\pm 20$  %RHi except over North America during fall and winter where the sondes are 40–50 %RHi wetter than MLS. Peixoto and Oort [1996] have a full global radiosonde humidity climatology for the 500 hPa level. Comparing this to the MLS 464 hPa shows overall qualitative and approximate quantitative agreement; however, the MLS 464 hPa data exhibit greater humidity extremes (drier and wetter) and have more spatial structure.

### 5.3. Comparison With SAGE II UTH Climatology

The Stratospheric Aerosol and Gas Experiment II (SAGE II) is a satellite-based remote sensing instrument designed to measure humidity in the stratosphere and troposphere using solar occultation [Rind et al., 1993]. SAGE II has been in operation since October 24, 1984. Tropospheric water vapor data are available from that time until mid 1991 when the Pinatubo eruption occurred. Aerosol loading from Pinatubo prevented SAGE II tropospheric humidity measurements from June 1991 until 1995. Tropospheric water vapor data from SAGE II have recently become available for the post-Pinatubo period. We have not yet been able to perform near coincident comparisons between MLS and SAGE II but have compared their UTH climatologies.

Plate 19 shows a seasonal comparison between SAGE II [Chiou et al., 1997] and MLS zonal mean UTH climatologies. The SAGE II values are binned in 20 degree latitude

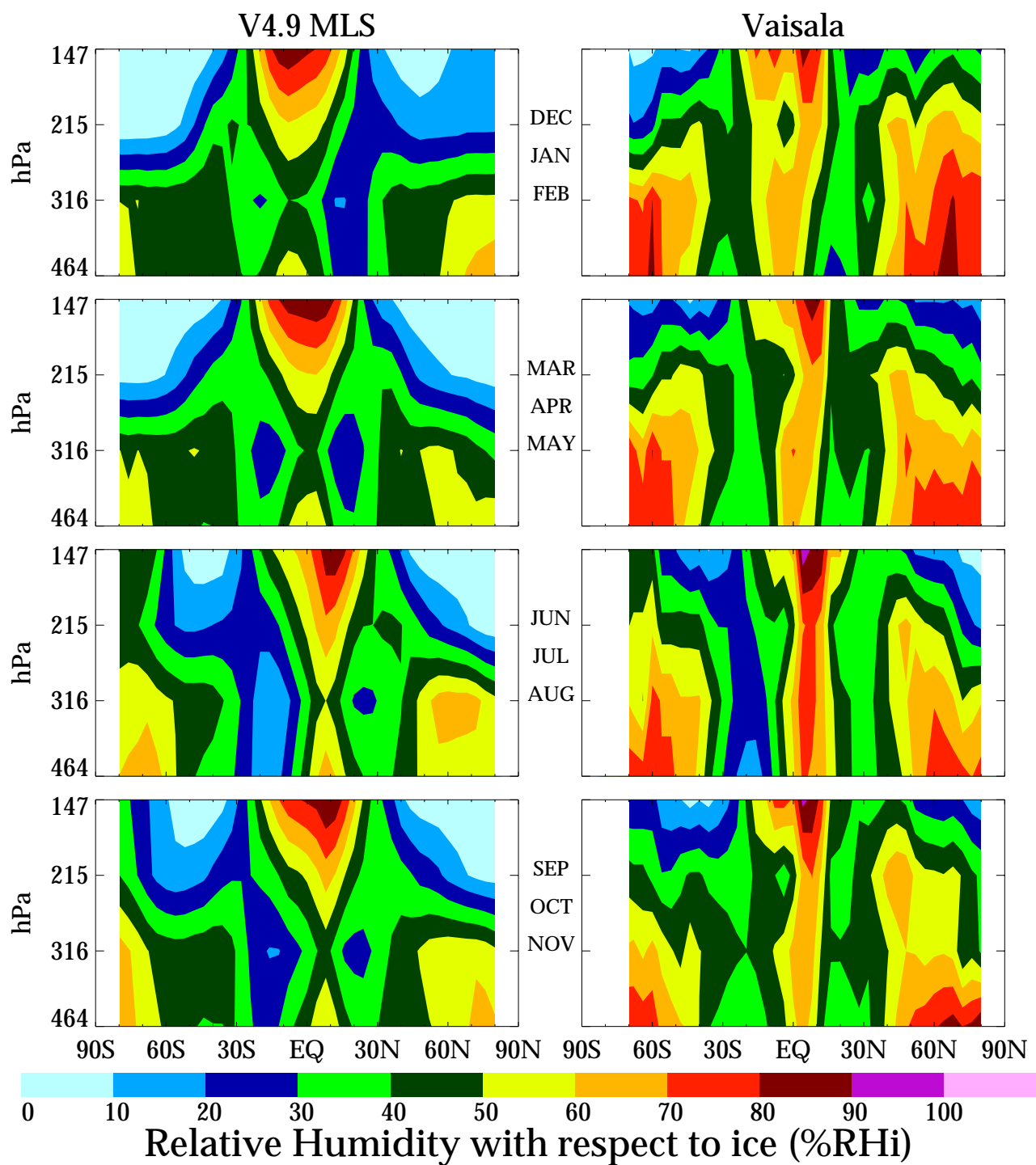


**Plate 14.** V4.9 MLS and Vaisala radiosonde zonal average UTH climatologies for the first 5½ years (September 1991 through June 1997) of the UARS mission.

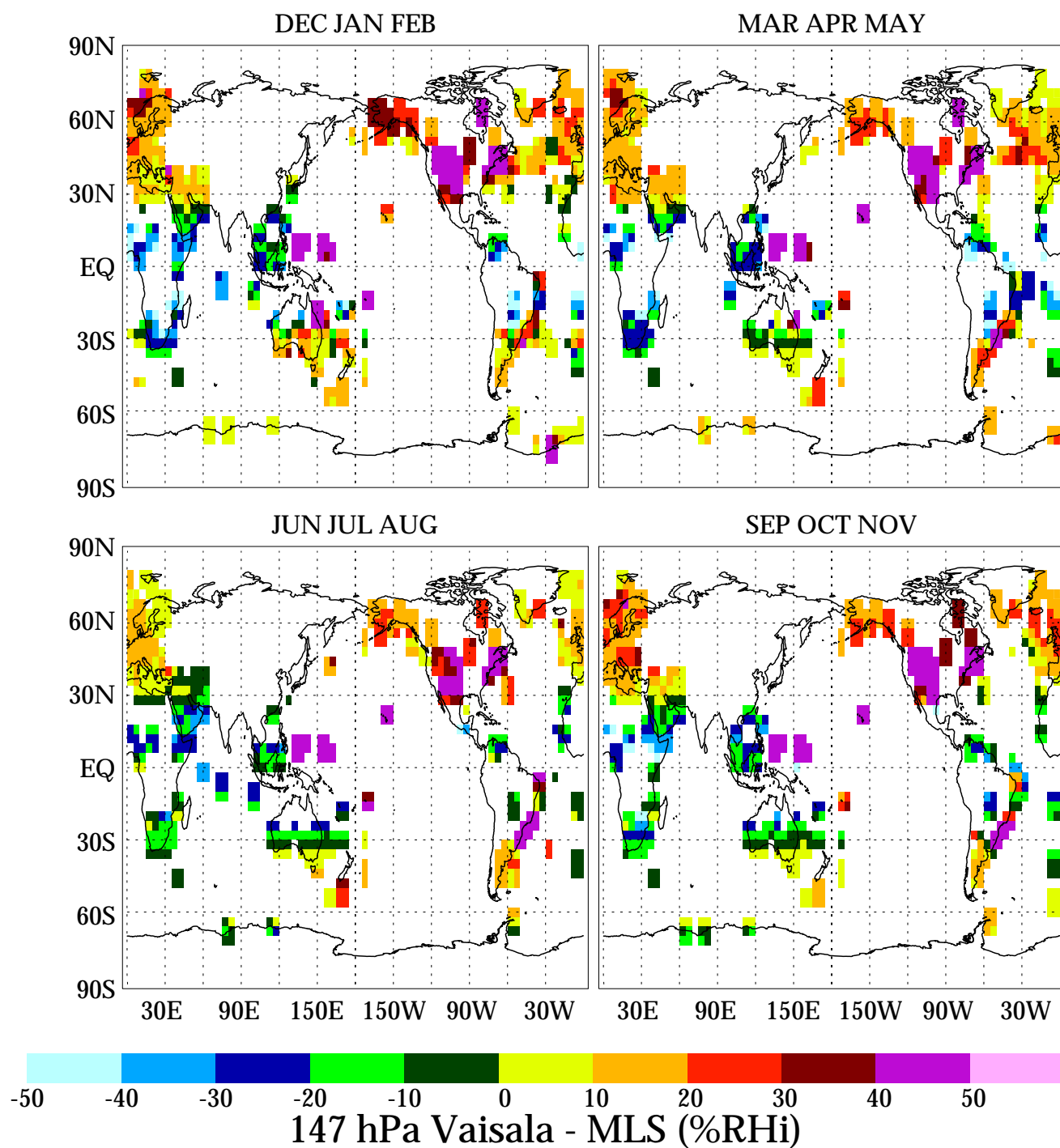


**Plate 15.** Vaisala radiosonde minus V4.9 MLS seasonal climatologies at 147 hPa for September 1991 through June 1997. Locations where there are no Vaisala radiosonde stations are blank.

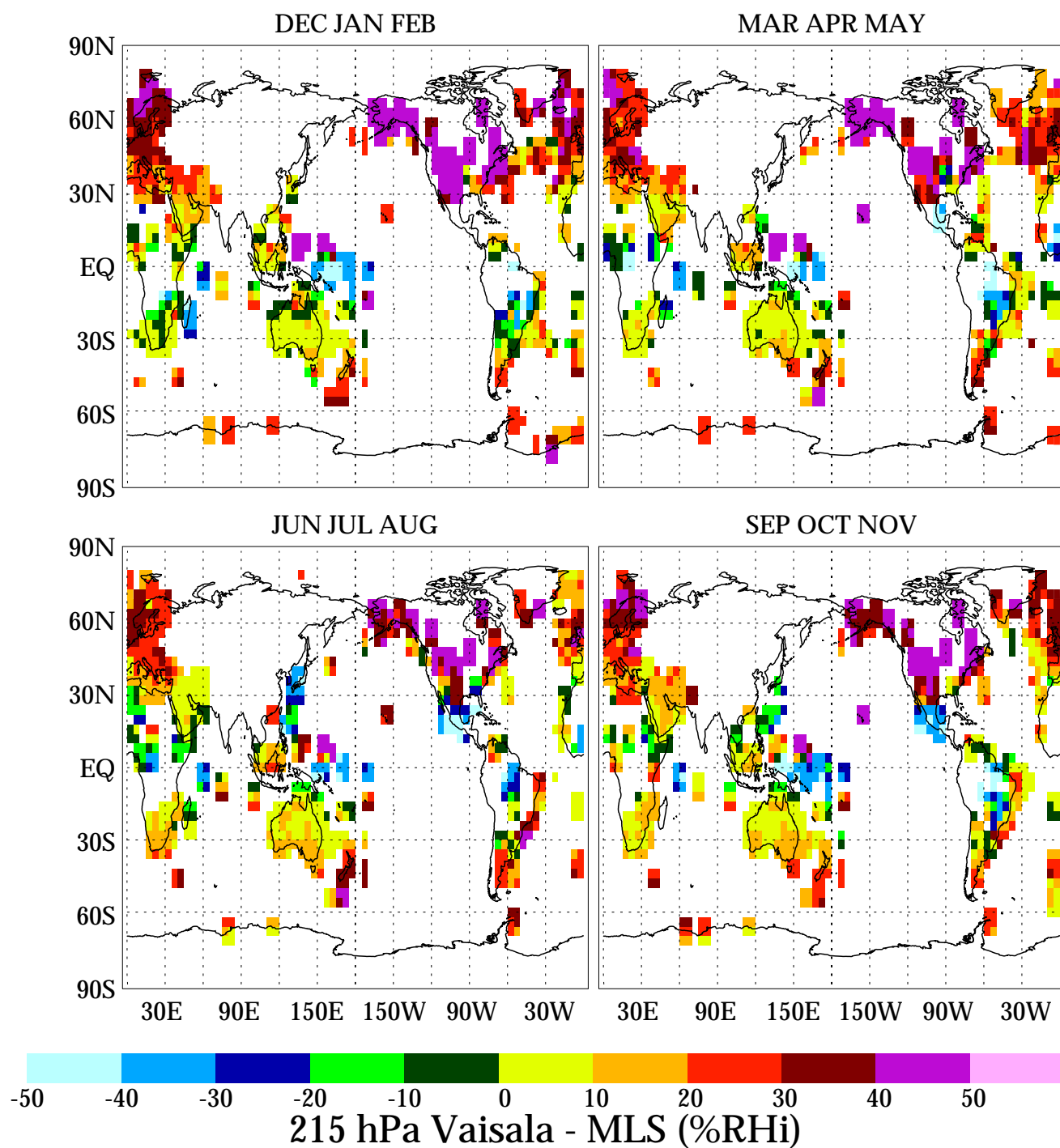
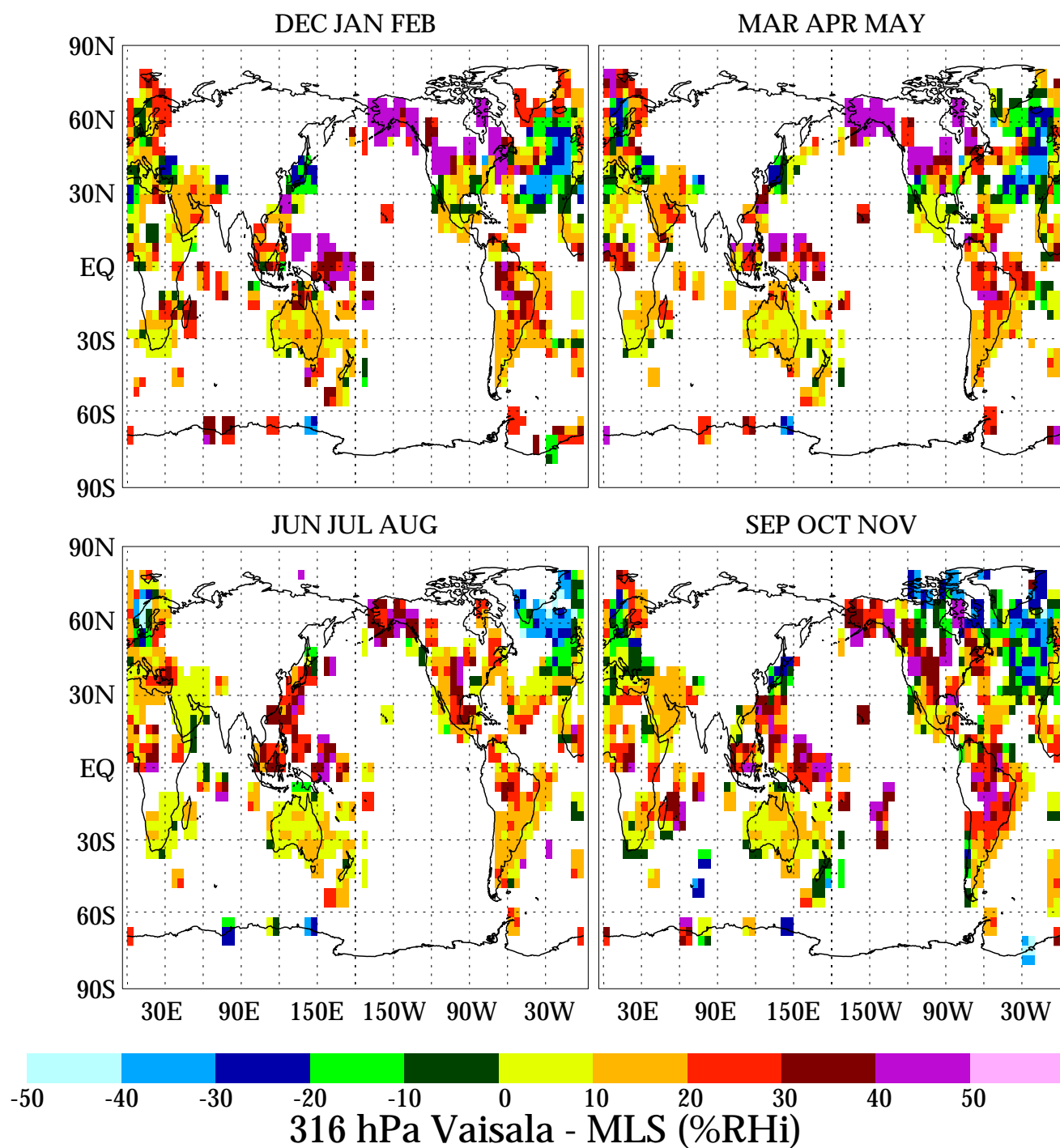


Plate 16. Same as Plate 15, but for 215 hPa.

**Plate 17.** Same as Plate 15, but for 316 hPa.

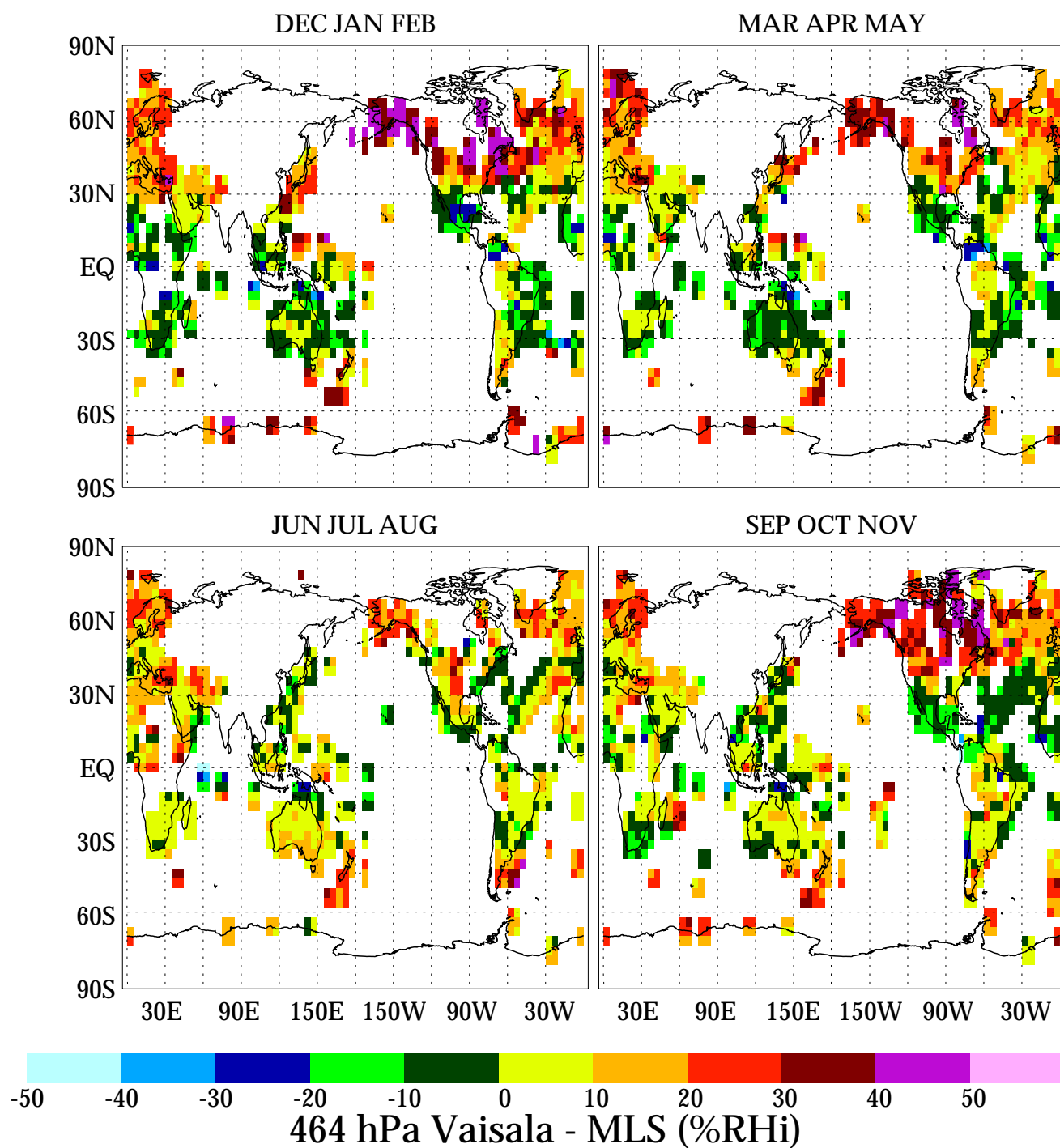
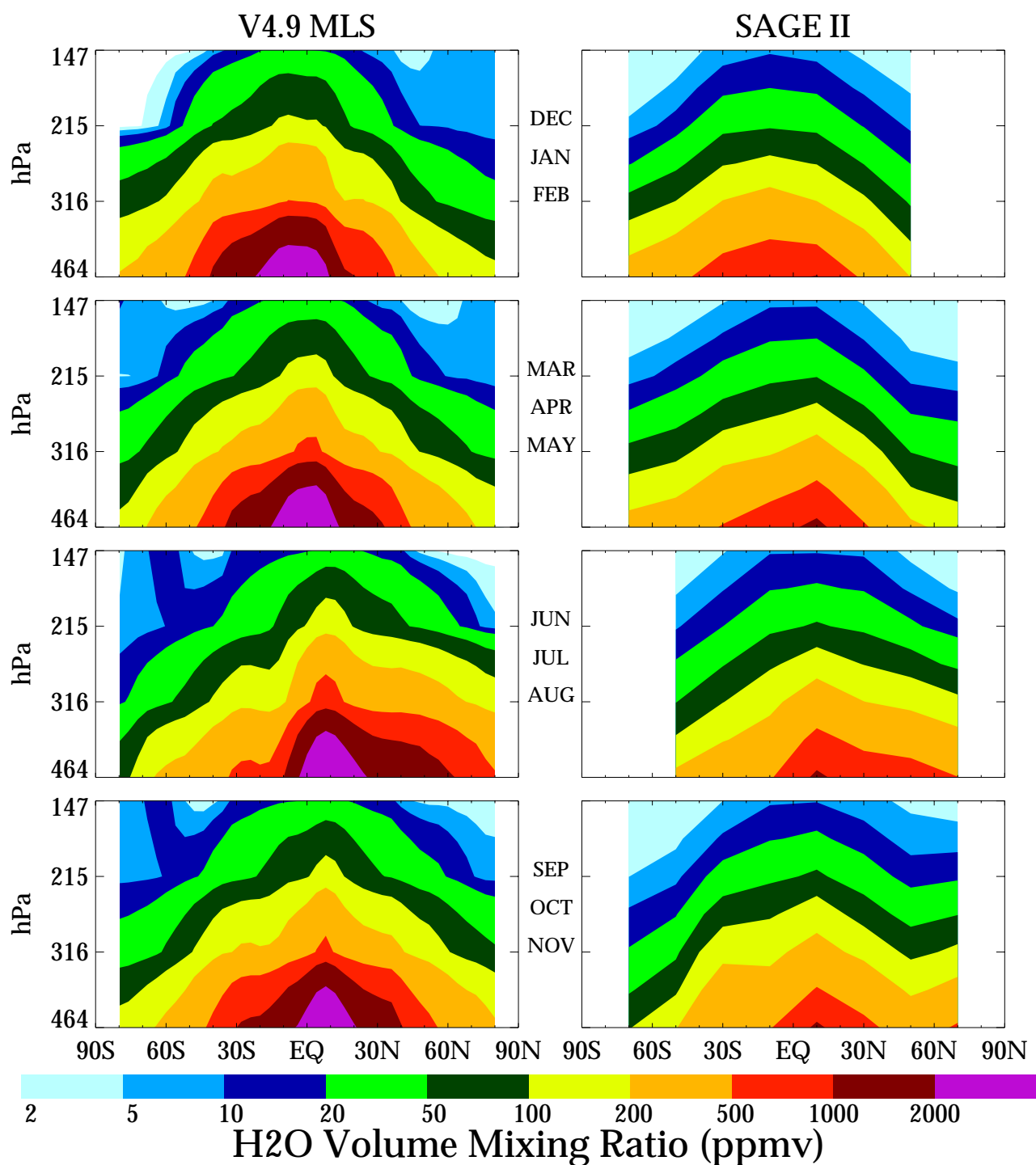


Plate 18. Same as Plate 15, but for 464 hPa.





**Plate 19.** H<sub>2</sub>O zonal climatologies from MLS (V4.9) and SAGE II [Chiou *et al.*, 1997]. The MLS data are from September 1991 through June 1997, and SAGE II data are from January 1986 through May 1991.



**Table 4.** Zonally Averaged MLS Water Vapor Mixing Ratio and Relative Humidity With Respect to Ice (%RHi) December—February<sup>a</sup>

Altitude, km	Latitude Bin							
	80°S–60°S	60°S–40°S	40°S–20°S	20°S–EQ	EQ–20°N	20°N–40°N	40°N–60°N	60°N–80°N
6.5	166.0(48)	512.1(43)	1504.2(39)	2375.4(42)	1418.5(27)	655.4(33)	224.7(44)	92.4(59)
7.5	99.0(48)	288.2(44)	773.1(36)	1250.2(38)	730.8(24)	333.6(32)	114.4(43)	47.3(54)
8.5	57.2(44)	170.2(45)	410.3(33)	674.0(34)	392.4(22)	179.4(30)	60.4(41)	23.2(46)
9.5	11.0(26)	89.9(38)	218.7(32)	295.4(27)	224.4(22)	112.1(31)	30.4(34)	11.0(32)
10.5	3.4(7)	42.4(26)	117.8(36)	172.9(39)	129.7(31)	53.4(28)	13.3(21)	5.9(18)
11.5	1.3(1)	20.5(17)	72.7(40)	119.4(52)	88.8(40)	29.4(24)	5.8(14)	4.4(17)
12.5	0.8(1)	5.0(11)	36.8(39)	75.2(66)	54.4(51)	12.8(21)	3.0(10)	5.4(17)
13.5	1.2(1)	2.6(6)	18.7(35)	37.3(83)	27.7(64)	7.5(18)	2.7(7)	5.0(17)

<sup>a</sup>Water vapor mixing ratio in ppmv and relative humidity with respect to ice %RHi in parentheses.**Table 5.** Zonally Averaged MLS Water Vapor Mixing Ratio and Relative Humidity With Respect to Ice (%RHi) March—May<sup>a</sup>

Altitude, km	Latitude Bin							
	80°S–60°S	60°S–40°S	40°S–20°S	20°S–EQ	EQ–20°N	20°N–40°N	40°N–60°N	60°N–80°N
6.5	119.2(50)	393.5(42)	1203.1(38)	2166.5(37)	2061.0(37)	1042.2(39)	397.5(48)	169.2(51)
7.5	68.9(48)	217.7(43)	622.9(36)	1129.2(34)	1072.5(33)	524.1(37)	203.8(47)	87.8(46)
8.5	31.7(42)	123.9(44)	332.6(35)	604.7(30)	576.2(30)	273.8(35)	108.6(46)	45.2(40)
9.5	10.4(25)	71.3(39)	189.9(34)	282.6(25)	271.8(24)	158.8(34)	53.4(39)	13.3(28)
10.5	4.9(8)	35.1(28)	99.8(35)	163.9(36)	159.5(35)	82.6(35)	22.8(26)	4.8(13)
11.5	2.3(6)	16.1(21)	59.5(37)	112.3(47)	110.3(46)	48.8(37)	9.9(16)	2.3(7)
12.5	2.5(5)	4.6(13)	30.0(35)	71.7(61)	69.8(59)	21.2(31)	2.9(10)	1.8(5)
13.5	1.5(2)	2.7(7)	16.4(31)	36.6(77)	35.3(75)	10.5(24)	1.8(5)	0.9(1)

<sup>a</sup>Water vapor mixing ratio in ppmv and relative humidity with respect to ice %RHi in parentheses.**Table 6.** Zonally Averaged MLS Water Vapor Mixing Ratio and Relative Humidity With Respect to Ice (%RHi) June—August<sup>a</sup>

Altitude, km	Latitude Bin							
	80°S–60°S	60°S–40°S	40°S–20°S	20°S–EQ	EQ–20°N	20°N–40°N	40°N–60°N	60°N–80°N
6.5	90.9(61)	228.6(44)	534.2(26)	871.2(16)	3346.8(57)	1671.1(30)	1278.0(52)	608.5(53)
7.5	44.6(56)	118.7(43)	281.5(25)	451.5(14)	1783.3(52)	838.1(27)	677.4(53)	328.9(54)
8.5	19.3(49)	62.5(43)	157.0(25)	246.2(13)	972.8(46)	453.5(24)	372.3(53)	188.1(55)
9.5	10.5(44)	32.9(36)	106.8(28)	176.2(17)	339.9(28)	253.7(24)	187.4(47)	71.2(46)
10.5	6.5(41)	16.0(24)	52.8(25)	105.0(25)	201.3(42)	142.3(31)	85.1(38)	24.2(25)
11.5	5.7(45)	7.4(18)	30.1(22)	74.6(33)	138.8(55)	94.0(39)	44.6(29)	9.6(8)
12.5	7.7(46)	4.4(14)	14.3(20)	46.9(41)	86.9(68)	55.3(42)	13.4(21)	2.0(5)
13.5	6.1(20)	2.7(6)	9.2(18)	24.7(50)	42.3(81)	27.8(43)	5.1(10)	0.9(2)

<sup>a</sup>Water vapor mixing ratio in ppmv and relative humidity with respect to ice %RHi in parentheses.

**Table 7.** Zonally Averaged MLS Water Vapor Mixing Ratio and Relative Humidity With Respect to Ice (%RH<sub>i</sub>) September–November<sup>a</sup>

Altitude, km	Latitude Bin							
	80°S–60°S	60°S–40°S	40°S–20°S	20°S–EQ	EQ–20°N	20°N–40°N	40°N–60°N	60°N–80°N
6.5	96.4(59)	306.7(42)	906.4(36)	1256.8(23)	2651.6(48)	1383.5(37)	598.8(49)	233.9(59)
7.5	50.6(56)	165.1(42)	474.2(35)	644.2(21)	1388.5(43)	700.4(34)	315.7(49)	125.4(56)
8.5	23.6(51)	92.1(42)	257.6(34)	342.9(18)	744.3(38)	368.0(31)	172.0(49)	65.2(53)
9.5	10.0(41)	44.6(35)	151.1(33)	210.9(20)	291.6(27)	201.9(29)	99.8(43)	26.0(36)
10.5	5.5(32)	20.3(23)	75.8(31)	124.1(30)	172.3(40)	106.7(33)	47.4(33)	11.3(17)
11.5	3.8(31)	8.7(15)	43.2(29)	86.3(39)	119.7(53)	65.1(36)	23.6(25)	4.3(8)
12.5	3.4(20)	3.1(10)	20.9(26)	55.1(51)	74.8(67)	35.5(37)	7.7(17)	1.9(5)
13.5	1.1(1)	2.0(4)	12.2(23)	29.2(66)	36.7(82)	18.9(37)	4.1(9)	1.9(3)

<sup>a</sup>Water vapor mixing ratio in ppmv and relative humidity with respect to ice %RH<sub>i</sub> in parentheses.

bins [Chiou *et al.*, 1997, Tables 1a–1d]. The SAGE II data, which are on a 1 km vertical grid, were converted to pressure using NCEP geopotential analyses fields. The SAGE II period covers January 1996 through May 1991 and MLS covers September 1991 through June 1997. The interannual sampling for the MLS average is not homogeneous, with the first 3 years being much more heavily sampled than after 1994 due to degraded satellite power capability and MLS antenna scanning problems. SAGE II averages contain between 50 and 2500 observations per season–latitude bin. The number is affected by the frequency of clouds. The MLS bins contain 20,000–70,000 profiles per season–latitude bin, screened according to the recommendations in section 4. Tables 4–7 give MLS UTH values in the SAGE II format used by Chiou *et al.* [1997]. MLS pressure was converted to height using hydrostatic balance with NCEP geopotential height at a reference surface as a boundary condition.

The MLS and SAGE II patterns agree fairly well qualitatively with both experiments showing the expected seasonal solar tracking of peak humidity about the equator. An interesting exception is the MAM season where MLS is nearly symmetrically distributed about the equator, whereas the SAGE II 0–20°N bin and the 0–20°S bin show very different numbers. Quantitatively, the agreement is best in the extreme polar bins (60°–80°N and S). MLS is much wetter in the tropics. The MLS detection threshold is approximately 8 ppmv at 147 hPa, which is higher than typical stratospheric values of 3–5 ppmv. The typical high-latitude profile above 6.5 km is very dry (< 500 ppmv) and cloud free, which allows many measurements by MLS and SAGE II. The good agreement in these regions is satisfying. The large difference in tropical UTH values is to be expected. A cloud climatology based on SAGE II observations [Wang *et al.*, 1996] shows very high frequencies of SVC occurring throughout the tropics. Cirrus frequencies greater than 60% at 15.5 km

around the regions normally associated with tropical convection is typical, and SAGE II does not get a vapor measurement under these conditions. Thin cirrus has negligible impact on the MLS humidity measurement and its sampling is not affected by them. The atmosphere surrounding cirrus is expected to be 100 %RH<sub>i</sub> which explains the high frequency of MLS tropical measurements at 147 hPa being near 100 %RH<sub>i</sub> as shown in Plate 14. Jensen *et al.* [1999] and Sandor *et al.* [2000] further discuss the high values of MLS %RH<sub>i</sub> and cirrus in the tropical upper troposphere.

The Peixoto and Oort [1996] radiosonde climatology is also wetter than the SAGE II climatology but not in the same way as MLS. The Peixoto radiosonde climatology tends to be significantly wetter than SAGE II in high latitude and equatorial regions but in better agreement at midlatitude. MLS, on the other hand, is considerably wetter than SAGE II in the equatorial region but is in good agreement with SAGE II at high latitude.

#### 5.4. Summary of Climatological Comparisons

Establishing the climatological behavior of water vapor is necessary for understanding global climate. The high variability of water vapor, clouds, and questionable humidity sensor accuracy are significant obstacles for accurately determining the global humidity climatology. The climatological comparisons shown here underscore this. Qualitatively, the MLS climatologies agree with the radiosondes and SAGE II, but quantitatively, there are some significant differences. The differences are very heterogeneous and not easily understood as a “bias” difference. The V4.9 MLS zonal climatology is wetter than SAGE II in the tropics by at least a factor of 2, but is in better agreement at high latitudes. This difference is almost certainly caused by sampling differences between the instruments and suggests that

SAGE II sampling is not sufficient to determine an accurate global climatology. Interpretation of V4.9 MLS climatological differences with the Vaisala radiosonde climatology is complex. On average, MLS appears drier than the radiosonde, but there are some notable exceptions. These include some regions in the tropics at 215 and 147 hPa and the northeast Atlantic at 316 hPa. This argues against a simple “bias” difference between these instruments. Also it is not clear that sampling behavior can explain this difference. There is no evidence based on the Vaisala radiosonde zonal climatology produced from the archived data that its humidities are too dry by a factor of 2 as would be expected from direct comparisons of raw data from the Vaisala RS80-A instrument and the frostpoint hygrometer [Miloshevich *et al.*, 2001]. In the next section we explore the differences that exist between MLS and other sensors by looking at coincident comparisons.

## 6. Coincident Comparisons of V4.9 MLS UTH With Other Techniques

### 6.1. Methods and Definition of Coincidence

This section compares “coincident” upper tropospheric humidity measurements between MLS and other techniques. Unless specified otherwise, we are using V4.9 MLS UTH for the comparisons. The goal is to compare MLS with an accurate sensor that measures vertical profiles and has enough data to produce hundreds of coincidences in order to determine statistically significant biases. Unfortunately, no existing technique during the MLS prime measurement period (1992–1994) fully satisfies the criterion. Three techniques are considered for the coincident comparisons. The frostpoint hygrometer (FPH) is used because its accuracy is well established [Oltmans, 1985]. Unfortunately, there are relatively few FPH profiles available. The Vaisala radiosonde was chosen because it produces vertical profiles up to 150 hPa, frequently flown by the radiosonde network, and may have good accuracy in the upper troposphere (based on SAGE II validation [Larsen *et al.*, 1993]). However, the quality of the Vaisala humidities depend on the data processing because the raw data are systematically biased at low temperatures, being dry by a factor of 2 at  $-60^{\circ}\text{C}$  [Miloshevich *et al.*, 2001]. The third technique, Measurement of Ozone and Water Vapor by Airbus In-Service Aircraft (MOZAIC), measures UTH using a Vaisala thin-film capacitive hygrometer with the superior H-type sensor mounted on commercial Airbus aircraft. The MOZAIC hygrometer is routinely recalibrated insuring its accuracy. MOZAIC produces much good vertically registered humidity data for comparison. SAGE II was not used because there are no suitable coincidences, as discussed in section 5. Humidity data

from nadir sounding operational satellites were not used because their vertical resolution and registration are poor and the data require nadir-sounding analysis.

The high variability of tropospheric water vapor makes coincidence comparisons difficult. The MLS measures water vapor in an approximate volume  $100 \times 200 \times 10 \text{ km}^3$  (across track  $\times$  along track  $\times$  vertical). The MLS forward model accounts for vertical gradients as described by four levels (464, 316, 215, and 147 hPa); it assumes horizontal homogeneity within the volume. Horizontal heterogeneity will cause some errors in the retrieved MLS humidity. The techniques used here for validation measure water vapor in situ in a substantially smaller volume than MLS. A large number of “coincidences” between the in situ and MLS should allow determination of measurement biases between the techniques; however, some care is required to interpret the results.

The method for establishing biases between MLS and other data sets is to find coincidence matches and fit a line to a scatterplot of the data. A linear fit to the scattered data gives bias (intercept) and scaling (slope) values. The considerable scatter between the coincidentally measured humidities by MLS and in situ methods indicates that a significant component of these measurements is either not correlated with atmospheric humidity or what is measured as atmospheric humidity. For example, instrument noise is not correlated with atmospheric humidity and the average humidity within a relatively large volume is not necessarily the same humidity as that observed at any point in the volume. Therefore there is uncertainty regarding the most appropriate method for determining the best linear relationship between the data sets. The linear regression (LR) method [Bevington, 1969] is useful for the case where in situ methods are assumed to be noise and error free and provides an indication of the actual bias and scaling in the MLS UTH. Apart from the volume averaging issue, the accuracies claimed by the in situ techniques are much better than that of MLS, and therefore an LR fit line would accurately determine the bias and scaling relationships if MLS UTH measurement is used as a proxy for an in situ measurement. However, due to uncertainties associated with comparing an in situ measurement with a volume average, the LR approach will tend to overestimate/underestimate the actual bias/scaling relationship between the measurements from the perspective of the true volume averaged UTH. The most appropriate approach is to use a method which independently assigns a noise to both MLS and in situ methods. The noise on the in situ technique would be the standard deviation of the in situ humidities inside the MLS measurement volume. Unfortunately, this is not known. MOZAIC which makes measurements along a horizontal track typically observe variability comparable to

MLS UTH accuracies. Therefore we perform an orthogonal distance regression (ODR) which produces the correct relationship when both measurements have equal noise.

The correlation coefficient, the ratio of the covariance to the square root of the product of the variances, determines how well the instruments track each other. The correlation coefficient between MLS and an in situ method is degraded by (1) instrument noise, (2) comparing a volume-averaged humidity with a point measurement, (3) lack of coincidence (i.e., different time and location), and (4) forward model errors that are uncorrelated with humidity. The computed correlation coefficient between MLS and another technique can be compared with what we expect to determine if the comparison is reasonable. Comparing MLS UTH with itself randomized with instrument noise (effect 1) gives correlations of 0.9, 0.9, 0.9, and 0.6 for 147, 215, 316, and 464 hPa levels, respectively. The MLS data can be used to estimate a volume smoothed UTH decorrelation due to lack of coincidence (effects 1 and 3). MLS measures a profile every 4° (450 km) of orbit arc per minute. The correlation of adjacent measurements is 0.85, 0.62, 0.47, and 0.43 for 147, 215, 316, and 464 hPa, respectively. The decorrelation of a volume average compared to a point measurement may be significant (effect 2). The MOZAIC data set show humidity measurements along a level flight path having 20–30 %RHi variability about the mean over a 110 km distance near 215 hPa. Using the MOZAIC measurement variability as representative of that in the atmosphere and 10 %RHi MLS precision at 215 hPa (effects 1 and 2) gives an estimated MLS correlation between 0.74 and 0.50. Therefore the correlation between in situ and MLS volume-averaged measurements may be low (see *Sassi et al.* [2001] for a discussion of the atmospheric implications of these correlations). MLS forward model errors that would lead to decorrelation are expected to be caused by its inability to accurately partition the radiance signal into contributions from dry, humid, contaminating species and instrumental components. An example of the latter is the yaw cycle artifact at 147 hPa, discussed in section 4.

## 6.2. Frostpoint Hygrometer Data

The frostpoint hygrometer (FPH) instrument measures water vapor concentrations based on its condensation temperature and is considered accurate to 10% (in concentration) [*Oltmans*, 1985]. It measures water vapor in situ, is lifted through the atmosphere with a balloon, and samples every 250 m. The UARS CDHF maintains a correlative database which has data from Boulder, Colorado (40°N, 105°W); Hilo, Hawaii (19°N, 155°W); Lauder, New Zealand (45°S, 169°E); McMurdo, Antarctica (77°S, 166°E) and Central Equatorial Pacific Experiment (CEPEX; 2°N,

157°W). We were supplied additional FPH profiles from CEPEX (A. Dessler, personal communication, 1994) and Boulder for the analysis. The coincidence criterion of 5.0° longitude, 3.0° latitude, and 6.0 hours time is used for comparing MLS UTH with FPH. This criterion produces 16 independent FPH profiles for comparison with 31 independent MLS UTH profiles.

The CEPEX campaign took place in the central Pacific. Four MLS coincidences from this campaign are shown in Plate 20. An FPH was flown alongside a Vaisala H-type instrument whose profile is also shown in Plate 20. The FPH profile was degraded to the MLS resolution by convolving it with the triangular basis functions appropriate for the MLS retrievals. The MLS profiles are screened according to section 4. Retrieved humidities at levels in cirrus are assigned 100 %RHi, and retrieved values at 316 and 464 hPa which may be erroneously retrieved and are recommended for rejection are shown. The CX001 profile, with four MLS profiles coincident, is representative of a challenging measurement situation for MLS. The CX001 FPH profile has a data gap between between 200 hPa and 140 hPa where it measures 100 %RHi on the gap boundaries indicative of cirrus. All four coincident MLS profiles show humidities above 120 %RHi at 147 hPa and three of the four measure greater than 120 %RHi at 215 hPa indicating ice detection. One of the MLS UTH profiles measures ~1200 %RHi at 147 hPa, thick cirrus possibly having an average IWC of ~0.6 g m<sup>-3</sup> within the MLS measurement volume. The four CX001 coincident MLS 215 hPa humidity measurements agree with the FPH within error. The high absorption in the upper two levels compromise the ability to measure vapor at the lower two levels. The retrieval has a tendency to badly underestimate vapor at 316 and 464 hPa in this situation. The quality criterion would mark seven out of eight MLS values as bad at 316 and 464 hPa even though five of them are in reasonable agreement with the FPH measurements. This demonstrates that MLS can make useful measurements in the presence of thick cirrus and the quality screen successfully rejects cloud contaminated 316 and 464 hPa measurements.

Plate 21 shows three additional comparisons between V4.9 MLS UTH and the FPH profiles measured over Antarctica, New Zealand, and Hawaii. The Antarctic measurement is a test of the V4.9 MLS UTH when the atmosphere is very cold (< -70°C above 215 hPa). The FPH measures less than 10 ppmv, near the detection limit of MLS, at altitudes greater than 300 hPa. The small mixing ratios are why the MLS error bars for the upper two levels are quite large for this profile and hence show agreement with the FPH profile within the MLS uncertainty. The Hawaii FPH profile agrees with V4.9 MLS UTH within its uncertainty. The Lauder, New Zealand, FPH profile is significantly drier than MLS at 316 hPa but is

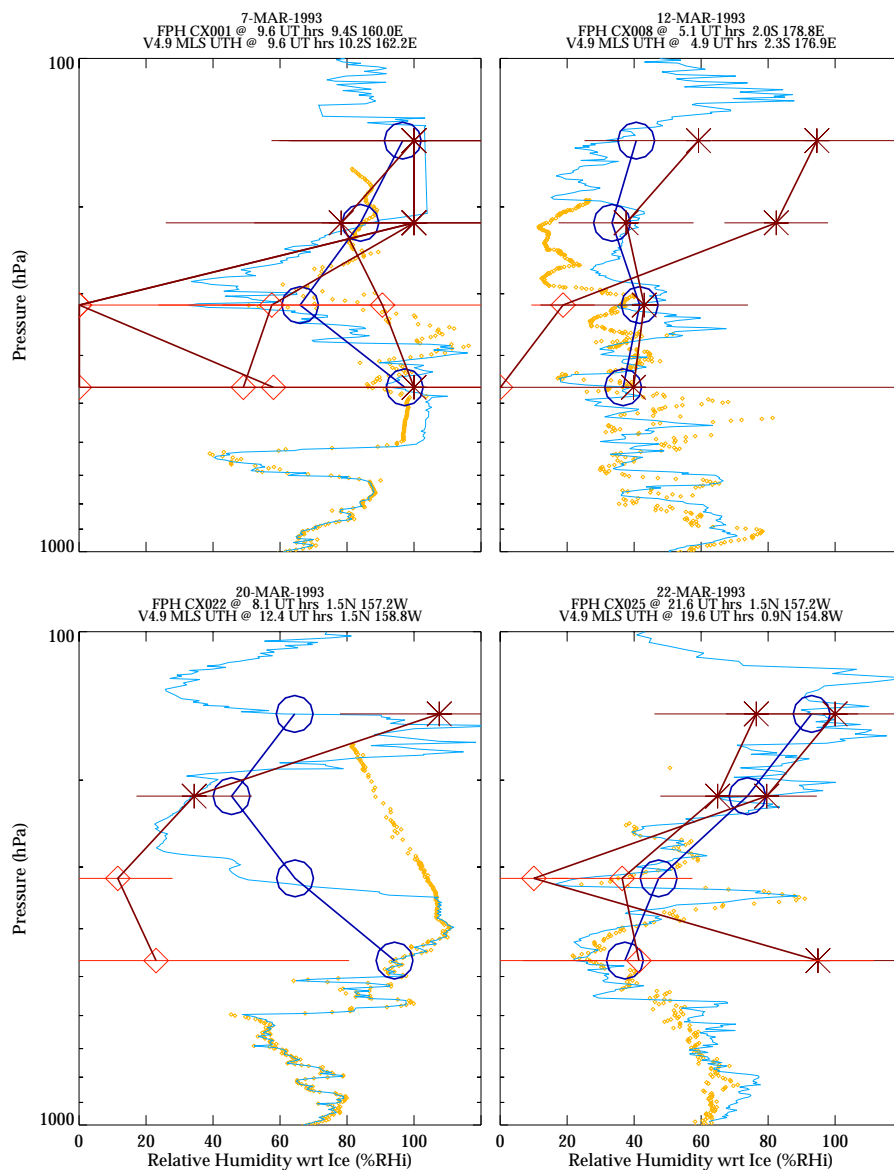


**Plate 20.** Profile comparison between V4.9 MLS (brown solid with error bars), Vaisala (tiny yellow diamonds), frostpoint hygrometer (thin blue line), and frostpoint hygrometer with vertical resolution degraded to that of MLS (large, dark blue circles and thick, dark blue line). Locations and times are given in the titles. The indicated MLS measurement location is the average for the profiles shown. The MLS measurements are marked with brown asterisks or red diamonds: diamonds are measurements that failed the quality check and are considered unreliable.

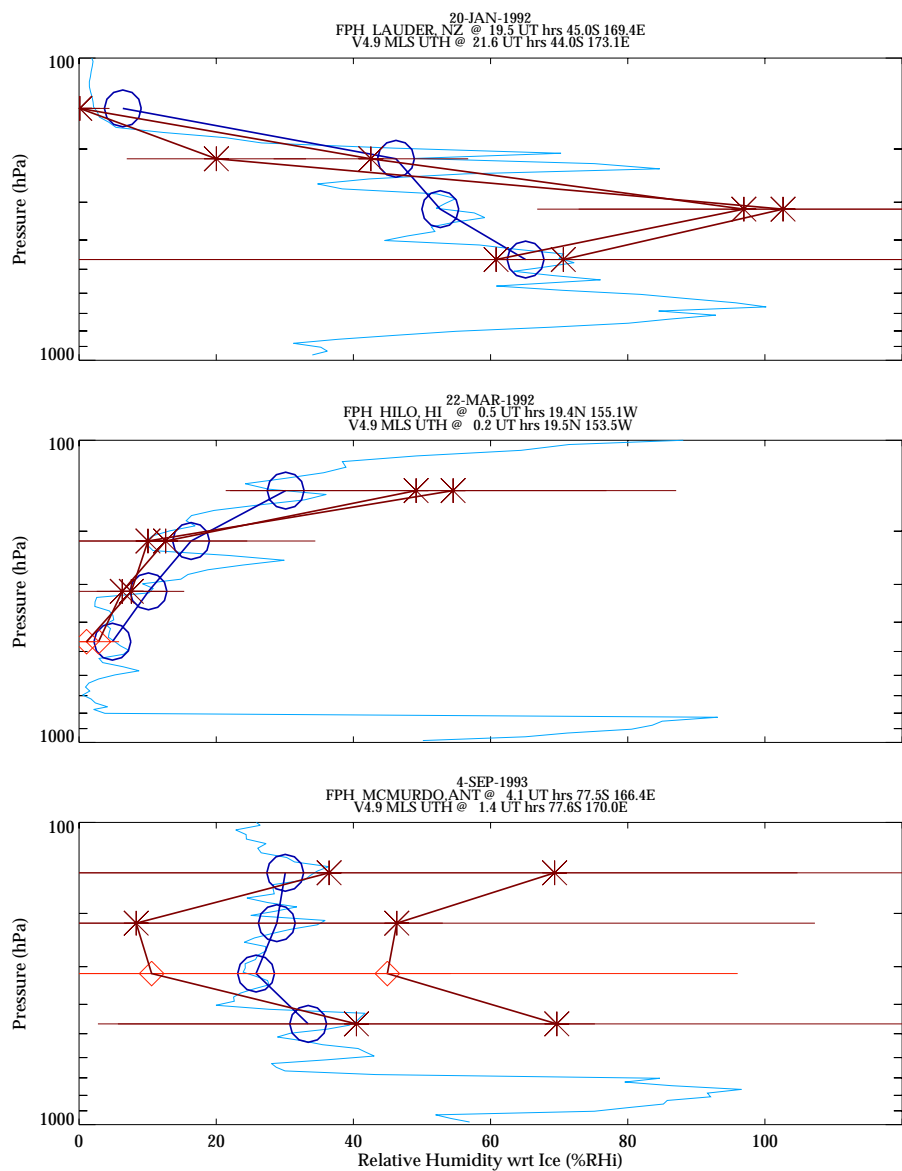


**Plate 21.** Same as Plate 20, but for FPH and MLS coincidences over New Zealand, Antarctica, and Hawaii.

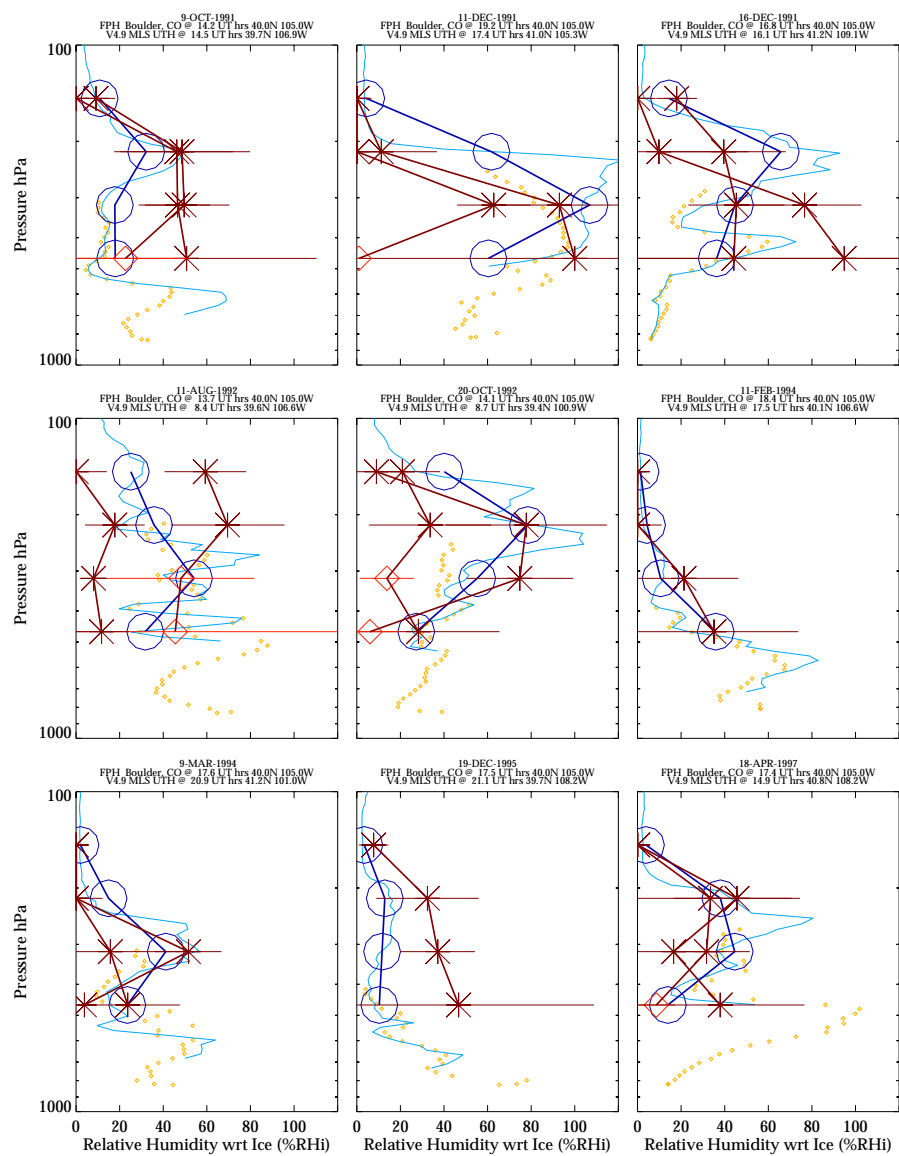


**Plate 22.** Same as Plate 20, but for FPH and MLS coincidences over Boulder, Colorado.

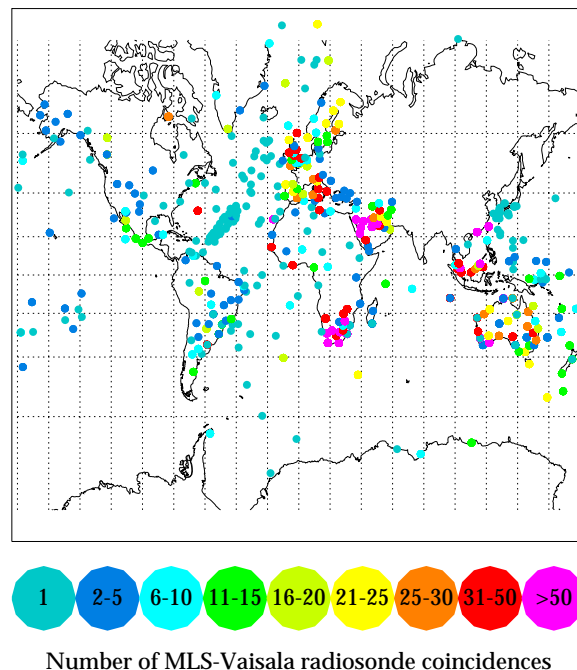
within the MLS uncertainties at the other levels. The majority of FPH data compared with MLS are for flights from Boulder, Colorado, as shown in Plate 22. These flights also included a Vaisala A-type humicap sensor. As with some of the other comparisons, there is a wide variation in agreement between MLS and the FPH, and large variability between adjacent MLS profiles, indicating substantial heterogeneity in the UTH field.

Figure 9 shows a scatterplot of V4.9 MLS UTH and the FPH with best fit lines through the points. MLS UTH measurements at 316 and 464 hPa that failed section 4 quality test were not included in their respective scatterplots. The 316 and 464 hPa quality screen recommended by section 4 significantly improves the overall correlation of the scatter (0.62 with screening versus 0.33 without it). The correlation between MLS UTH and FPH is somewhat better than that expected based on measured MLS UTH decorrelation between adjacent MLS measurements or that expected from comparing a volume averaged to an in situ humidity. Both methods of linear fitting between the FPH and V4.9 MLS humidities show agreement within 20 %RHi for all humidities less than 100 %RHi at all four levels which is comparable to the estimated systematic error. The degree of agreement between MLS UTH and FPH suggests that the V4.9 MLS UTH with the data screening recommended in section 4 is accurate within the expected capabilities of MLS, albeit this is based on a small number of coincidences.

### 6.3. Vaisala Radiosonde UTH Comparisons

**6.3.1. Comparisons with archived Vaisala radiosondes.** The Vaisala radiosonde network provides many coincidence opportunities with MLS. For this data set a coincidence is defined as within 1° latitude, 1° longitude (or  $\sim 110 \times 110 \text{ km}^2$ ), and 3 hours time. The coincidence is within the MLS measurement footprint and the correlation is limited mostly by instrument noise, volume averaging, and uncorrelated forward model errors; 4440 coincidences meet this criterion.

The geographical distribution and frequency of the coincident radiosondes are given in Plate 23. There is coverage over much of the globe except for most of the Asian continent which use the goldbeaters skin hygrometer eliminated from this study. The results of the coincidence comparisons are shown in two formats. The first format, shown in Plate 24, is a scatterplot including all V4.9 MLS UTH scattered against the coincident sonde measurement interpolated onto the 4 MLS retrieval heights. Since the NCEP mandatory levels are of comparable resolution to the MLS retrieval surfaces, linear interpolation in %RHi was considered adequate for the comparison. The MLS data are screened according to section 4. Comparing Plate 24 to the analogous

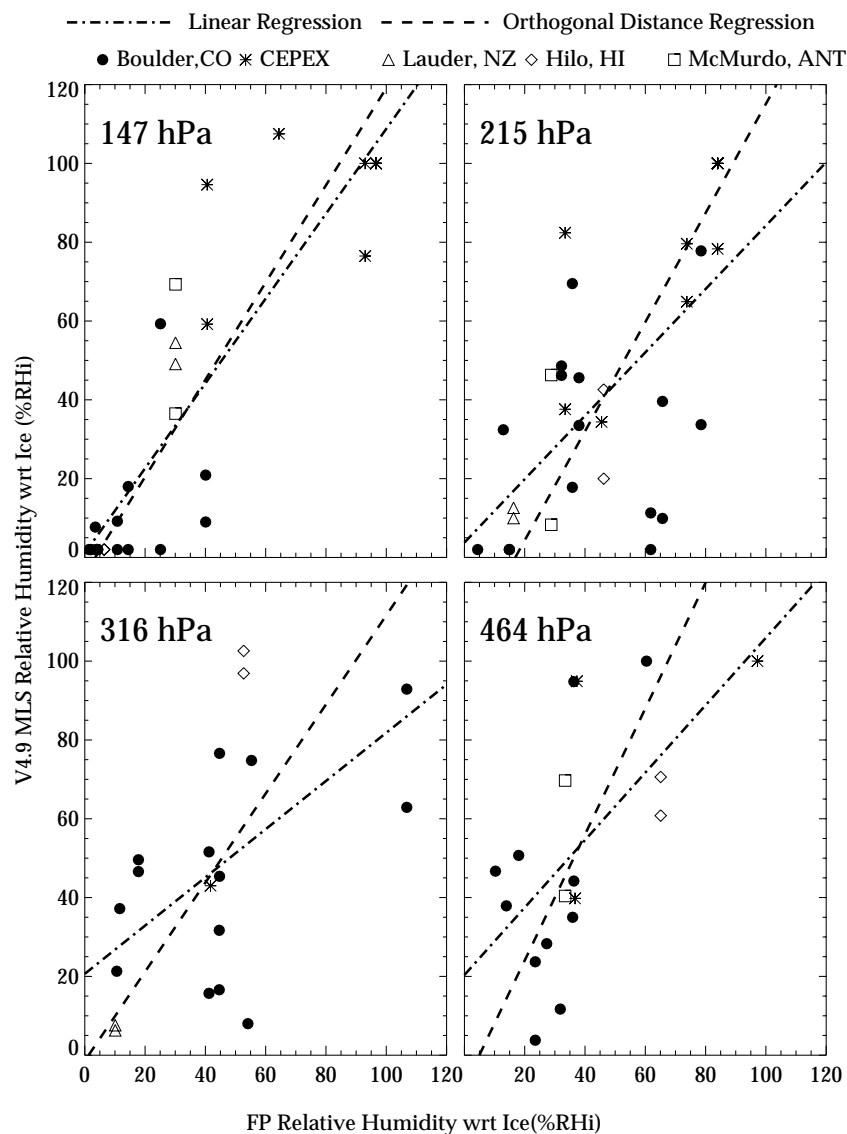


**Plate 23.** The distribution and number (color coded) of MLS-Vaisala radiosonde coincidences.

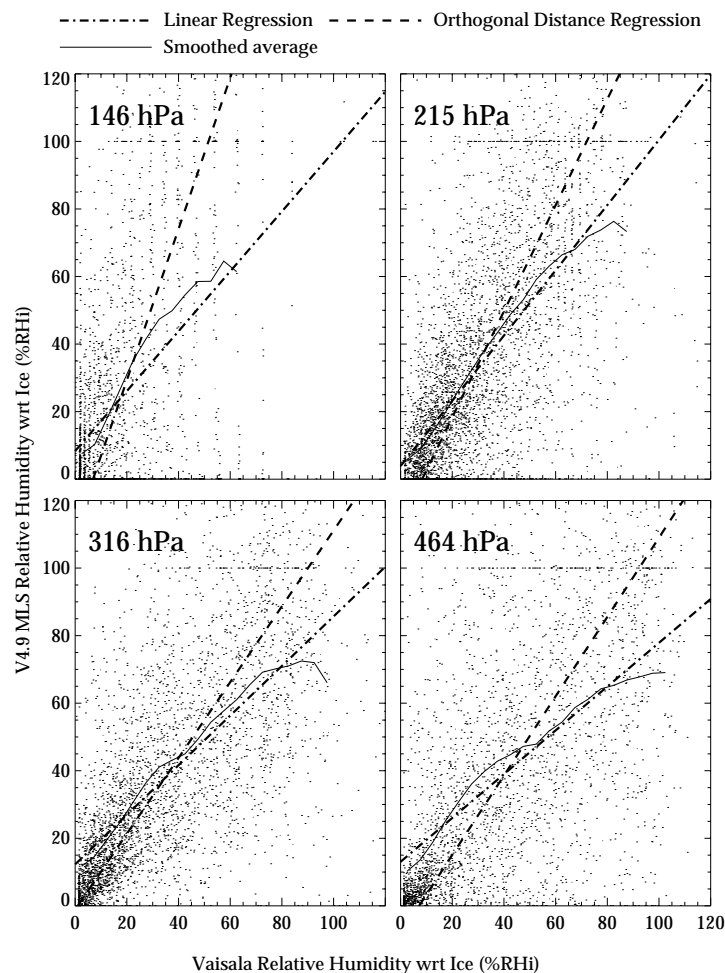
SAGE II plot [Larsen *et al.*, 1993, Figure 15, hygrometer-14] shows that MLS and SAGE II correlate similarly with the Vaisala radiosondes. Both show generally good correlation with considerable variability about the mean and MLS having more scatter than SAGE II. Given that SAGE II coincidence criterion ( $250 \times 250 \text{ km}^2$  by 6 hours) is larger than that for MLS, the cause of the scatter is probably not a coincidence problem. The most likely source of the scatter is comparing a volume smoothed to an in situ humidity with additional scatter in the MLS UTH plot due to MLS UTH measurement precision being 3 times noisier than SAGE II.

Figure 10 shows scatterplots of coincident Vaisala and V4.9 MLS measurements for the 147, 215, 316, and 464 hPa surfaces. Quality control and adjustments described in section 4 were applied to the MLS data. The 150 hPa Vaisala radiosonde data in the vicinity of South Africa were not included in the 147 hPa scatterplots because the dewpoint depression for these data appeared to be unphysically large (i.e., 0 %RHi). Overlaid on these plots are best fit lines from LR and ODR methods. A smoothed line is overlaid on the plot to demonstrate that the average MLS UTH is roughly linear with the Vaisala UTH. Therefore characterizing the comparison between MLS and Vaisala UTH in terms of bias and scaling factors is reasonable.





**Figure 9.** Scatterplot of all the V4.9 MLS UTH and frostpoint hygrometer coincidences. Lines from linear regression and orthogonal distance regression are overlaid on each panel. Printed with permission from *Kley et al.* [2000].



**Figure 10.** Scatterplots between coincident Vaisala radiosonde and V4.9 MLS UTH on the four MLS retrieval surfaces. Best fit lines and a smoothed average are overlaid. The smoothed average was computed by setting up a grid of 24 points separated by 5 %RH<sub>i</sub>. For each grid point the coincident MLS UTH is weighted by  $\cos^2(\pi(\text{sonde}\%RH_i - \text{gridpoint}\%RH_i)/20)$  and averaged. The  $\cos^2$  function is zero if  $|\text{sonde}\%RH_i - \text{gridpoint}\%RH_i| > 10\%RH_i$ . Printed with permission from Kley *et al.* [2000].

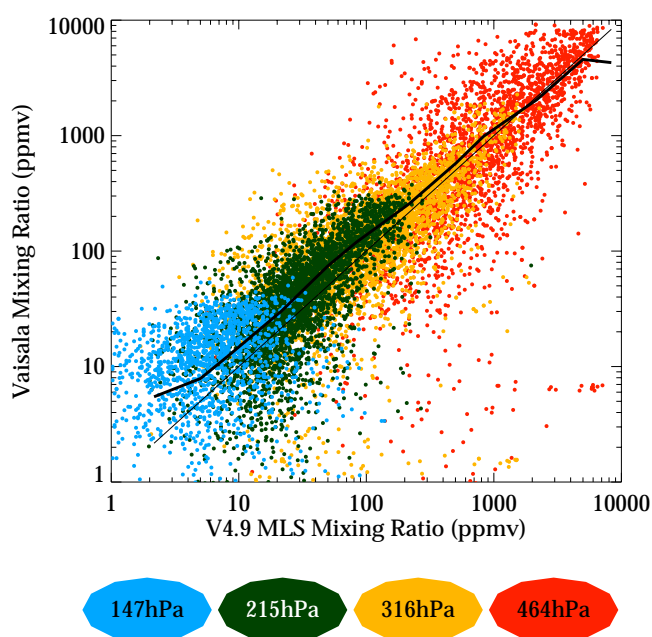


**Plate 24.** Scatter between Vaisala radiosonde and MLS V4.9 UTH measurements. Pressure level of the measurements is color coded. One to one (thin) and averaged (thick) lines are shown.

Based on the LR fit, the radiosonde measurements are on average within 20 %RHi of MLS which is within the typical MLS estimated accuracy of 20–25 %RHi. MLS tends to be drier than the Vaisala radiosonde at the highest relative humidities. At 316 and 464 hPa this could be caused by poor MLS UTH sensitivity and resulting a priori influence. The correlation coefficients on all four levels are consistent with that expected from comparing an in situ measurement with an MLS volume averaged-humidity. The previous statement assumes a standard deviation of the volume average based on MOZAIC along-track measurements. Except at 147 hPa, the correlations, slopes, and intercepts for the Vaisala radiosonde are similar to that with the FPH comparisons which had a looser coincidence criteria. The MLS correlation at 147 hPa is poorer with Vaisala radiosondes than it is with FPH. This could be caused by increased Vaisala errors at low temperatures. The humicap sensor response time increases exponentially as temperature decreases. At  $-50^{\circ}\text{C}$  the Vaisala radiosonde response time is 54 s and the balloon rises 250 m altitude [Miloshevich *et al.*, 2001]. In this case, the measurement generally is indicative of the humidity at a somewhat lower altitude than reported.

The ODR fit gives the bias and scaling values for the case where V4.9 MLS and radiosonde UTH are equally uncertain. The ODR fits have negative biases with slopes greater than 1 giving MLS UTH a dry tendency at low %RHi and a wet tendency at high %RHi. The ODR results improve the average agreement between MLS and the radiosondes at 316 and 464 hPa but make it worse for the two levels above that. The differences between the LR and ODR fits and the inability to know exactly the measurement uncertainties to apply to each measurement makes it difficult to determine the exact relationship between V4.9 MLS UTH and the Vaisala radiosonde.

**6.3.2. Comparison with temperature-corrected Vaisala radiosondes.** Numerous balloon flights of an instrument package consisting of an FPH, a particle replicator and a Vaisala RS80-A radiosonde humicap sensor demonstrated that the humicap has a dry bias in the upper troposphere under cloudy conditions [Miloshevich *et al.*, 2001]. The dry bias is caused by extrapolating the Vaisala humidity calibration coefficients which are a linear function in temperature below  $-20^{\circ}$ . Errors caused by the response time of the RS80-A at very low temperatures are much smaller than the errors caused by extrapolating the A-type humidity calibration coefficients for temperatures between  $-70^{\circ}\text{C}$  and  $-20^{\circ}\text{C}$ . A scaling polynomial as a function of temperature was fitted to the Vaisala data to make its mean measurement nearly match the FPH humidity. Such scaling, in principle, could allow older Vaisala data to be corrected. This was done for the MLS-radiosonde coincidences and

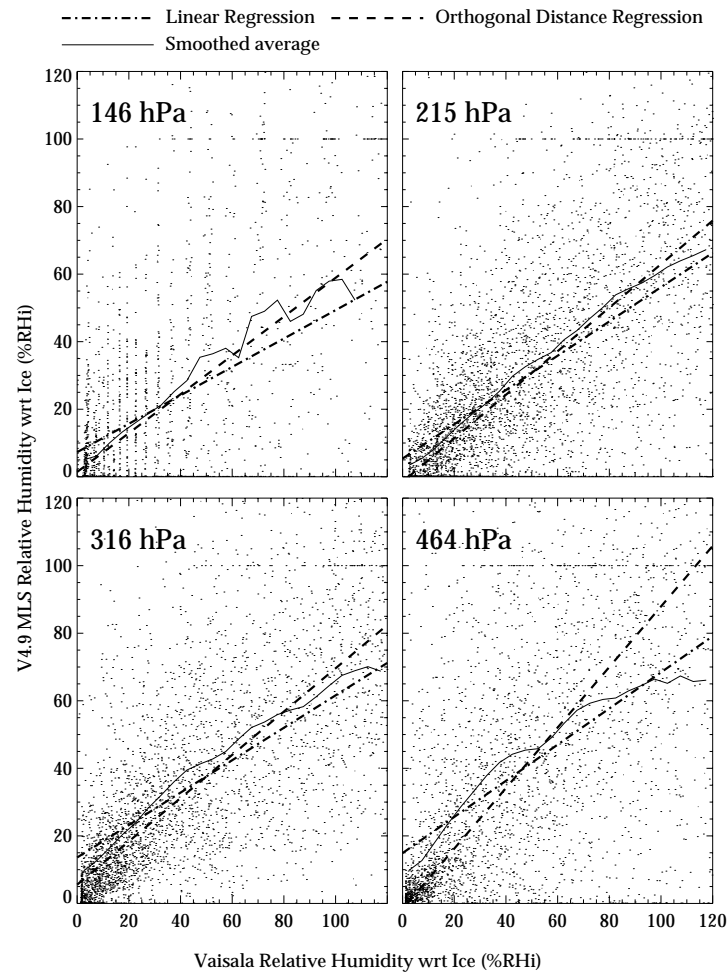


**Figure 11.** Same as Figure 10, except the Vaisala radiosondes are scaled by the *Miloshevich et al.* [2001] temperature correction.

the results shown in Figure 11. The MLS agreement with the corrected Vaisala is much worse than with the “uncorrected” Vaisala, and the cause of this worsening is not understood. Curiously, even the ODR fit which produces a slope over 2 for the uncorrected Vaisala data at 147 hPa is less than 0.6 with the correction. The correction is very large, a factor of 2–2.5 at the lowest temperatures. The correction applies only to the Vaisala humicap sensor with the A-type dielectric whose data are processed with Vaisala supplied calibration tapes. The radiosonde archive does not distinguish among the RS80 sensor types nor does it provide any information regarding the data processing; however, the measurements are reported in dewpoint depression which is a derived quantity. Since most of the correlative data were taken in the early 1990s, prior to incorporation of the H-type sensor into the radiosonde network, we have assumed that the Vaisala data used here are from the A type. Also the SAGE II validation exercise which used 1987 sonde data, prior to the H type sensor, does not show a factor of 2 disagreement with the Vaisala radiosonde [Larsen *et al.*, 1993].

The behavior of the archived Vaisala RS80 data used here is inconsistent with the correction given by Miloshevich *et al.* [2001]. Comparing the zonal Vaisala radiosonde average, Plate 14, with a scatterplot of coincident RS80-A and FPH humidities [Miloshevich *et al.*, 2001, Figures 2 and 3] illustrates the inconsistency. The RS80-A humidity is half of that measured by the FPH and almost never above 50 %RH<sub>i</sub>(~25 %RH<sub>w</sub>); however, over the tropics at 147 hPa which has a mean temperature less than -60°C, the Vaisala average from the archived data is 80-90 %RH<sub>i</sub>. It appears certain that the archived Vaisala radiosonde data have been processed differently than that by Miloshevich *et al.* [2001]. An example of using a different correction scheme is given by Anderson [1994].

**6.3.3. Comparison of MLS V4.9 and V5 UTH with Vaisala radiosondes.** A global average profile of all the coincidences between MLS V4.9 and V5 and Vaisala radiosondes is shown in Figure 12. The V5 has good average agreement with uncorrected Vaisala radiosonde because the wet continuum function was determined using Vaisala humidity measurements. The poorer agreement at 464 hPa for both V4.9 and V5 reflects problems with bad retrievals and a priori influence.

#### 6.4. MOZAIC

The collaborative European environmental research program MOZAIC (Measurement of Ozone and Water Vapor by Airbus In-Service Aircraft) was initiated in 1993 [Marenco *et al.*, 1998]. MOZAIC measures temperature, ozone, and water vapor using sensors installed on five Airbus A340 air-

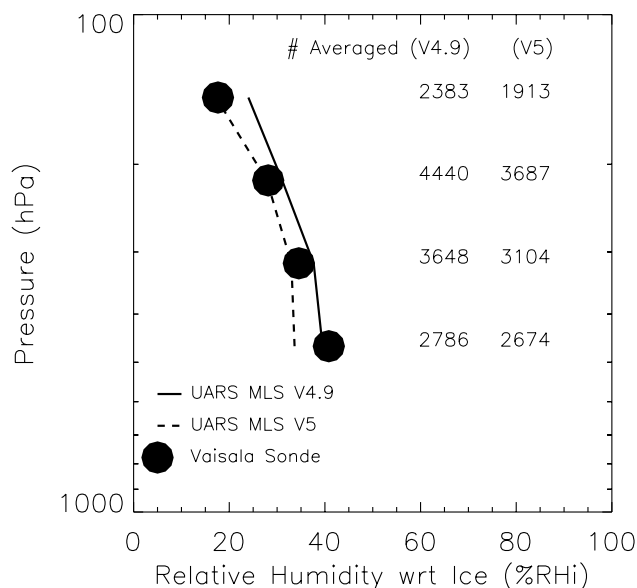


**Figure 12.** Average coincident Vaisala (bullets), V4.9 MLS (solid line), and V5 MLS (dashed line) profiles.

craft in normal commercial service. Water vapor is measured with a Vaisala thin-film humicap sensor incorporating the superior H-type dielectric which is routinely calibrated and is accurate to 4% at -40°C and 7% at -60°C. A typical flight cruises at 230 hPa and the atmospheric temperature is -50°C to -55°C. Measurements are taken every minute during the flight. MOZAIC Version 3 data from August 1994 through May 1998 were made available for MLS comparisons. The MOZAIC data were scanned for coincidences with MLS measurements. The same coincidence criterion was used as that for comparing sondes (1° longitude, 1° latitude, and 3 hours). Usually, several MOZAIC measurements occur within a single MLS coincidence criterion. The coincident MOZAIC data were screened according to the following criteria: (1) potential vorticity (from European Centre for Medium-Range Weather Forecasts analyses which are supplied with the data) between -2.0 and  $2.0 \times 10^{-6} \text{ km}^2 \text{ kg}^{-1} \text{ s}^{-1}$  (PVU), and (2) level flight path having pressure less than 260 hPa. The coincident flight path data (temperature, pressure, and relative humidity) were averaged inside the coincidence window to yield a single value for comparing with MLS. The MOZAIC data were converted to ice relative humidity using the World Meteorological Organization relative humidity function supplied with the data and the MOZAIC temperature measurement. The MLS

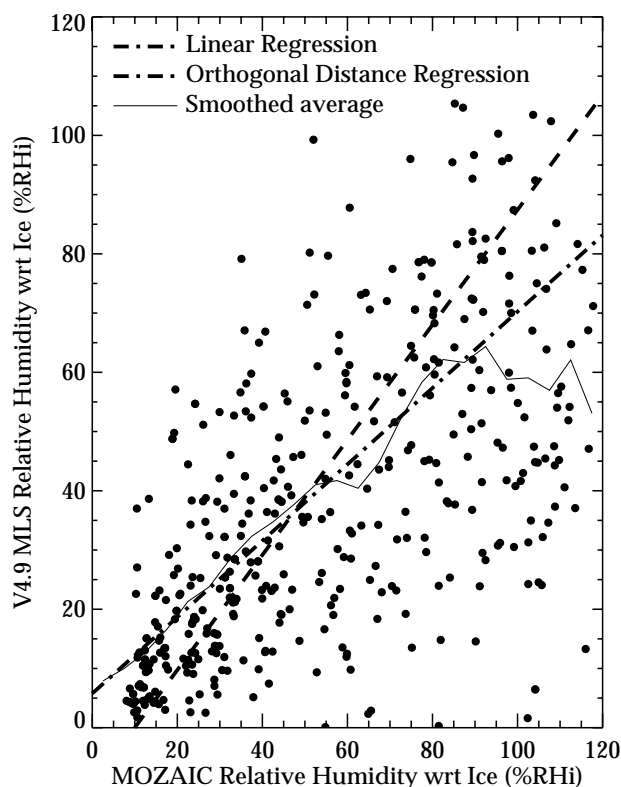


**Figure 13.** MOZAIC and V4.9 MLS UTH scatterplot at the MOZAIC altitude 180–260 hPa. The MLS %RH was linearly interpolated to the MOZAIC altitude. The best fit line and a smoothed average (same method as Figure 10) are overlaid. Printed with permission from Kley *et al.* [2000].

water vapor value used for comparison is obtained from linearly interpolating between the adjacent MLS retrieval surfaces to the average MOZAIC pressure. The MLS data were adjusted for the presence of cirrus according to section 4, but the 316 hPa data were not screened because their influence on the final interpolated MLS UTH is minor. A total of 461 coincidences were obtained and are shown as a scatterplot with best fit LR and ODR lines overlaid in Figure 13.

The MOZAIC data set suggests that MLS V4.9 humidity on average is low at 215 hPa. The LR fit suggests that MLS has a large dry bias at high %RH, whereas the ODR fit alleviates the dry bias somewhat. The correlation of MLS and MOZAIC data is similar to that of MLS comparisons with radiosondes and FPH at 215 hPa. Overlaid is a smoothed curve indicating the average MLS %RH as a function of MOZAIC %RH which shows linearity from 0 to 95 %RH.

Above 95 %RH the correlation breaks down and the average MLS humidity stops increasing. For this reason we only used MOZAIC data measuring relative humidity < 100 %RH for establishing the LR and ODR intercept and slope parameters; 17% of the coincident MOZAIC data exceed 100 %RH. The reason for the poor correlation with MOZAIC humidities > 100 %RH is not understood.

### 6.5. Comparisons of MLS UTH and CLAES Detection of Cirrus

Results from the Cryogenic Limb Array Etalon Spectrometer (CLAES) on UARS [Roche *et al.*, 1993] showing detection of subvisible cirrus (SVC) at 215, 147, 100, and 68 hPa have been reported [Mergenthaler *et al.*, 1999]. The CLAES experiment operated during the first 1.5 years of the UARS mission until its cryogen evaporated. CLAES provides an ideal correlative data set for MLS because its measurement track is virtually coaligned (within 30 s and 200 km along the measurement track at all times) with MLS. Subvisible or thicker cirrus is detected whenever the extinction measured in the CLAES  $780\text{ cm}^{-1}$  (blocker 9) spectrometer is  $\geq 9 \times 10^{-4}\text{ km}^{-1}$ . If the associated cirrus extinction has an error greater than 30% of its value then the underlying atmosphere is considered obscured and the extinction profile below it is not used for cloud detection [Mergenthaler *et al.*, 1999]. These criteria are sufficient to discriminate against sulfate aerosol and overlaying cirrus. As an illustration of the good tracking between CLAES cirrus detection and V4.9 MLS UTH > 100 %RH, Plate 25 shows a 1 day orbit series of MLS UTH overlaid by CLAES cirrus detection for September 8, 1992. Data gaps in Plate 25 are due to the following: (1) 316 hPa MLS data that fail section 4 quality test, (2) on every other orbit for 10 min, CLAES operates in a spectral sweeping mode for calibration and other science studies, (3) the bottom of the CLAES vertical coverage is sometimes above 215 hPa, and (4) situations where upper level thick clouds obscure the lower levels. CLAES cirrus and high MLS relative humidities appear to track best at 147 hPa and worst at 316 hPa. Differences between MLS and CLAES at any height are probably caused by coincidence issues which are still important at the 200 km scale. Also CLAES is much more sensitive than MLS to condensed water anywhere along its line of sight. The cirrus sensitivity difference between CLAES and MLS increases sharply with decreasing altitude.

The left panel of Plate 26 shows, for the entire CLAES lifetime, a scatter density plot of all the CLAES 147 hPa extinction values between  $40^\circ\text{S}$  and  $40^\circ\text{N}$  and coincident V4.9 MLS UTH. The plot is divided into four quadrants according to cirrus criteria for each instrument. Ideally, one would like to see only the lower left quadrant (both instruments

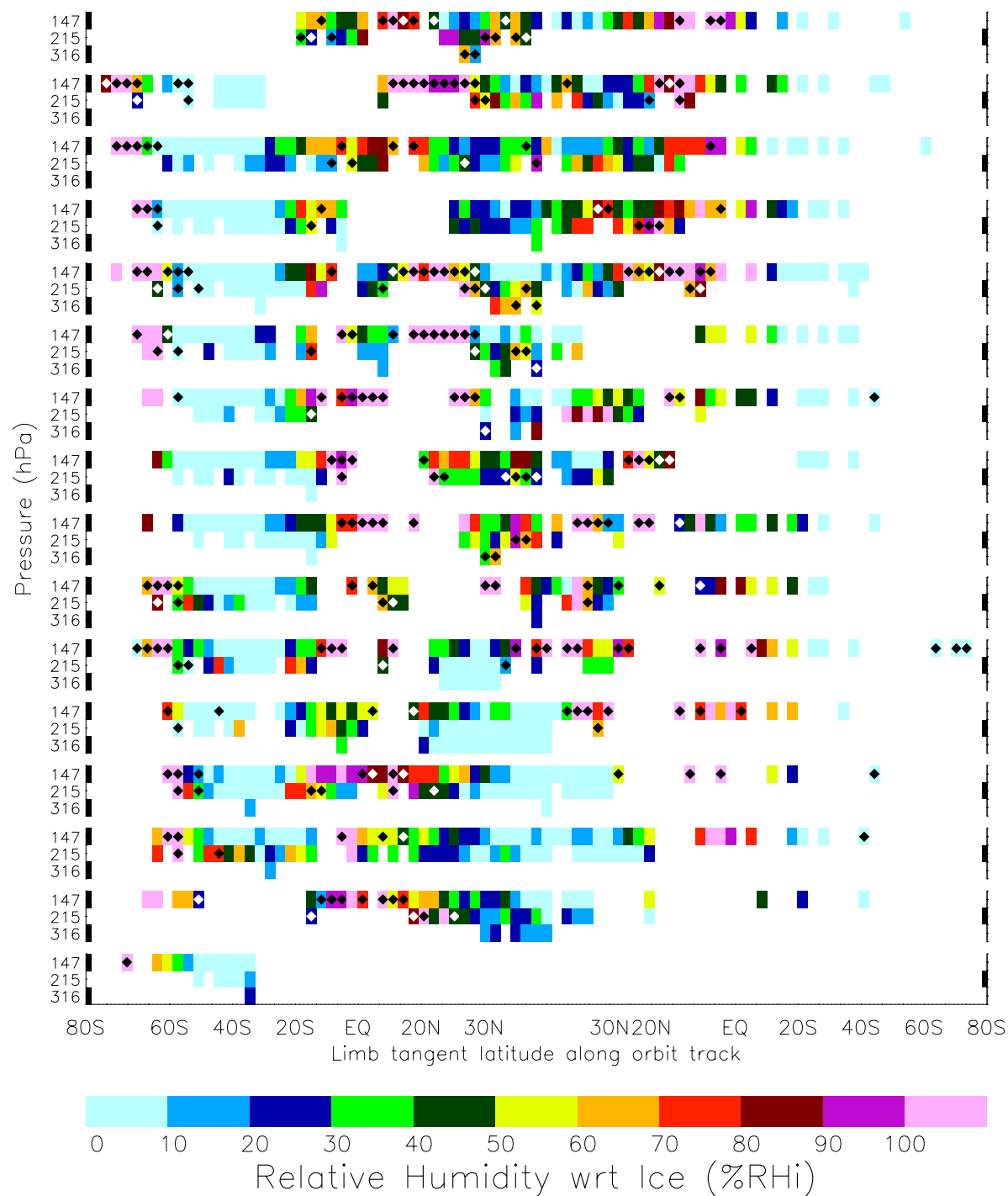


**Plate 25.** Example of MLS UTH and CLAES cirrus detection for September 8, 1992. Each strip is a complete orbit. Data shown are where both MLS and CLAES have measurements on this day. CLAES cirrus detection (extinction greater than  $0.0009 \text{ km}^{-1}$ ) is indicated by diamonds.

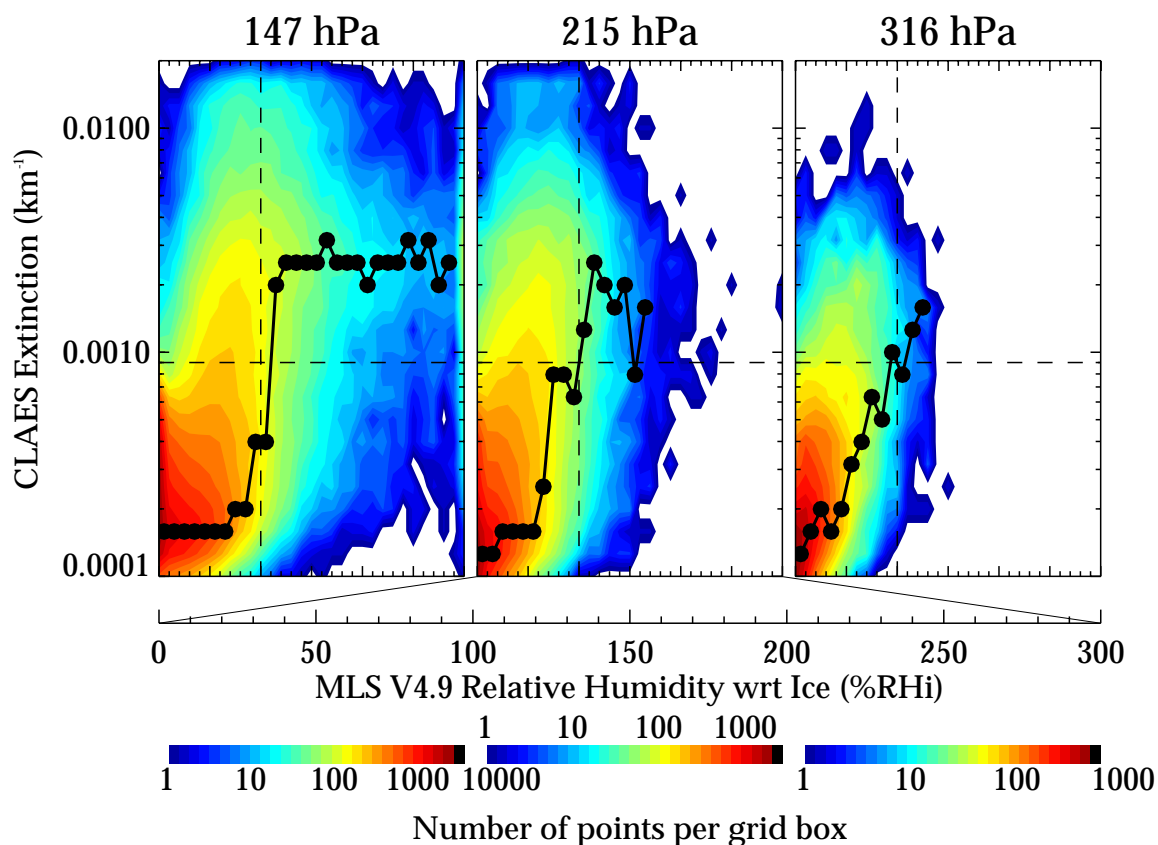


**Plate 26.** A scatter density plot of coincident CLAES extinction and V4.9 MLS UTH at (left) 147 hPa, (center) 215 hPa, and (right) 316 hPa for the entire CLAES data set during its operational lifetime. The color bars indicate the number of points per grid box; note that the scale is logarithmic and different for each pressure. The connected bullets show the most probable CLAES extinction as a function of MLS %RH<sub>i</sub>. The vertical dashed line is MLS humidity of 100 %RH<sub>i</sub>, and the horizontal dashed line is CLAES extinction of  $0.0009 \text{ km}^{-1}$  which are minimum values that indicate detection of cirrus.



see clear sky) and the upper right quadrant (both instruments see cirrus) populated, but there is a significant population of points in the upper left quadrant (MLS clear sky, CLAES cirrus) especially when MLS measures more than 50 %RH<sub>i</sub>. There are fewer points in the lower right quadrant indicating MLS cirrus while CLAES is clear. The most probable value of CLAES extinction as a function of MLS UTH is also shown, and a very steep gradient occurs between 85% and 115% RH<sub>i</sub>, indicating that when the MLS UTH measurement exceeds 115 %RH<sub>i</sub>, CLAES most likely detects cirrus. The cause of the large density of points between 50 and 100 %RH<sub>i</sub> and CLAES cirrus detection may be a consequence of sensitivity and coincidence issues. CLAES cirrus threshold varies considerably with ice water content (IWC) and effective particle radius, but assuming 0.8  $\mu\text{m}$  for the latter (which is considered a maximum value for SVC) would place the CLAES detection threshold at  $3 \times 10^{-6} \text{ g m}^{-3}$  [Mergenthaler et al., 1999]. This is at least 3 orders of magnitude below the MLS IWC detectability. Therefore the MLS UTH is more sensitive to any subsaturated air within the measurement volume than it will be to the added emissions from SVC. If cirrus is anywhere along the line of sight except in the limb tangent layer, it is plausible for MLS relative humidity to be considerably less than 100 %RH<sub>i</sub>. Although not observable in Plate 26 there are a small number ( $\sim 70$  pts out of 239101) of 0.1 %RH<sub>i</sub> MLS values where CLAES detects cirrus, indicating a situation where the MLS retrieval has failed to give the correct result. This is probably caused by a severe horizontal UTH gradient in the lower levels which is not properly accounted for in the retrieval.

The center panel of Plate 26 shows the CLAES extinction and V4.9 MLS UTH scatter density at 215 hPa. Qualitatively this figure is similar to 147 hPa and the same discussion applies. The gradient in the most probable value is not as steep at this height, rising sharply from 65% to 115% RH<sub>i</sub>. Coincident very high MLS %RH<sub>i</sub> values are considerably rarer at 215 hPa than 147 hPa. This is expected because the 100 %RH<sub>i</sub> vapor emission is much larger due to higher temperatures which significantly increases the IWC detection threshold in MLS data. MLS detection of ice will be limited mostly to cirrus associated with strong convection where the CLAES extinction profile stops at the cloud top, most likely at 100 or 147 hPa with extinction at 215 hPa and below obscured.

The right panel of Plate 26 shows the CLAES extinction and V4.9 MLS UTH scatter density at 316 hPa. The amount of 316 hPa data is 10 times less than at 147 hPa level, mostly caused by blocking out by upper level cirrus in the CLAES data set and the MLS 316 hPa data screening criteria. Qualitatively, the 316 hPa scatter density is similar to those at 147 and 215 hPa except the most probable value no longer has

a sharp gradient but rather is nearly linear from 5% and up crossing the CLAES ice detection threshold at 95–105%.

## 6.6. Summary of Coincident Comparisons

Table 8 shows the average correlative “bias” and “scaling” between MLS and (1) Vaisala, (2) low-temperature corrected Vaisala, (3) FPH, and (4) MOZAIC from LR and ODR. The MLS UTH LR biases relative to the in situ methods compared are small, positive, and less than  $1\sigma$  MLS estimated uncertainty for the upper two levels (147 and 215 hPa). The LR average bias is larger for the lower two levels (316 and 464 hPa), approaching the accuracy estimate. The ODR derived biases between MLS UTH and the in situ methods are usually negative values sometimes as large as the estimated accuracy. The scaling factors derived from LR fits tend to be less than 1 for these comparisons but the ODR fits with the exception of the temperature corrected Vaisala sondes are usually greater than 1.

The linear fits between MLS V4.9 and the in situ methods broadly show agreement but with much variability. The LR results show that individual comparisons indicate MLS too wet at the lowest humidities and MLS too dry at the highest humidities. If MLS and in situ are accurately measuring UTH, then this result is anticipated from an intercomparison where the volume averaging issue is significant; however, it is also possible that V4.9 MLS UTH is too dry at high %RH<sub>i</sub>. Limitations in the measurement system are expected to have a dry tendency at high %RH<sub>i</sub> for 316 and 464 hPa. The ODR fit provides some insight how uncertainties associated with comparing a volume averaged measurement to an in situ measurement might affect the linear relationship. The large difference between the LR and ODR fits do not provide a strong constraint on the accuracy of MLS UTH. However, deviations from either or both best fit lines are for most cases consistent with the MLS accuracy estimates. The one significant exception being the temperature-corrected Vaisala radiosondes. Applying the low-temperature correction to the archived Vaisala radiosonde data has MLS dry by a factor of 2 (or more) in the upper two levels which is inconsistent with the FPH comparison. For reasons not understood, MLS comparisons with (1) FPH and archived Vaisala radiosondes, (2) high average relative humidities over the tropics at 147 hPa derived from the archived Vaisala radiosonde data, and (3) SAGE II comparisons with archived Vaisala radiosondes all suggest that the low-temperature correction given by Miloshevich et al. [2001] should not be applied to the archived Vaisala data.

Table 9 also gives the minimum MLS %RH<sub>i</sub> where CLAES most probable extinction indicates cirrus. CLAES cirrus detection correlates well with V4.9 MLS UTH between 95–115 %RH<sub>i</sub> at 147, 215, and 316 hPa levels.

**Table 8.** Summary of MLS V4.9 “Bias” and “Scaling” With in Situ Measurements<sup>a</sup>

Pressure, hPa	Vaisala Radiosondes		Corrected Vaisala <sup>b</sup>		Frostpoint		MOZAIC <sup>c</sup>	
	Bias,		Bias,		Bias,		Bias,	
	%RHi	Scaling	%RHi	Scaling	%RHi	Scaling	%RHi	Scaling
147	8.4(−16.5)	0.89(2.29)	7.3(1.9)	0.42(0.56)	−1.1(−4.3)	1.08(1.23)		
215	3.9(−14.3)	0.97(1.61)	5.4(−2.7)	0.51(0.67)	3.8(−23.3)	0.80(1.38)	5.8(−11.5)	0.65(1.01)
316	12.3(−2.2)	0.73(1.15)	13.6(6.4)	0.73(1.15)	20.6(−1.4)	0.61(1.13)		
464	13.0(−10.6)	0.65(1.23)	14.9(−3.9)	0.65(1.23)	20.4(−7.9)	0.86(1.60)		

<sup>a</sup>Linear regression values are followed by orthogonal distance regression values in parentheses.

MLS V4.9 %RHi = bias + scaling × (in situ %RHi).

<sup>b</sup>Vaisala measurements are scaled by recommended low-temperature polynomial [Miloshevich *et al.*, 2001].

<sup>c</sup>MLS is interpolated to MOZAIC altitude which is above 260 hPa.

**Table 10.** MLS V4.9 and in Situ Correlation Coefficient  $r$  and Standard Deviation  $\sigma_{\text{MLS UTH}}$  About the LR Line

Pressure, hPa	Vaisala Radiosondes		Corrected Vaisala <sup>a</sup>		Frostpoint		MOZAIC <sup>b</sup>	
	$\sigma_{\text{MLS UTH}}$ ,		$\sigma_{\text{MLS UTH}}$ ,		$\sigma_{\text{MLS UTH}}$ ,		$\sigma_{\text{MLS UTH}}$ ,	
	$r$	%RHi	$r$	%RHi	$r$	%RHi	$r$	%RHi
147	0.54	27.6	0.60	25.8	0.89	18.9		
215	0.69	22.7	0.67	23.3	0.63	24.3	0.64	21.2
316	0.67	22.4	0.66	22.6	0.55	25.1		
464	0.58	27.4	0.55	27.9	0.62	22.9		

<sup>a</sup>Vaisala measurements are scaled by recommended low-temperature polynomial [Miloshevich *et al.*, 2001].

<sup>b</sup>MLS is interpolated to MOZAIC altitude which is above 260 hPa.

**Table 9.** Minimum %RH<sub>i</sub> Where CLAES Extinction Indicates Cirrus<sup>a</sup>

Pressure, hPa	CLAES Cirrus, Most Probable %RH <sub>i</sub>
147	≥ 115
215	≥ 105
316	≥ 95

<sup>a</sup>This is the minimum %RH<sub>i</sub> where the peak of the distribution of coincident CLAES extinctions indicates cirrus.

Table 10 shows the linear correlation coefficient between V4.9 MLS UTH and the other in situ techniques. The correlation coefficients are similar. The correlation coefficient gives the average standard deviation of the measured MLS UTH relative to the LR corrected in situ UTH according to

$$\sigma_{\text{MLS UTH}} = m \sigma_{\text{atm}} \frac{\sqrt{1-r^2}}{r}, \quad (22)$$

where  $\sigma_{\text{MLS UTH}}$  is the MLS standard deviation with respect to the in situ measurement,  $m$  is the scaling factor between MLS and the in situ humidity,  $\sigma_{\text{atm}}$  is the standard deviation about the mean atmospheric humidity, and  $r$  is the linear correlation coefficient. The scaling factor,  $m$  is estimated from the linear regression between MLS and the in situ technique and  $\sigma_{\text{atm}}$  is approximated with the standard deviation of the in situ data. Equation (22) is equivalent to  $(\sigma_{\text{meas}}^2 - m^2 \sigma_{\text{atm}}^2)^{1/2}$  which can be shown to be equivalent to  $[(1/N) \sum_i (y_i - mx_i - b)^2]^{1/2}$ , the standard deviation of the measurements relative to the LR line, where  $b$  is the bias or intercept and  $N$  is the sample size. The  $1/N$  is normally  $1/(N-2)$  if  $m$  and  $b$  are determined from the data; however, to complete the derivation,  $N-2 \approx N$  is used for a large sample. Table 10 shows the standard deviation of the differences between V4.9 MLS UTH and the other in situ measurements. Nearly all these values are about 25 %RH<sub>i</sub>. We feel that the most dominant contributing sources to  $\sigma_{\text{MLS UTH}}$  are variations due to comparing volume averages to in situ data and MLS precision. Along-track MOZAIC humidities show that UTH variability in a slice taken through the MLS measurement footprint has a standard deviation of 20 to 30 %RH<sub>i</sub> about the average. The estimated V4.9 MLS precision is 8–21 %RH<sub>i</sub>. The correlation coefficients and standard deviations of the mean are somewhat better than the root sum square of these two contributing factors, indicating the linear correlation coefficients of the coincident comparisons are reasonable. There is no evidence to suggest that coincidence differences or uncorrelated forward model errors are significant.

## 7. Comparisons of V4.9 MLS UTH With Meteorological Fields

### 7.1. Consistency With Upper Tropospheric/Lower Stratospheric Dynamics

Several publications have shown the scientific value of the preliminary MLS UTH data product [Read *et al.*, 1995] for use in meteorological studies. Newell *et al.* [1996a] showed observations of cirrus associated with rising motions and coincident with high relative humidities at 147 hPa in the MLS UTH data. The dynamics of the east-west Walker circulation has been investigated in terms of the divergent wind fields and MLS UTH [Newell *et al.*, 1996b]. The velocity potential and divergent winds are useful in identifying upwelling and subsidence regions in the tropics which are associated with the rising and sinking branches of the Walker and Hadley circulation cells. MLS UTH shows good correlation with the divergent winds, illustrating that the longitudinal distribution of tropical upper tropospheric water vapor is largely consistent with the circulation [Newell *et al.*, 1996b; Stone *et al.*, 2000]. A good example [see Stone *et al.*, 2000, Figure 2] shows a 6 year average of MLS UTH at 215 hPa overlaid on a velocity potential and divergent wind field map. The extratropical Southern Hemisphere summer circulation pattern is often dominated by medium-scale waves associated with baroclinic growth and decay. This behavior was examined using geopotential height and potential vorticity analysis and was shown to have good correspondence to MLS UTH features [Stone *et al.*, 1996]. The MLS UTH measurements were also included in a study which used assimilated winds and a chemical transport model to examine the large-scale mass transport from the troposphere into the stratosphere during a 1993 blizzard on the east coast of the United States [Rood *et al.*, 1997]. These studies demonstrate the general consistency of the MLS UTH measurements with upper tropospheric dynamics.

The pressure levels on which MLS retrieves UTH can, at times, be located in the lower stratosphere in the extratropics. While the MLS 202/204 GHz UTH measurement is not sensitive to the small variations in mixing ratios in the stratosphere, one can identify a coherent boundary between the troposphere and the drier lowermost stratosphere. Plate 27 shows a daily V4.9 MLS UTH map (in mixing ratio) for March 14, 1993, a day the east coast experienced a blizzard whose dynamical characteristics are described by Rood *et al.* [1997]. Humidity values and potential vorticity (PV) contours usually associated with the tropopause are approximately aligned.  $|PV| > 2 \times 10^{-6} \text{ km}^2 \text{ kg}^{-1} \text{ s}^{-1}$  denoting stratospheric air, correspond to stratospheric-like water vapor mixing ratios ( $< 10 \text{ ppmv}$ ). At 147 hPa there is a sharp latitudinal gradient in both the water vapor and PV

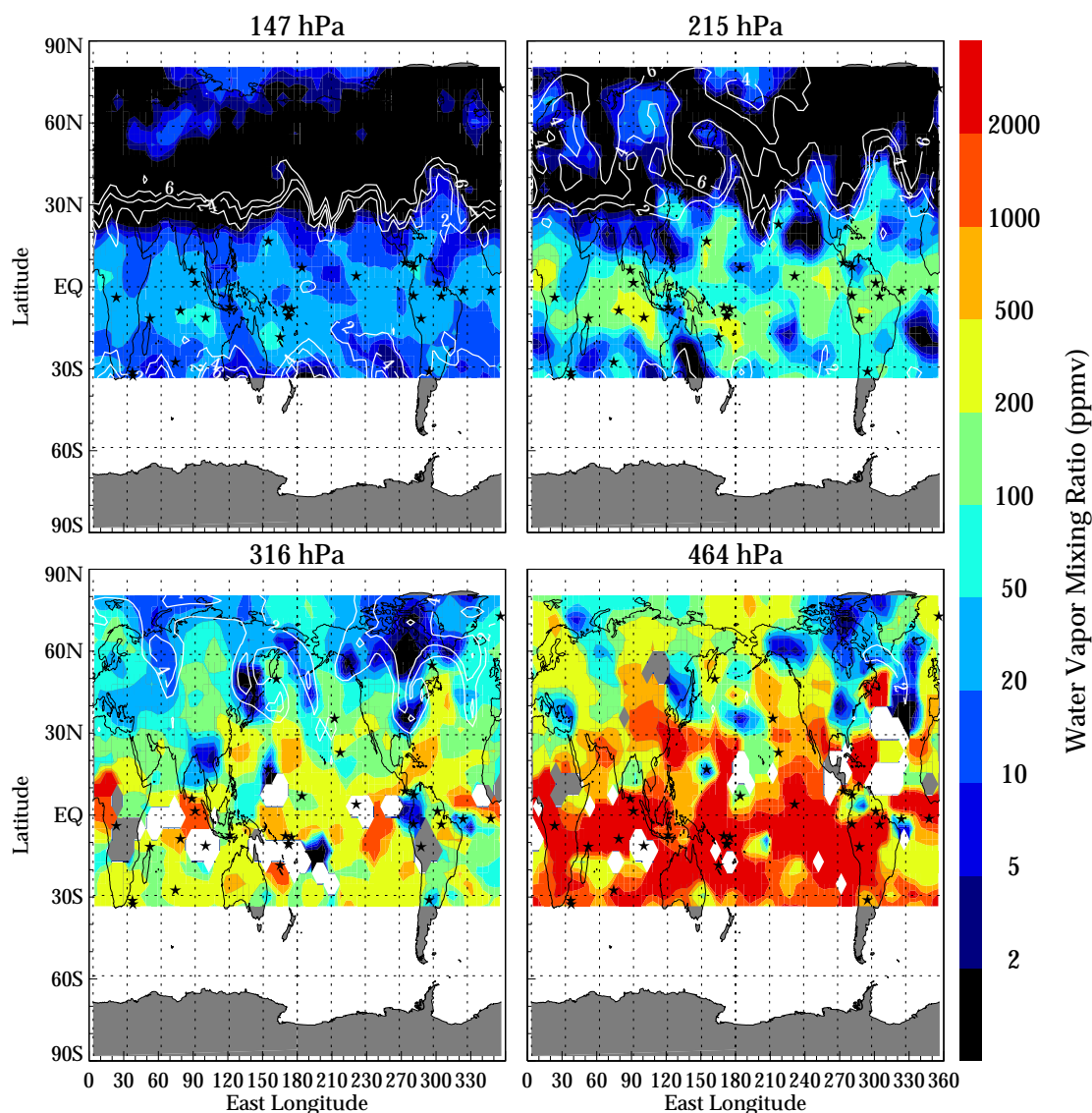


**Plate 27.** A map of V4.9 MLS UTH on March 14, 1993. The data are presented as color contours of mixing ratio for the four MLS surfaces (white and grey areas indicate no data due to viewing geometry or data screening of the 316 and 464 hPa levels). Absolute values of potential vorticity (PV, contours are 2, 4, and 6 PVU where  $\text{PVU} = 10^{-6} \text{ km}^2 \text{ kg}^{-1} \text{ s}^{-1}$ ) are overlaid as white contour lines.  $|\text{PVU}| = 2$  approximately denotes the boundary between the troposphere and stratosphere [Holton *et al.*, 1995]. Stars indicate measurements made in the presence of significant scattering (i.e. thick cirrus with ice particles  $> 100 \mu\text{m}$ ) which is detected when the lowest altitude radiance is depressed by more than 50 K. This is one of the standard daily analyses products produced by the MLS.

near 30°N. At 215 hPa the PV gradient is not as great but there is a reasonable correlation between the high PV and dry regions. High PV and low mixing ratios are also seen to coincide at the 316 hPa level. The 316 hPa map clearly show dry stratospheric air descending to very low altitudes during the March 1993 U.S. east coast blizzard.

## 7.2. Comparison of MLS V4.9 UTH and GEOS 2 UTH

A rich source of humidity data is available from the Goddard Earth Observing System (GEOS) data assimilation model [Schubert *et al.*, 1993]. The assimilation produces a horizontally gridded humidity field every 6 hours on 2.5° longitude by 2° latitude on 22 heights including 500, 400, 300, 250, 200, and 150 hPa that are relevant for comparisons with V4.9 MLS UTH. The GEOS upper air moisture analysis uses radiosonde observations up to 300 hPa altitude. Moisture above 300 hPa is determined by extrapolating the lower altitude moisture according to the assimilating model and observations of other quantities (e.g., temperature and winds). Comparing with an assimilation field offers some advantages over coincident measurement comparisons from radiosondes. Maps can be compared and a better assessment of the geographical nature of the differences can be obtained. The assimilation field UTH is also a volume average and more comparable to the MLS UTH measurement. A comparison between the preliminary MLS UTH retrieval at 215 hPa and the GEOS 1 field at 200 hPa has been done [Chen *et al.*, 1998]. Here we compare the improved GEOS 2 humidity with the V4.9 MLS UTH field on the four MLS retrieval surfaces. The GEOS 2 has clouds forming at subfreezing temperatures [Chen *et al.*, 1998] when humidity is 100 %RH<sub>i</sub> instead of 100 %RH<sub>w</sub>.

We compare MLS 4.9 UTH data with GEOS 2 reanalyses humidity for December 1991 through February 1992 and June 1992 through August 1992. For the comparison between V4.9 MLS and GEOS 2 UTH, the GEOS 2 fields were sampled by the MLS measurement pattern. The logarithm of the GEOS 2 specific humidity is linearly interpolated to the MLS measurement location, time, and pressure. GEOS 2 temperature was interpolated linearly onto the MLS measurement pattern. Humidity was converted to %RH<sub>i</sub> using (9). Every MLS UTH point was compared to GEOS 2 in a scatterplot, and a best fit line determined. The scatterplots, not shown, are similar to those shown in section 6 but with over 200,000 points. The computed bias, scaling, correlation coefficient, and comparison standard deviation are presented in Table 11. The results are similar to the coincident comparisons but have slightly lower correlation coefficients and larger standard deviations. The GEOS UTH should represent a volume average comparable to V4.9 MLS UTH and therefore the ODR analysis is inappropriate.

We compare 3-month GEOS 2 and V4.9 MLS seasonal humidity maps. The GEOS 2 map in Plate 28 shows the 1992 Northern Hemisphere winter and Plate 29 shows the 1992 Northern Hemisphere summer. These maps were made by sampling the GEOS 2 fields in the same way that MLS samples the atmosphere. Plates 28 and 29 can be compared to the MLS climatology maps in Plates 10–13. The MLS and GEOS 2 maps are qualitatively similar. The GEOS 2 maps in Plates 28 and 29 are for an El Niño year, and there will be some relocation of moist features in these years relative to the MLS 6-year average. MLS maps of V4.9 UTH for the same time periods were made and differenced from the GEOS 2 and shown in Plates 30 and 31.

V4.9 MLS is considerably wetter than GEOS 2 at 147 hPa in the tropics except in a region off the west coast of South America (the descending branch of the Walker circulation) where MLS is only slightly wetter. The 147 hPa humidity at midlatitudes are in agreement to within 10 %RH<sub>i</sub>, but there is a band near 40°S in December-January-February (DJF) season or 40°N in the June-July-August (JJA) season where GEOS 2 is more than 20 %RH<sub>i</sub> wetter. The V4.9 MLS humidity at 147 hPa has a steeper tropics to midlatitude humidity gradient than calculated in the GEOS 2 assimilation. The GEOS 2 reanalysis has a considerably wetter winter high latitudes than MLS, although both fields have higher relative humidities in the winter polar regions than in midlatitudes.

The 215 hPa features are in very good qualitative agreement between GEOS 2 and V4.9 MLS. The Intertropical Convergence Zone (ITCZ) is slightly wetter in the MLS data. This is in contrast to the Chen *et al.* [1998] study and is most likely caused by changing the cirrus formation criteria from 100 %RH<sub>w</sub> to 100 %RH<sub>i</sub> in the GEOS 2 model. As noted by Chen *et al.* [1998], the high humidity regions tend to be spatially larger in the GEOS 2 reanalysis. Although the regions of high and low humidities are well colocated, except over the winter polar regions, the degree of dryness or wetness is more exaggerated in the MLS field. As with 147 hPa, the winter high latitudes are much wetter in the GEOS 2 reanalysis. The Vaisala radiosonde minus MLS climatology difference map, Plate 16, is reasonably consistent with the reanalysis differences shown Plates 30 and 31.

The difference map at the 316 hPa level is perhaps less coherent compared to the upper two levels, and generally V4.9 MLS is dry by 10–30 %RH<sub>i</sub> at 316 hPa. GEOS 2 has a wetter ITCZ than MLS. GEOS 2 is more humid than MLS over the southern high latitudes. Curiously, MLS has wetter northern high latitudes in JJA than does GEOS 2. It is interesting to compare these differences to those with the Vaisala radiosonde climatology difference (see Plate 17). The Vaisala differences in the tropics are consistent with those for GEOS 2. The GEOS 2 climatology does not show the large dif-

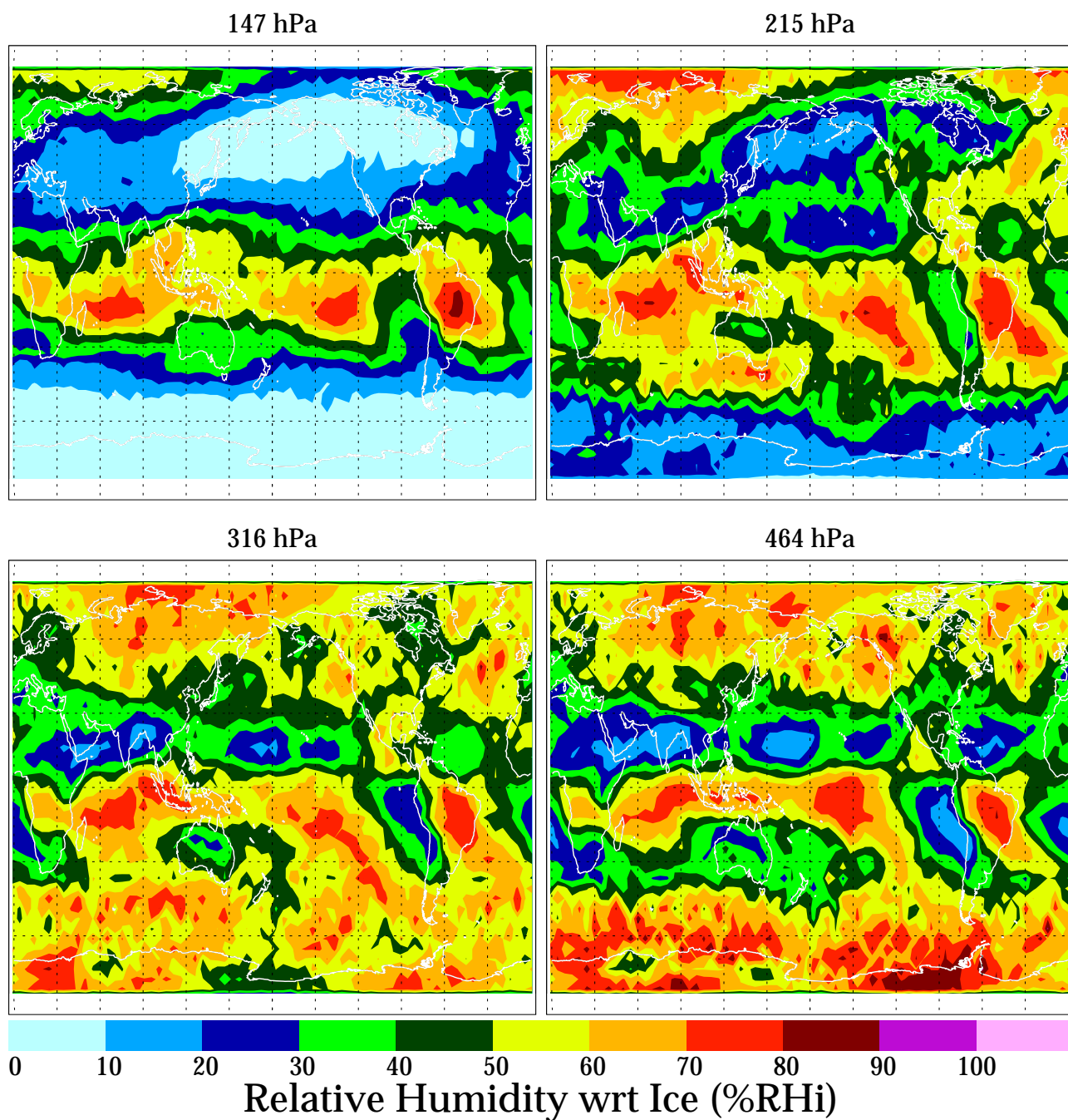


**Plate 28.** A mean seasonal map produced from GEOS 2 data sampled like MLS for December 1991 through February 1992.



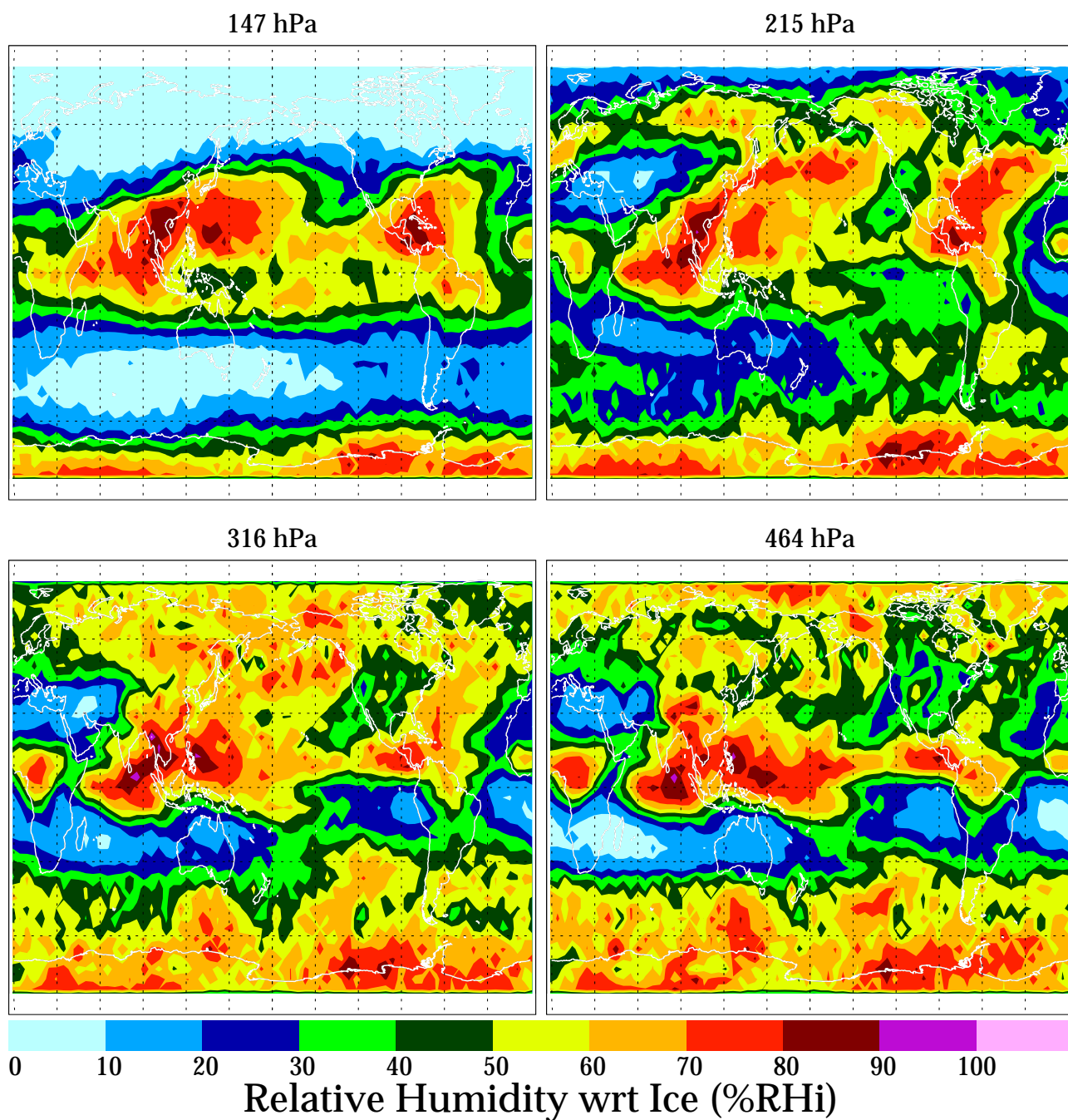


**Plate 29.** A mean seasonal map produced from GEOS 2 data sampled like MLS for June through August 1992.

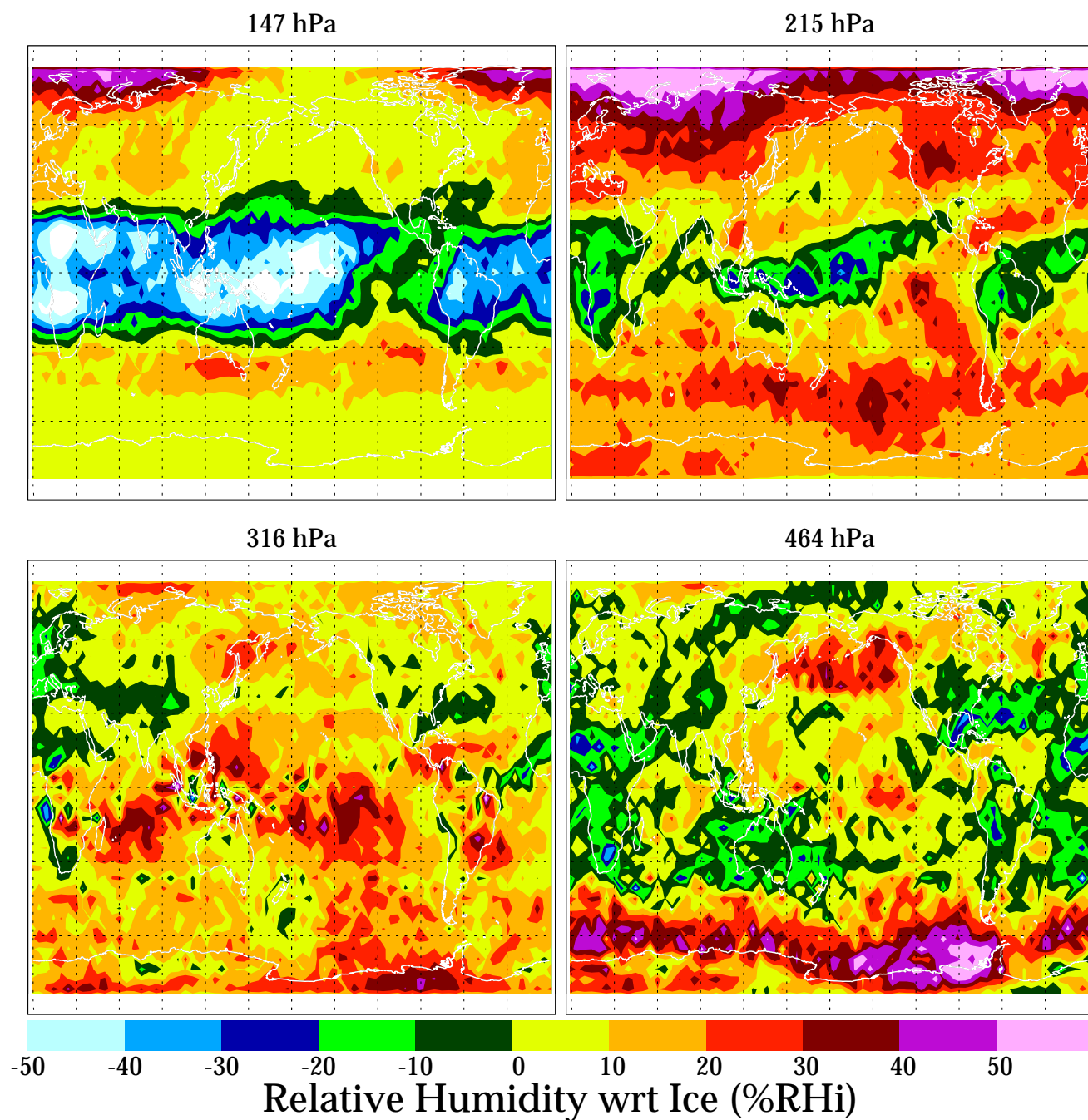


**Plate 30.** Map of GEOS 2 minus V4.9 MLS seasonal UTH map for December 1991 through February 1992.



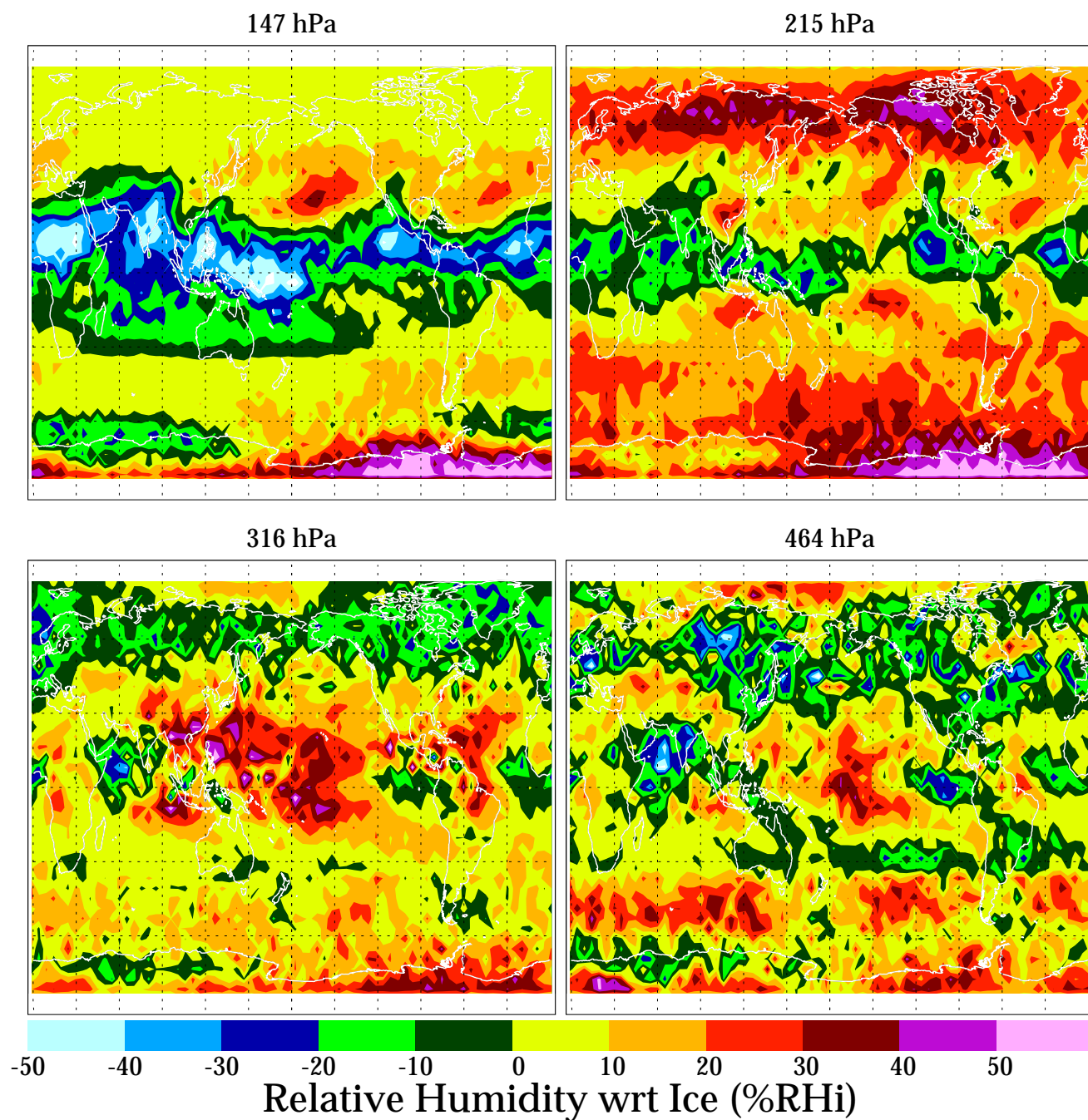


**Plate 31.** Map of GEOS 2 minus V4.9 MLS seasonal UTH map for June through August 1992.

**Table 11.** Comparison Characteristics Between MLS and GEOS 2 UTH

Pressure, hPa	Bias, <sup>a</sup> %RH <sub>i</sub>	Scaling <sup>a</sup>	Correlation Coefficient	Standard Deviation of Comparison, %RH <sub>i</sub>
147	6.0	0.84	0.63	29.4
215	−1.3	0.68	0.56	27.2
316	7.6	0.63	0.59	24.2
464	12.6	0.58	0.51	29.0

<sup>a</sup>MLS V4.9 %RH<sub>i</sub> = bias + scaling × (GEOS 2 %RH<sub>i</sub>).

ferences at mid-high northern latitudes (e.g., over the North Atlantic) that are seen in the radiosonde differences.

The agreement at 464 hPa between the reanalysis and V4.9 MLS is quite good and does not show an overall bias except over the Antarctic in DJF where the GEOS 2 is wetter. A large difference appears over the North Pacific in DJF which is caused by low MLS humidities extending further north than in the reanalysis. The radiosonde and V4.9 MLS differences (Plate 18) tend to be more consistent with the GEOS 2 and V4.9 MLS differences at this level than at the upper levels.

## 8. Conclusions

The methodology of retrieving upper tropospheric humidity from MLS is described. It uses a vertical profile of radiances in the water vapor/oxygen absorption coefficient function window region near 202 and 204 GHz. The method relies on characterizing the radiances in terms of dry, wet, and known contaminant species contributions. The wet continuum provides the humidity. Measuring humidity from the wet continuum is different from that used for other MLS measurements because it does not observe a spectral line and relies on absolute values of the radiances. The radiance signals are sufficiently understood for useful humidity measurements between 464 and 147 hPa. The estimated uncertainty of the retrieved UTH product is based on the accuracy of radiance forward model used to calculate radiances. Therefore the retrieved uncertainty estimates are interpreted as accuracy. Precision estimates have also been determined based on propagating the radiance noise and precisions of limb tangent pressure, temperature, and other contributing species into UTH. The 1 standard deviation UTH precision is 1–3 times smaller than the accuracy estimate depending on height.

Existing laboratory measurements of the dry and wet absorption coefficient functions near 203 GHz are representative of that observed from MLS radiances but have inadequate accuracy for retrievals. The necessary dry and

wet continuum functions were determined from upper tropospheric radiance measurements in situations where the atmospheric humidity was believed to be known. Radiances that are associated with dry conditions were used to infer the dry continuum function. MLS version 4.9 used tropical radiances measured in cirrus, assuming 100 %RH<sub>i</sub> humidity with negligible ice emission contributions, to scale the laboratory measured 213 GHz H<sub>2</sub>O—N<sub>2</sub>, wet continuum function. Version 5 used coincident Vaisala radiosonde humidity measurements to determine the wet continuum function. The V4.9 is the recommended version for scientific investigations.

The V4.9 MLS UTH validation concentrates on three types of comparisons with other data sets. These are climatological, coincident profile matches and consistency with meteorological fields.

The comparisons with climatological fields reveal sampling problems. The Vaisala radiosonde zonal climatology is roughly 20 %RH<sub>i</sub> wetter than MLS V4.9 UTH. A comparison with Vaisala global seasonal climatologies show that this is not a homogeneous bias. Most of the measurements were made over landmasses, and different biases between the MLS and Vaisala data sets are associated with different regions of the world. SAGE II tropical climatology is half as humid as MLS with better agreement toward higher latitudes. Some issues with these types of comparison are (1) MLS and SAGE II sample both oceans and land, whereas radiosondes sample mostly land, (2) SAGE II is limited to clear sky, whereas the radiosondes and MLS can measure humidity in cirrus, (3) SAGE II only gets 30 profiles a day, whereas MLS and radiosondes get > 1000 a day, (4) section 4 data quality screening introduces possibly a dry sampling bias at the 316 and 464 hPa levels because rejected data are usually accompanied with high humidity in the upper two levels, and (5) MLS has an asymmetric global coverage which changes approximately monthly and might affect a derived climatology poleward of 34°.

All the climatologies show similar features and appropriate tracking with the solar seasonal cycle. The different bi-

ases for comparisons of climatologies between V4.9 MLS UTH with different instruments and comparisons with the same instrument over different regions of the globe suggest that differences in sampling frequencies and limitations specific to each instrument type could be important factors. A quantitative statement about MLS UTH accuracy cannot be made based on these types of comparisons.

Correlative comparisons between MLS, frostpoint hygrometer, Vaisala radiosondes, and MOZAIC were undertaken to establish the MLS UTH accuracy. To concisely summarize these comparisons, we fit a line through a scatterplot of the coincidence between V4.9 MLS UTH and the other techniques. Linear regression (LR) and orthogonal distance regression (ODR) are used to establish the best fit line. The linear fits give a measure of bias (an additive correction) and a slope (a multiplicative correction). The results are summarized in Table 8.

Unfortunately, a simple concise statement cannot be made based on these comparisons. The LR fit represents how well MLS tracks the correlative technique. It measures the accuracy of the V4.9 MLS UTH if the correlative technique is accurate and both methods temporally and spatially sample the atmosphere identically. Given these limitations, the upper two MLS levels, 147 and 215 hPa, show small biases with other correlative types, less than 10 %RHi with Vaisala radiosondes and MOZAIC, and less than 5 %RHi with the frostpoint hygrometer. The scaling difference, the value one has to multiply the other technique to match the MLS measurement, ranges from 0.6 to 1.1 at 147 and 215 hPa, suggesting that MLS UTH is dry. Complicating the issue further is the uncertain quality of the archived Vaisala radiosonde data set at these heights. The raw data from the A-type humicap sensor on the older Vaisala data, believed to be the instrument used by most of the radiosonde network using Vaisala during the validation period, are known to have a significant dry bias at low temperature (e.g., a factor of 2 too dry at  $-60^{\circ}\text{C}$ ). The raw Vaisala data can be corrected. It has been shown that this bias does not appear in the archived radiosonde data and we believe it is not appropriate to apply a temperature correction to that data. The lower two MLS levels at 316 and 464 hPa are more difficult retrievals and therefore generally have lower quality. Their bias with Vaisala radiosondes and the frostpoint hygrometer is between 10–20 %RHi and with scaling differences between 0.6 and 0.9, again MLS V4.9 UTH being too dry.

The correlation coefficients of the linear fits to the coincident scatter between MLS and the other techniques at all four MLS retrieval pressures are similar. This suggests that the standard deviation of a coincident profile comparison between MLS and another technique, after correcting for the bias and scaling difference, is 25 %RHi on average

at all four heights. The 25 %RHi is very close to the globally averaged estimated MLS UTH accuracy at 147, 215, and 316 hPa levels and a factor of 2 better than that estimated at 464 hPa. Therefore the estimated uncertainty on individual profiles represents a realistic measure of the likely variability between MLS and another in situ correlative data set except at 464 hPa where the MLS estimate should be halved.

The coincident scatter, although large, is not unexpected (see section 6.1). However, comparing MLS UTH which is a relatively large volume average at a somewhat different time to essentially an in situ measurement contributes to the scatter. In this case, the bias and scaling from an LR fit will be distorted toward giving MLS a wet tendency at low %RHi and a dry tendency at high %RHi as generally observed. If the MLS UTH measurement variability is equal to the in situ UTH variability in the volume measured by MLS, the ODR fit will give better bias and scaling values. The ODR analysis gave larger negative biases at the upper two levels and smaller ones at the lower two levels. The scaling ranges from 1.0 to 2.3 with higher levels having higher values. The ODR fit would indicate that MLS has a significant wet tendency at the highest %RHi values at 147 and 215 hPa, except with MOZAIC where the ODR fit still has MLS too dry by 20 %RHi at 100 %RHi. It is noteworthy, that the ODR fit did not significantly improve the comparison between temperature-corrected Vaisala radiosondes and V4.9 MLS UTH.

CLAES extinction measurements, which are almost nearly coincident with MLS UTH measurements, provide an indirect means of quantitatively assessing V4.9 MLS UTH. CLAES extinction is extremely sensitive to cirrus. Coincident comparisons between V4.9 MLS UTH and V8 CLAES most probable extinction at 147 hPa shows a well-defined transition from clear to cirrus skies when MLS UTH is between 95 and 115 %RHi, as expected since 100 %RHi represents a humidity-saturated atmosphere. Therefore our recommendation to interpret all MLS UTH measurements greater than 120 %RHi as being in the presence of cirrus and truncating the UTH to 100 %RHi is somewhat conservative but accurate at 147 hPa. The transition between clear to cirrus at 215 hPa is broader: from 65 to 105 %RHi between the CLAES and MLS data. The coincident CLAES extinction and MLS UTH 316 hPa data do not show a distinct transition at all. The most probable extinction rising linearly with humidity and crossing the cirrus detection threshold at 95 %RHi. The CLAES comparisons appear to uphold the accuracy of the V4.9 MLS UTH with the tendency of MLS being too dry with decreasing altitude.

A third approach toward validation compared MLS mapped fields with derived quantities from meteorological analyses. These included velocity potential/divergent winds,

potential vorticity from NCEP analyses, and humidity from the GEOS 2 data assimilation model. MLS UTH is consistent with the wind fields and potential vorticity. Coincident comparisons between V4.9 MLS UTH and GEOS 2 humidity show similar biases and scaling differences as the coincident comparisons with in situ techniques. On average, the V4.9 MLS tends to be drier than GEOS 2. As with the other comparisons, the difference between MLS and GEOS 2 is smallest at 147 hPa and largest at 464 hPa. The standard deviation of the profile comparisons between MLS UTH and GEOS 2 is near 27 %RH for all four levels.

## 9. Future Work

UTH is an unanticipated product from UARS MLS for which the instrument was not designed, but it has become an important contribution from the experiment. Despite the challenges, UTH measured from MLS appears to be a scientifically useful product as many studies have shown. Future work may include an attempt to remove the yaw cycle artifact, determining new dry and wet continuum functions for the V5 data set using the V4.9 ice saturation method, a continuous water vapor profile measurement from 464 to 0.1 hPa from a combined 202/204 and 183 GHz retrieval, and a validation with humidity measurements from the DMSP sensors. Improved laboratory measurements of the dry and wet continua would be very helpful. A laboratory program is now in place to measure the dry and water vapor continuum functions over the MLS frequencies (F. DeLucia, Ohio State University, personal communication, 2000). These results will be a great aid in understanding the measured radiance signals.

A follow up experiment, EOS MLS [Waters *et al.*, 1999], to be launched mid 2003 on the NASA Earth Observing System Aura satellite is an improved MLS which is designed to measure H<sub>2</sub>O from the mesosphere down to 500 hPa. Retrievals below 316 hPa will require fitting to absolute radiances as in the UARS-MLS case. Good overlap with the 183 GHz line measurements and improved laboratory continuum measurements should greatly improve the quality of UTH to be obtained from EOS MLS.

## Appendix A: A Priori Constrained Least Squares is Optimal Estimation

Given some radiances,  $\hat{I}_{\text{meas}}^L$  (equation (2)) and an a priori UTH profile,  $\mathbf{RH}_{\text{apriori}}$ , (14) is shown to be equivalent to optimal estimation [Rodgers, 1976, equation (99)]. This is shown more generally for any two measurements by Froidevaux *et al.* [1996]. The case where an instrument measurement is combined with an a priori profile is shown here. Be-

ginning with definitions of measurements, covariances, and measurement sensitivities as defined in (15), (17), and (19), the estimated measurement error covariance, (16), is written as

$$\mathbf{S}_{\text{rh}} = \left( \begin{bmatrix} \mathbf{K}_{\text{rh}} & | & \mathbf{1} \end{bmatrix} \begin{bmatrix} \mathbf{S}_{\text{rad}}^{-1} & | & \mathbf{0} \\ \mathbf{0} & | & \mathbf{S}_{\text{apriori}}^{-1} \end{bmatrix} \begin{bmatrix} \mathbf{K}_{\text{rh}}^t \\ | \\ \mathbf{1} \end{bmatrix} \right)^{-1}. \quad (\text{A1})$$

There must be no correlations between the radiance measurements and the a priori profiles which is indicated here by the off-diagonal block  $\mathbf{0}$  in the error covariance matrix. Expanding (A1) gives

$$\mathbf{S}_{\text{rh}} = \left( \mathbf{S}_{\text{apriori}}^{-1} + \mathbf{K}_{\text{rh}} \mathbf{S}_{\text{rad}}^{-1} \mathbf{K}_{\text{rh}}^t \right)^{-1}, \quad (\text{A2})$$

which is the covariance for optimal estimation [Rodgers, 1976, equation (102)].

The profile estimate, (14), can be expanded similarly,

$$\begin{aligned} \mathbf{RH} &= \mathbf{RH}_{\text{initial}} + \begin{bmatrix} \hat{I}_{\text{meas}}^L - \hat{I}_{\text{initial}}^L & | & \mathbf{RH}_{\text{apriori}} - \mathbf{RH}_{\text{initial}} \end{bmatrix} \\ &\times \begin{bmatrix} \mathbf{S}_{\text{rad}}^{-1} & | & \mathbf{0} \\ \mathbf{0} & | & \mathbf{S}_{\text{apriori}}^{-1} \end{bmatrix} \begin{bmatrix} \mathbf{K}_{\text{rh}}^t \\ | \\ \mathbf{1} \end{bmatrix} \mathbf{S}_{\text{rh}}, \end{aligned} \quad (\text{A3})$$

where  $\hat{I}_{\text{initial}}^L$  are the calculated radiances from (2) for humidity profile  $\mathbf{RH}_{\text{initial}}$ . Equation (A3) expands to

$$\begin{aligned} \mathbf{RH} &= \mathbf{RH}_{\text{initial}} + \left[ (\hat{I}_{\text{meas}}^L - \hat{I}_{\text{initial}}^L) \mathbf{S}_{\text{rad}}^{-1} \mathbf{K}_{\text{rh}}^t \right. \\ &\quad \left. + (\mathbf{RH}_{\text{apriori}} - \mathbf{RH}_{\text{initial}}) \mathbf{S}_{\text{apriori}}^{-1} \right] \mathbf{S}_{\text{rh}}, \end{aligned} \quad (\text{A4})$$

which is equivalent to [Rodgers, 1976, equation (99)]. Equation (A4) is the transpose of the standard form because the measurement and state vectors are represented in a row format (for Interactive Data Language programming ease) instead of the usual column format. Equation (14) offers no advantage over (A4) except that allows the user to apply standard least squares software routines to optimal estimation problems which was done here.

**Acknowledgments.** We thank the entire MLS instrument and data processing teams for assistance in producing the MLS UTH product. We are grateful to R. E. Newell at Massachusetts Institute of Technology and B. J. Sandor at the National Center for Atmospheric Research for initiating several scientific investigations that provided the first validation of the preliminary data set, H. L. Clark and R. S. Harwood at Edinburgh University for identifying the yaw cycle dependence in the data, M. R. Schoeberl and the UARS project at NASA Goddard Space Flight Center for encouragement and support in producing the MLS UTH data set, and L. M. Miloshevich at the National Center for Atmospheric Research for many discussions regarding the low-temperature bias in the Vaisala RS80-A radiosondes. We also thank the two anonymous referees for their helpful comments. The research described

here done at the Jet Propulsion Laboratory, California Institute of Technology, was under contract with the National Aeronautics and Space Administration and funded through its UARS Project.

## References

- Anderson, P. S., A method for rescaling humidity sensors at temperatures well below freezing, *J. Atmos. Oceanic Technol.*, **11**, 1388–1391, 1994.
- Barath, F. T., et al., The Upper Atmosphere Research Satellite Microwave Limb Sounder Instrument, *J. Geophys. Res.*, **98**, 10,751–10,762, 1993.
- Bauer, A., and M. Godon, Temperature dependence of water-vapor absorption in linewings at 190 GHz, *J. Quant. Spectrosc. Radiat. Transfer*, **46**, 211–220, 1991.
- Bauer, A., M. Godon, J. Carlier, and Q. Ma, Water vapor absorption in the atmospheric window at 239 GHz, *J. Quant. Spectrosc. Radiat. Transfer*, **53**, 411–423, 1995.
- Bevington, P. R., *Data Reduction and Error Analysis for the Physical Sciences*, McGraw-Hill, New York, 1969.
- Borysow, A., and L. Frommhold, Collision-induced rototranslational absorption spectra of N<sub>2</sub>–N<sub>2</sub> pairs for temperatures from 50 to 300 K, *Astrophys. J.*, **311**, 1043–1057, 1986.
- Cess, R. D., et al., Intercomparison and interpretation of climate feedback processes in 19 atmospheric general circulation models, *J. Geophys. Res.*, **95**, 16,601–16,615, 1990.
- Chandra, S., J. R. Ziemke, W. Min, and W. G. Read, Effects of 1997–1998 El Niño on tropospheric ozone and water vapor, *Geophys. Res. Lett.*, **25**, 3867–3870, 1998.
- Chen, M., R. B. Rood, and W. G. Read, Upper tropospheric water vapor from GEOS reanalysis and UARS MLS observation, *J. Geophys. Res.*, **103**, 19,587–19,594, 1998.
- Chen, M., R. B. Rood, and W. G. Read, Seasonal variations of upper tropospheric water vapor and high clouds observed from satellites, *J. Geophys. Res.*, **104**, 6193–6197, 1999.
- Chiou, E. W., M. P. McCormick, and W. P. Chu, Global water vapor distributions in the stratosphere and upper troposphere derived from 5.5 years of SAGE-II observations, *J. Geophys. Res.*, **102**, 19,105–19,118, 1997.
- Clark, H. J., R. S. Harwood, P. W. Mote, and W. G. Read, Variability of water vapor in the tropical upper troposphere as measured by the Microwave Limb Sounder on UARS, *J. Geophys. Res.*, **103**, 31,695–31,707, 1998.
- Dagg, I. R., G. E. Reesor, and J. L. Urbaniak, Collision induced microwave absorption in N<sub>2</sub>, CH<sub>4</sub>, and N<sub>2</sub>–Ar, N<sub>2</sub>–CH<sub>4</sub> mixtures at 1.1 and 2.3 cm<sup>−1</sup>, *Can. J. Phys.*, **52**, 821–829, 1974.
- Dagg, I. R., G. E. Reesor, and J. L. Urbaniak, Collision induced absorption in N<sub>2</sub>, CO<sub>2</sub>, and H<sub>2</sub> at 2.3 cm<sup>−1</sup>, *Can. J. Phys.*, **53**, 1764–1776, 1975.
- Dagg, I. R., G. E. Reesor, and J. L. Urbaniak, A microwave cavity measurement of collision-induced absorption in N<sub>2</sub> and CO<sub>2</sub> at 4.6 cm<sup>−1</sup>, *Can. J. Phys.*, **56**, 1037–1045, 1978.
- Dagg, I. R., A. Anderson, S. Yan, W. Smith, and L. A. A. Read, Collision-induced absorption in nitrogen at low temperatures, *Can. J. Phys.*, **63**, 625–631, 1985.
- Elliot, W. P., and D. J. Gaffen, On the utility of radiosonde humidity archives for climate studies, *Bull. Am. Meteorol. Soc.*, **72**, 1507–1520, 1991.
- Elliot, W. P., and D. J. Gaffen, Effects of conversion algorithms on reported upper-air dewpoint depressions, *Bull. Am. Meteorol. Soc.*, **74**, 1323–1325, 1993.
- Elson, L. S., W. G. Read, J. W. Waters, P. W. Mote, J. S. Kinnersley, and R. S. Harwood, Space-time variations in water vapor as observed by the UARS Microwave Limb Sounder, *J. Geophys. Res.*, **101**, 9001–9015, 1996.
- Froidevaux, L., et al., Validation of UARS Microwave Limb Sounder ozone measurements, *J. Geophys. Res.*, **101**, 10,017–10,060, 1996.
- Gaffen, D. J., Historical changes in radiosonde instruments and practices, *Instrum. Obs. Methods Rep. 50 WMO/TD-No. 541*, World Meteorol. Org., Geneva, 1993.
- Godon, M., J. Carlier, and A. Bauer, Laboratory studies of water vapor absorption in the atmospheric window at 213 GHz, *J. Quant. Spectrosc. Radiat. Transfer*, **47**, 275–285, 1992.
- Haas, M. R., and L. Pfister, A high-altitude site survey for SOFIA, *Publ. Astron. Soc. Pac.*, **110**, 339–364, 1998.
- Holton, J. R., P. H. Haynes, M. E. McIntyre, A. R. Douglass, R. B. Rood, and L. Pfister, Stratosphere-troposphere exchange, *Rev. Geophys.*, **33**, 403–439, 1995.
- Hu, H., and W. T. Liu, The impact of upper tropospheric humidity from Microwave Limb Sounder on the midlatitude greenhouse effect, *Geophys. Res. Lett.*, **25**, 3151–3154, 1998.
- Intergovernmental Panel on Climate Change, *Climate Change 1995: The Science of Climate Change*, Cambridge Univ. Press, New York, 1995.
- Jarnot, R. F., R. E. Cofield, J. W. Waters, D. A. Flower, and G. E. Peckham, Calibration of the Microwave Limb Sounder on the Upper Atmosphere Research Satellite, *J. Geophys. Res.*, **101**, 9957–9982, 1996.
- Jensen, E. J., W. G. Read, J. Mergenthaler, B. J. Sandor, L. Pfister, and A. Tabazadeh, High humidities and subvisible cirrus near the tropical tropopause, *Geophys. Res. Lett.*, **26**, 2347–2350, 1999.
- Kley, D., J. M. Russell III, and C. Phillips, SPARC assessment of upper tropospheric and stratospheric water vapour, *SPARC Report No. 2, WCRP-113*, WMO/ICSU/IOC, CNRS, Verrières le Buisson, 2000.
- Knollenberg, R. G., K. Kelly, and J. C. Wilson, Measurements of high number densities of ice crystals in the tops of tropical cumulonimbus, *J. Geophys. Res.*, **98**, 8639–8664, 1993.
- Larsen, J. C., E. W. Chiou, W. P. Chu, M. P. McCormick, L. R. McMaster, S. Oltmans, and D. Rind, A comparison of the Stratospheric Aerosol and Gas Experiment II tropospheric water vapor to radiosonde measurements, *J. Geophys. Res.*, **98**, 4897–4917, 1993.
- Liebe, H. J., MPM: An atmospheric millimeter-wave propagation model, *Int. J. Infrared Millimeter Waves*, **10**, 631–650, 1989.
- Liebe, H. J., T. Manabe, and G. A. Hufford, Millimeter-wave attenuation and delay rates due to fog/cloud conditions, *IEEE Trans. Antennas Propag.*, **37**, 1617–1623, 1989.
- Liebe, H. J., G. A. Hufford, and M. G. Cotton, Propagation modeling of moist air and suspended water/ice particles at frequencies below 1000 GHz, paper presented at 52nd Specialists' Meeting of the Electromagnetic Wave Propagation Panel, Adv. Group for Aerosp. Res. and Dev., Palma De Mallorca, Spain, 1993.

- Lindzen, R. S., Some coolness concerning global warming, *Bull. Am. Meteorol. Soc.*, **71**, 288–299, 1990.
- List, R. J., Smithsonian meteorological tables, *Smithson. Misc. Collect. 114*, Smithson. Inst., Washington, D. C., 1951.
- Manabe, S., and R. T. Wetherald, Thermal equilibrium of the atmosphere with a given distribution of relative humidity, *J. Atmos. Sci.*, **24**, 241–259, 1967.
- Marengo, A., et al., Measurement of ozone and water vapor by airbus in-service aircraft: The MOZAIC airborne program, an overview, *J. Geophys. Res.*, **103**, 25,631–25,642, 1998.
- Mergenthaler, J. L., A. E. Roche, J. B. Kumer, and G. A. Ely, CLAES observation of tropical cirrus, *J. Geophys. Res.*, **104**, 22,183–22,194, 1999.
- Miloshevich, L. M., H. Vömel, A. Paukkunen, A. J. Heymsfield, and S. J. Oltmans, Characterization and correction of relative humidity measurements from Vaisala RS80-A radiosondes at cold temperatures, *J. Atmos. Oceanic Technol.*, **18**, 135–156, 2001.
- Newell, R. E., Y. Zhu, E. V. Browell, S. Ismail, W. G. Read, J. W. Waters, K. K. Kelly, and S. C. Liu, Upper tropospheric water vapor and cirrus: Comparisons of DC-8 observations, preliminary UARS Microwave Limb Sounder measurements and meteorological analyses, *J. Geophys. Res.*, **101**, 1931–1941, 1996a.
- Newell, R. E., Y. Zhu, E. V. Browell, W. G. Read, and J. W. Waters, Walker circulation and tropical upper tropospheric water vapor, *J. Geophys. Res.*, **101**, 1961–1974, 1996b.
- Newell, R. E., Y. Zhu, W. G. Read, and J. W. Waters, Relationship between tropical upper tropospheric moisture and eastern tropical Pacific sea surface temperature at seasonal and interannual time scales, *Geophys. Res. Lett.*, **24**, 25–28, 1997.
- Oltmans, S., Measurements of water vapor in the stratosphere with a frost point hygrometer, *Proceedings of the 1985 International Symposium on Moisture and Humidity*, pp. 251–258, Measurement and Control in Science and Industry, Instrum. Soc. of Am., Washington, D.C., 1985.
- Pardo, J. R., E. Serabyn, and J. Cernicharo, Submillimeter atmospheric transmission measurements on Mauna Kea during extremely dry El Niño conditions: Implications for broadband opacity contributions, *J. Quant. Spectrosc. Radiat. Transfer*, **68**, 419–433, 2001.
- Paukkunen, A., Sensor heating to enhance reliability of radiosonde humidity measurement, paper presented at *11th AMS International Conference on Interactive Information and Processing Systems for Meteorology, Oceanography and Hygrology*, pp. 103–106, Am. Meteorol. Soc., Dallas, Tex., 1995.
- Peixoto, J. P., and A. H. Oort, The climatology of relative humidity in the atmosphere, *J. Clim.*, **9**, 3443–3463, 1996.
- Pueschel, R. F., et al., Condensed water in tropical cyclone Oliver, 8 February 1993, *Atmos. Res.*, **38**, 297–313, 1995.
- Pumphrey, H. C., Validation of a new prototype water vapor retrieval for the UARS Microwave Limb Sounder, *J. Geophys. Res.*, **104**, 9399–9412, 1999.
- Read, W. G., EOS MLS forward model algorithm theoretical basis document, *Tech. Rep. JPL D-18130*, Jet Propul. Lab., Pasadena, Calif., 1999.
- Read, W. G., J. W. Waters, D. A. Flower, L. Froidevaux, R. F. Jarnot, D. L. Hartmann, R. S. Harwood, and R. B. Rood, Upper tropospheric water vapor from UARS MLS, *Bull. Am. Meteorol. Soc.*, **76**, 2381–2389, 1995.
- Rind, D., E.-W. Chiou, W. Chu, S. Oltmans, J. Lerner, J. Larsen, M. P. McCormick, and L. McMaster, Overview of the Stratospheric Aerosol and Gas Experiment II water vapor observations: Method, validation, and data characteristics, *J. Geophys. Res.*, **98**, 4835–4856, 1993.
- Roche, A. E., J. B. Kumer, J. L. Mergenthaler, G. A. Ely, W. G. Uplinger, J. F. Potter, T. C. James, and L. W. Sterritt, The cryogenic limb array etalon spectrometer (CLAES) on UARS: Experiment description and performance, *J. Geophys. Res.*, **98**, 10,763–10,775, 1993.
- Rodgers, C. D., Retrieval of atmospheric temperature and composition from remote measurements of thermal radiation, *Rev. Geophys.*, **14**, 609–624, 1976.
- Rodgers, C. D., Characterization and error analysis of profiles retrieved from remote sounding measurements, *J. Geophys. Res.*, **95**, 5587–5595, 1990.
- Rood, R. B., A. R. Douglass, M. C. Cerniglia, and W. G. Read, Synoptic-scale mass exchange from the troposphere to the stratosphere, *J. Geophys. Res.*, **102**, 23,467–23,485, 1997.
- Sandor, B. J., W. G. Read, J. W. Waters, and K. H. Rosenlof, Seasonal behavior of tropical to mid-latitude upper tropospheric water vapor from UARS-MLS, *J. Geophys. Res.*, **103**, 25,935–25,947, 1998.
- Sandor, B. J., E. J. Jensen, E. M. Stone, W. G. Read, J. W. Waters, and J. L. Mergenthaler, Upper tropospheric humidity and thin cirrus, *Geophys. Res. Lett.*, **27**, 2645–2648, 2000.
- Sassi, F., M. Salby, and W. G. Read, Relationship between upper-tropospheric humidity and deep convection, *J. Geophys. Res.*, **106**, 17,133–17,146, 2001.
- Schmidlin, F. J., WMO international radiosonde intercomparison phase II, *Instrum. Obs. Methods Rep. 29, WMO/TD-312*, World Meteorol. Org., Geneva, 1988.
- Schubert, S. D., R. B. Rood, and J. Pfaendtner, An assimilated dataset for earth science applications, *Bull. Am. Meteorol. Soc.*, **74**, 2331–2342, 1993.
- Soden, B. J., and F. P. Bretherton, Interpretation of TOVS water vapor radiances in terms of layer-average relative humidities: Method and climatology for the upper, middle, and lower troposphere, *J. Geophys. Res.*, **101**, 9333–9343, 1996.
- Soden, B. J., and J. R. Lanzante, An assessment of satellite and radiosonde climatologies of upper-tropospheric water vapor, *J. Clim.*, **9**, 1235–1250, 1996.
- Spencer, R. W., and W. D. Braswell, How dry is the tropical free troposphere? Implications for global warming theory, *Bull. Am. Meteorol. Soc.*, **78**, 1097–1106, 1997.
- Stone, E. M., W. J. Randel, J. L. Stanford, W. G. Read, and J. W. Waters, Baroclinic wave variations observed in MLS upper tropospheric water vapor, *Geophys. Res. Lett.*, **23**, 2967–2970, 1996.
- Stone, E. M., L. Pan, B. J. Sandor, W. G. Read, and J. W. Waters, Spatial distributions of upper tropospheric water vapor measurements from the UARS Microwave Limb Sounder, *J. Geophys. Res.*, **105**, 12,149–12,161, 2000.
- Stone, N. W. B., L. A. A. Read, A. Anderson, I. R. Dagg, and W. Smith, Temperature dependent collision induced absorption in nitrogen, *Can. J. Phys.*, **62**, 338–347, 1984.

- Urbaniak, J. L., I. R. Dagg, and G. E. Reesor, Collision induced microwave absorption in N<sub>2</sub>, CH<sub>4</sub>, and CF<sub>4</sub> in the gaseous and liquid phases, *Can. J. Phys.*, 55, 496–505, 1977.
- Wang, P.-H., P. Minnis, M. P. McCormick, G. S. Kent, and K. M. Skeens, A 6-year climatology of cloud occurrence frequency from Stratospheric Aerosol and Gas Experiment II observations (1985–1990), *J. Geophys. Res.*, 101, 29,407–29,429, 1996.
- Waters, J. W., et al., The UARS and EOS Microwave Limb Sounder (MLS) experiments, *J. Atmos. Sci.*, 56, 194–218, 1999.
- Wu, D. L., Remote sensing of clouds and water vapor by microwave limb sounding, paper presented at *International Asia-Pacific Symposium 1998 in Beijing, China*, Soc. of Photo-optical Instrum. Eng., Bellingham, Wash., 1998.
- Wu, X., J. J. Bates, and S. J. S. Khalsa, A climatology of the water vapor band brightness temperatures from NOAA operational satellites, *J. Clim.*, 6, 1282–1300, 1993.
- W. G. Read, J. W. Waters, D. L. Wu, Z. Shippony, and A. C. Smedley, Jet Propulsion Laboratory, Mail Stop 183-701, 4800 Oak Grove Drive, Pasadena, CA., 91109, USA. (bill@mls.jpl.nasa.gov; joe@mls.jpl.nasa.gov; dwu@mls.jpl.nasa.gov; zvi@mls.jpl.nasa.gov; andrea@mls.jpl.nasa.gov)
- E. M. Stone, ASM Lithography Holding N. V., 77 Danbury Road, Wilton, CT. 06897, USA. (emstone@snet.net)
- C. C. Smallcomb, National Weather Service, 6201 Theiler Lane, Louisville, KY., 40229, USA. (smallcomb1@home.com)
- S. Oltmans, NOAA Climate Monitoring and Diagnostics Laboratory, CMDL R/E/CGI, 325 Broadway, Boulder, CO. 80303, USA. (soltmans@cmdl.noaa.gov)
- D. Kley, and H. G. J. Smit, Institute for Chemistry of the Polluted Atmosphere, Department for Chemistry and Dynamics of the Geosphere, Research Centre Juelich GmbH, Postfach 1913, D–52425, Juelich, Germany. (D.Kley@fz-juelich.de; h.smit@fz-juelich.de)
- J. L. Mergenthaler, Lockheed Martin Advanced Technology Center, Dept. 91-20, Bldg. 252, 3251 Hanover Street, Palo Alto, CA. 94304, USA. (MERGEN@clae.spasci.com)
- M. K. Karki, NASA Goddard Space Flight Center, Data Assimilation Office, Code 910.2, Greenbelt, MD. 20771, USA. (karki@dao.gsfc.nasa.gov)
- November 6, 2000; revised April 24, 2001; accepted June 19, 2001.

---

This preprint was prepared with AGU's L<sup>A</sup>T<sub>E</sub>X macros v4, with the extension package 'AGU++' by P. W. Daly, version 1.5g from 1998/09/14.